DEVELOPMENT OF MILLIMETER WAVE SYSTEM COMPONENTS FOR 5G/6G WIRELESS NETWORKS

MEHMET FARUK CENGİZ

Thesis for the Master's Program in Electrical and Electronics Engineering

Graduate School

Izmir University of Economics

Izmir

2022

DEVELOPMENT OF MILLIMETER WAVE SYSTEM COMPONENTS FOR 5G/6G WIRELESS NETWORKS

MEHMET FARUK CENGİZ

THESIS ADVISOR: PROF. DR. DIAA GADELMAVLA

A Master's Thesis
Submitted to
The Graduate School of Izmir University of Economics
The Department of Electrical and Electronics Engineering

Izmir
2022

ETHICAL DECLARATION

I hereby declare that I am the sole author of this thesis and that I have conducted my work in accordance with academic rules and ethical behaviour at every stage from the planning of the thesis to its defence. I confirm that I have cited all ideas, information and findings that are not specific to my study, as required by the code of ethical behaviour, and that all statements not cited are my own.

Mehmet Faruk Cengiz

20.12.2022

ABSTRACT

DEVELOPMENT OF MILLIMETER WAVE SYSTEM COMPONENTS FOR 5G/6G WIRELESS NETWORKS

Cengiz, Mehmet Faruk

Master's Program in Electrical and Electronics Engineering

Advisor: Prof. Dr. Diaa Gadelmavla

December, 2022

This thesis is devoted to the design of three system components for 5G and mm-wave applications based on gap waveguide technology. A Triple-band bandpass filter is designed for Ka-band applications with resonance frequencies of 32.32 GHz, 35.75 GHz, and 38.12 GHz, and low insertion losses of about 0.6 dB, 1.1 dB, and 0.9 dB, respectively. A four-port MIMO antenna for applications in V/W frequency bands is developed. It is suitable for use in automotive radar and inter-satellite applications in the range of 72.7 to 79.5 GHz. A new 4 x 1 rectangular slot antenna array for D-band applications is developed in the range from 140.9 to 157.7 GHz. The overall efficiency is around 95%, and the maximum gain is about 10 dBi. A DGS-based isolation enhancement-based four-port MIMO antenna is designed for D-band applications. The impedance bandwidth extends from 148 GHz to 161.7 GHz. Employing different DGS geometries is effective in coupling reductions, the highest coupling level obtained from different DGS geometries is -26.4 dB the lowest level reaches about -96 dB, with a maximum realized gain of 7.97 dBi. Optimum diversity properties are obtained. A novel reconfigurable metasurface-based compact UWB hybrid coupler is developed for Ku-band applications in the range from 11.94 to 16.91 GHz, covering the Ku-band. The coupler delivers continuously adjustable amplitudes between 2.6 and 4.8 dB while the phase differences are within 77° to 105° over a fractional bandwidth (FBW) of 34.45%. Our proposed design is the first adjustable phase coupler in the Ku band/mm-band ranges.

Keywords: RGW, SIGW, MIMO Antenna, Array Antenna, Multi-band filter, Reconfigurable coupler.

ÖZET

5G/6G KABLOSUZ AĞLAR İÇİN MİLİMETRİK DALGA SİSTEM BİLEŞENLERİNİN GELİŞTİRİLMESİ

Cengiz, Mehmet Faruk

Elektrik - Elektronik Mühendisliği Yüksek Lisans Programı

Tez Danışmanı: Prof. Dr. Diaa Gadelmavla

Aralık, 2022

Bu tez, boşluk dalga kılavuzu teknolojisine dayalı 5G ve mm dalga uygulamaları için üç sistem bileşeninin tasarımına ayrılmıştır. Üç bantlı bant geçiren filtre, sırasıyla 32,32 GHz, 35,75 GHz ve 38,12 GHz rezonans frekanslarına ve yaklaşık 0,6 dB, 1,1 dB ve 0,9 dB düşük ekleme kayıplarına sahip Ka-bant uygulamaları için tasarlanmıştır. V/W frekans bantlarındaki uygulamalar için dört portlu MIMO anten geliştirilmiştir. 72,7 ile 79,5 GHz aralığı arasındaki otomotiv radar ve uydular arası uygulamalarda kullanıma uygundur. D-bant uygulamaları için 140,9 ile 157,7 GHz aralığında yeni 4 x 1 dikdörtgen yarık anten dizisi geliştirilmiştir. Genel verimlilik %95 civarındadır ve maksimum kazanç yaklaşık 10 dBi'dir. DGS izolasyon geliştirme tabanlı dört portlu MIMO anteni, D-bandı uygulamaları için tasarlanmıştır. Empedans bant genişliği 148 GHz'den 161,7 GHz'e kadar uzanır. Farklı DGS geometrilerinin kullanılması kuplaj azaltmalarında etkili olup bu geometrilerinden elde edilen en yüksek kuplaj seviyesi -26,4 dB'dir, en düşük seviye yaklaşık -96 dB'ye ulaşır ve maksimum gerçekleşen kazanç 7,97 dBi'dir. 11,94 ile 16,91 GHz aralığındaki Ku-bant uygulamaları için özgün, ayarlanabilir metayüzey tabanlı kompakt UWB hibrit kuplör geliştirildi. Kuplör, 2,6 ile 4,8 dB arasında sürekli olarak ayarlanabilen büyüklük sunarken, faz farkları 77° ila 105° aralığındadır ve %34,45'lik kesirli bant genişliğine (FBW) sahiptir. Önerdiğimiz tasarım, Ku bandı/mm-bant aralığındaki ilk ayarlanabilir faz kuplörüdür.

Anahtar Kelimeler: RGW, SIGW, MIMO Anten, Anten Disizi, Çok Bantlı Filtre, Ayarlanabilir Kuplör.

ACKNOWLEDGEMENTS

Above all, I would like to express my sincere gratitude to my academic adviser, Prof. Dr. Diaa Gadelmavla for his invaluable guidance, advice, and encouragement. I feel extremely lucky to have him as my thesis adviser.

I am thankful to Prof. Dr. Abdelmegid Allam for his outstanding lectures and for sharing his knowledge and comments which developed me to understand the fundamentals very well. I hope we will be able to work together in the future.

I am very grateful to Masoud Abedinifar, Sude Pehlivan, Barış Dal and Özge Büyükdeveci who have given me their friendship and their never-ending support.

At last, I would like to thank my parents for their love, support and encouragement.

To my family...

TABLE OF CONTENTS

LIST OF TABLES

LIST OF FIGURES

CHAPTER 1 : INTRODUCTION

In the last decades, communication technology has advanced very quickly. Indeed, communication technologies have significant impacts on contemporary culture. The nowadays fast development of wireless and mobile communications has made it easier for people to coordinate and exchange information. Wi-Fi access points and base station networks are nearly everywhere, enabling users of mobile terminals to connect at any time. There are several potential commercial uses for wireless technology, including point-to-multipoint services, high-speed chip-to-chip connectivity, satellite communications, vehicle radars, imaging, and security systems. However, the biggest obstacle is the saturation of the existing spectrum at microwave frequencies below 10 GHz (Liu, 2019). As a result, it is essential to investigate new frequency bands at higher frequencies. At the moment, millimeter and sub-millimeter wave communications have received a lot of interest. But according to the fundamentals of electromagnetic field theory, wireless communications in such frequency ranges are easily impacted by propagation losses and by significant air absorption. To overcome these impairments facing wireless systems, waveguide structures with low-loss characteristics and high-gain system components such as antennas, filters, couplers, etc. are required.

Microstrip transmission lines are often utilized at lower frequencies where waves propagate in the transverse electromagnetic (TEM) mode, this mode has neither an electric nor magnetic field in its direction of propagation. In communication systems, the TEM mode is chosen because it has no dispersion. The TEM mode also has a zero hertz cutoff frequency, allowing it to transmit any signal at any frequency. However, high dielectric losses occur at the mm-wave ranges due to the fact that microstrip lines are susceptible to surface waves and high cavity modes at higher frequencies produce undesirable radiation. These problems encourage the utilization of waveguide structures because of their excellent power handling capacities and minimal insertion losses. Particularly, at the mm-wave frequencies. Conventional waveguide structures have significant losses while not supporting the TEM mode. The waveguides' reliance on TE as the dominant mode is one of their main drawbacks. In addition, they suffer from several shortcomings, including excessive signal dispersion, complexity in production, and lack of network integration (Shamseldin, 2016).

Substrate integrated waveguide (SIW) technology has demonstrated significant improvements over both conventional rectangular waveguides and printed circuit-based transmission lines in mm-Waves. SIW is a planar structure in which the field moves in the substrate in between two rows of via holes that act as the waveguide's sidewalls. Due to its low profile and ease of integration with other system components on a single board, this topology offers several benefits. On the other hand, SIW suffers from dispersive propagation and dielectric losses. Therefore, gap waveguide (GW) technology emerged as a potential replacement that could be employed in such bands without any of the aforementioned restrictions.

The gap waveguide (GW) technology has been recently employed in the development of several mm-wave-based components. Both soft and hard surfaces are considered. An important benefit in the manufacturing process of the gap waveguide-based components is that, unlike traditional waveguides, it is possible to integrate active components relatively easily since they do not require metallic connections between the top and lower plates to avoid significant leakages. This technique facilitates the mechanical assembly's issue with excellent electrical contacts, particularly at high frequencies. Ridge Gap Waveguide (RGW), Groove Gap Waveguide (GGW), Inverted Microstrip Gap Waveguide (IM-GWG), and Printed Ridge Gap Waveguide (PRGW) are the four basic GW technologies. All of these technologies enable the quasi-TEM mode, except the GGW, which supports the Transverse Electric or Transverse Magnetic (TE/TM) modes. This is the main disadvantage of GGW over the other GWs. The RGW technology, first introduced by Kildal [4], provides substantial benefits in mm-wave over traditional printed microstrip lines and waveguide structures, including some other modern technologies like SIW. The RGW technology overcomes most of these drawbacks as it considers the air gap as a dielectric layer in the design. In addition, the RGW technology minimizes the size of components, showing high performance, and lowering the manufacturing tolerance and dispersion. One of the main disadvantages of the RGW with an air-filled structure is that, it requires very accurate CNC machining and that its performance is unstable. There is a possibility that this gap may collapse in the existence of stresses or impacts. One advantage of the substrate-integrated gap waveguides (SIGW) over RGW is that the air gap is filled with the substrate layer, maintaining the air gap's height constant. Another advantage is that the fabrication process is simple (PCB-based). Inside the air gap, a quasi-TEM condition is maintained over the ridge and an electromagnetic (EM) leakage can be

stopped.

The GW-based system has drawn a lot of attention during the last decade with excessive numbers of filters, antennas, and coupler designs in the literature. Dual-mode RGW filter using three different shape perturbations was analyzed (Hassani et al., 2018). The GGW technique was applied to microwave narrow band filters for the Ku band (Mazinani et al., 2018). These systems were created without the use of dielectric materials; nevertheless, the addition of dielectric materials allows the system to have more design freedom. The PRGW based Band Pass Filter (BPF) reported by (Sorkherizi and Kishk, 2016, 2017) suffered from high losses. To the best of the authors' knowledge, no multi-band filters employing IM-GWG technology have been suggested in the Ka-band even though there are several Ka-band GW-based bandpass filter designs published in the literature (Shu et al., 2020; Li et al., 2018; Castro et al., 2021).

The remarkable technical developments in 5G and 6G wireless communications have created a huge need for high-performance system components, especially antennas. Higher operating frequencies primarily result in smaller system components and more compact structures. Wideband communication over short distances is also made possible by the use of higher-frequency bands. As a result, millimeter-wave (mm-wave) frequencies are often employed in several industries, including military applications, satellite systems, and automobile radar systems (Okan, 2021; Khan et al., 2022). There are two frequency bands assigned for automotive radar applications, they operate around 24 GHz and 77 GHz; where the 77 GHz band permits a smaller size with improved resolution, better range, and angular resolution compared to the 24 GHz range. As the antenna is one of the most important components of any radar system, so it is critical to developing a high-performance antenna for the 77 GHz vehicle radar systems (Teng et al., 2022) which is one of the targets of the current work .

Multiple Input Multiple Output (MIMO) systems, which consider multiple antenna units on both the transmitter and the receiver sides, can significantly increase the performance of wireless communication systems. The multipath propagation is realized by the use of several transmitting and receiving antennas which in turn increases the data rates and radio link capacities. The MIMO technology usually

requires huge bandwidths, which are only available at high millimeter-wave and sub-terahertz domains, this, in turn, enhances the capacity to hundreds of gigabits per second (Frecassetti et al., 2019; Vassilev et al., 2018). Another advantage of the MIMO technology is the ability to improve the system's capabilities, channel capacity, and coverage area, preventing multipath attenuation and channel interference (Aghoutane et al., 2022; Fakharian et al., 2022).

One of the main problems in MIMO systems is the isolation between the antenna elements. This problem has a cascading effect on other metrics used to determine the MIMO antenna system diversity parameters. The most important metrics that influence the antenna performance in a MIMO system are the Envelope Correlation Coefficient (ECC), Diversity Gain (DG), Channel Capacity Loss (CCL), Multiplexing Efficiency (ME), and Total Active Reflection Coefficient (TARC). A straightforward way to obtain high isolation is to increase the physical distance between the radiators, although this leads to a huge antenna size. Researchers have tried to come up with different techniques to expand packing density while also improving the radiator's isolation. Several methods to improve antenna isolation are suggested in the literature. Increasing the physical distance between the antenna elements is an easy technique to get good isolation (Huang et al., 2021), but with the cost of increased antenna size. Commonly used coupling minimization techniques include the Defected Ground Structure (DGS), Split Ring Resonator (SRR), and Electromagnetic Bandgap Structures (EBG). These are useful strategies for altering the surface current route to enhance isolation (Tan et al., 2019; Tebache et al., 2018; Wu et al., 2018; Ghalib and Sharawi, 2017). Another method involves etching an isolating slit between the antenna components (Chen et al., 2017; Li et al., 2019; Iqbal et al., 2017). Even though these isolating gaps reduce the reciprocal coupling between the radiating antennas, however, they do not affect the system gain. A parasitic structure has also been proposed as a decoupling design to provide good isolation by providing an additional coupling line. However, they necessitate additional decoupling structures, which take up more space and complicate the construction of the MIMO antenna (Sun et al., 2020; Li et al., 2011; Mathur and Dwari, 2018).Our second target is to develop a MIMO system with enhancement in the isolation using the DGS technique.

Couplers with numerous functionalities have received a great deal of attention for the development of multi-standard communication systems. The functions of signal

isolation, mixing, and separation, as well as signal amplitude and phase acquisition, are all vital for the 5G communication system applications, making directional couplers a critical component. Many coupler designs have been studied using GW technology in recent years (Farahani et al., 2017; Nematpour et al., 2019; Shen et al., 2018; Mahmoud Ali et al., 2019; Birgermajer et al., 2017; Ghaly et al., 2022; Ali et al., 2021, 2017; Nasr and Kishk, 2020; Mousavirazi et al., 2022; Zarifi and Shater, 2017; Zhao and Denidni, 2020; Taraji, 2022; Zarifi et al., 2022). However, none of them is reconfigurable.

The demand for reconfigurable devices is increasing because of offering great flexibility and simple expansion for new usage conditions. Moreover, the ability to reconfigure a wireless communication system becomes a necessity to save costs and provide the best performance for various applications. Couplers are commonly used to build a beamforming network to be capable of producing the required radiation beams. The hybrid coupler, acting as a phase shifter, is also capable of performing a power division function and the phase shift. The typical coupler-based beamforming network can only produce limited beams because of the standard phase differences such as 90° and 0°/180°. It is typically required to have a constantly controlled phase difference for greater flexibility. The easiest approach is to add a phase shifter after the power divider or hybrid coupler. However, three major issues arise later: high insertion loss, significant phase change, and enormous circuit size (Xu, Zheng and Long, 2019). The radiation beams can be constantly scanned over a large area if the coupler can give a reconfigurable phase difference. That is why it is essential to have a coupler with a broad phase adjustment range. All types of reconfigurable couplers garnered a lot of interest in microwave integrated circuits with variable power-dividing ratios (Peng et al., 2021; Chu and Ma, 2019; Shah et al., 2013; Marcaccioli et al., 2008), and operating-frequency adjustment (Wan et al., 2020; Tan and Lin, 2019; Dwivedy and Behera, 2019; Tan et al., 2020). Only a few numbers of structures have been documented in the literature since the reconfigurability in phase difference is more difficult than that in frequency or power division ratio (Xu, Wang and Liu, 2019; Zheng, 2017; Zhu and Abbosh, 2017; Pan et al., 2019). Varactor-tuned couplers were researched to complete the continuously adjustable differential phase at a given frequency in order to increase the phase coverage. Generally tuning ranges between 45° and 135° can be provided with the current phase-reconfigurable coupler. The periodic employment of Varactors as transmission line loads allows control voltage

modification of the equivalent circuit capacitance which supplied a 30°-150° phase difference (Xu, Wang and Liu, 2019). In Zheng (2017) a Varactor-loaded branch line coupler ensures equal power division with a configurable phase difference of 45° to 135°. By substituting an adjustable phase shifting unit for the horizontal branch, the phase difference is continuously set from 45 to 135 (Zhu and Abbosh, 2017). In Pan et al. (2019) a tunable unit was made up of open and shorted stubs, tunable capacitors, and two eighth wavelength linked lines which achieved a 0° to 180° phase difference. All these phase tunable capacitor designs are lumped elements based and in addition to that, the operating frequencies are below 3 GHz.

The main objectives of this study are divided into six sections:

- To develop fundamental mm-wave system components: Bandpass filter, MIMO, and antenna array systems, and non-reconfigurable and reconfigurable coupler designs using GW-based technology as the feeding network.

- Development of a multi-band bandpass filter for Ka applications using IM-GWG by enhancing the obtained fractional bandwidths.

- To develop high-gain antennas with a UWB to facilitate high data transmission for millimeter-wave applications.

- To improve the compact-sized structures and to enhance the isolation levels in a MIMO system using DGS and orthogonal polarization techniques targeting applications in V, W, and D bands.

- To design a novel mechanically tunable compact SIGW-based hybrid coupler.

CHAPTER 2 : DESIGN OF TRIPLE-BAND BPF USING IMGWG FOR KA-BAND APPLICATIONS

This study presents a multi-band Band Pass Filter (BPF) using an IMGWG feeding network. A double octagonal ring resonator (RR) with corner cuts was used for the design. The current project has two goals: firstly, to create multi-band filters for Ka applications; and secondly to improve the acquired fractional bandwidths (FBW). The development process of the proposed work is summarized as follows:

- IMGWG feeding network and octagonal ring resonator design and optimization

- Triple-band BPF simulation and performance analysis

- Conclusion of IMGWG-based triple-band BPF

2.1 *IMGWG Feeding Network And Filter Design*

The unit cell and the supercell of the IMGWG structure are shown in Fig.1. The dimensions are optimized for the Ka-band frequency range. The dielectric material is chosen to be Rogers RT5880 (ε_r = 2.2 and $tan\delta$ = 0.0009) due to its low losses at high frequencies. The substrate has a thickness of 0.787 mm. The dispersion diagram was calculated with the CST Eigen Mode. The proposed unit cell's bandgap spans the frequencies from 27 GHz to 40.5 GHz while the supercell's 30.3 to 39.8 GHz. The dispersion diagram of the unit cell and supercell are depicted in Fig. 2.

The proposed multiple-band bandpass filter is based on two octagonal ring resonators (RR) with corner cuts that connect the orthogonal patches on top of the feed line, this technique is found to be good to generate multiple resonances (Puentes et al., 2011). To achieve a sharp cut-off frequency response, octagonal resonators are preferred rather than circular ring resonators (Manzoor and Pak, 2018). The corner cuts on the patches generate an inductive effect that alters the response of the resonator coupling (Gorur, 2004). The developed filter consists of two orthogonal patches with a length of about 2.2 mm (approximately $\lambda/4$) and a width of 0.3 mm. The diagonal line of the outer octagonal patch is 4.4 mm, and the width is 0.4 mm. The gap between the resonators is 0.4 mm. The width of the feed line is optimized at 3.6 mm for 50 Ω. Fig. 3 shows the proposed filter, and Table 1 lists the dimensions.

(a)

(b)
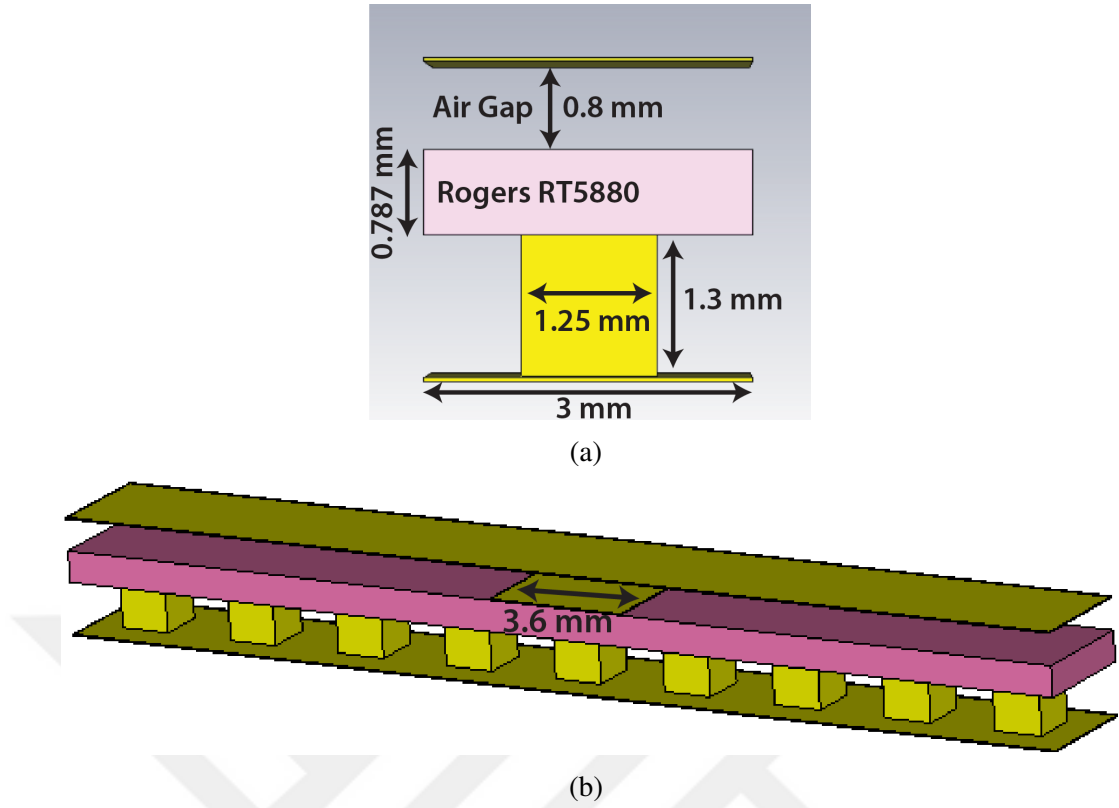
Figure 1. IMGWG (a) unit cell design (b) supercell design

Table 1. Dimensions of the unit cell and supercell

Parameters	L1	L2	L3	L4	L5	W1	W2	W3	z	d
Values (mm)	2.2	1.47	1.07	5.7	5.3	3.6	0.8	0.3	0.4	0.4

The port dimension for IMGWG technology is selected based on the formula conducted in Equation (1) where p: periodicity, W1: feed line width, and a: width of the port's horizontal plane.

$$\frac{3*p-W1}{2} \leq a \leq \frac{3*p+W1}{2} \qquad (1)$$

2.2   *Simulated Results of The Proposed Filter*

The scattering parameters of the optimized filter are demonstrated in Fig. 4. It is apparent that the filter is a multiband band-pass filter with three resonance frequencies in the 31–39 GHz range. The resonance frequencies of the three bands are 32.32 GHz, 35.75 GHz, and 38.12 GHz. The return losses reach levels of about -35 dB, -25 dB, and -32 dB for the three bands, respectively. The octagonal resonators' corner cuts supply current flow while obstructing flow around the rings. Fig. 5 displays

8
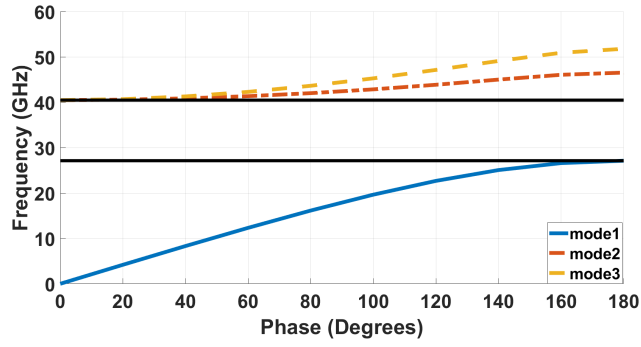
(a)
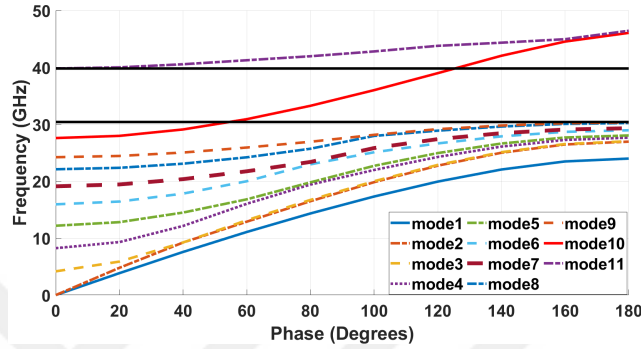
(b)

Figure 2. Dispersion diagram of (a) unit cell (b) supercell

the designed filter's surface current distributions. It is clear that depending on the resonant frequency, the highest current values are generally obtained at the outer RR and sometimes at the inner RR.

The corner cut gap value "z" is another crucial dominating component that significantly influences the resonance frequencies. An optimal value of 0.4 mm produces the triple-band response. It is crucial to note that we took into account a broad range of z values, and Fig. 6 presents the most noteworthy situations.

The effects of the "d" distance between the two octagonal patches are shown in Fig. 7. It is evident that only the middle-frequency response is impacted by changing the distance. It has no effect on the other frequency bands, though. Decreasing the d value shifts the middle frequency towards higher frequencies.

The relative placement of the corner cuts of the inner and outer rings is another crucial parameter in order to obtain multi resonances. The positions of the outer corner cuts are changed with angles $\theta = 0°$, 30°, and 60° counter-clockwise (CCW) while keeping

9
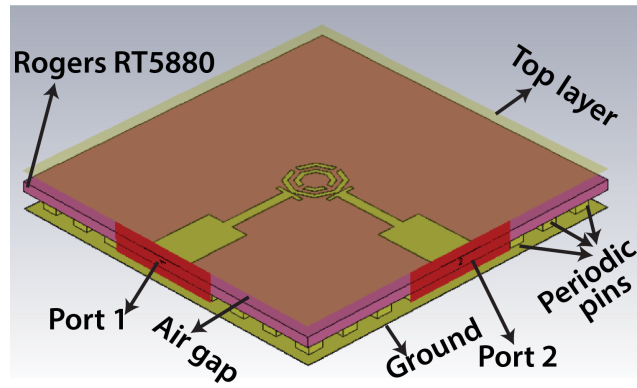
(a)
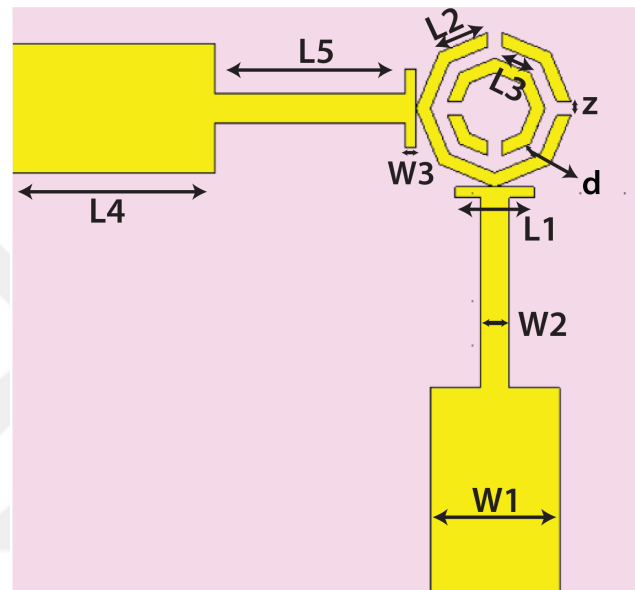
(b)

Figure 3. Proposed (a) IMGWG filter (b) filter resonator
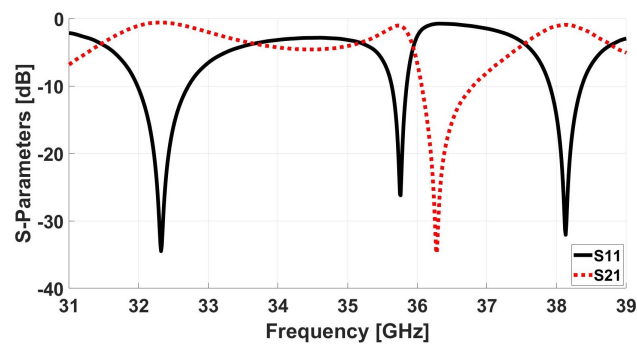
(a)

Figure 4. Scattering parameters of the proposed filter

the inner ring fixed. This process is repeated for the inner corner cuts while keeping the outer ring fixed. The responses of the filter are shown in Fig. 8. The change of
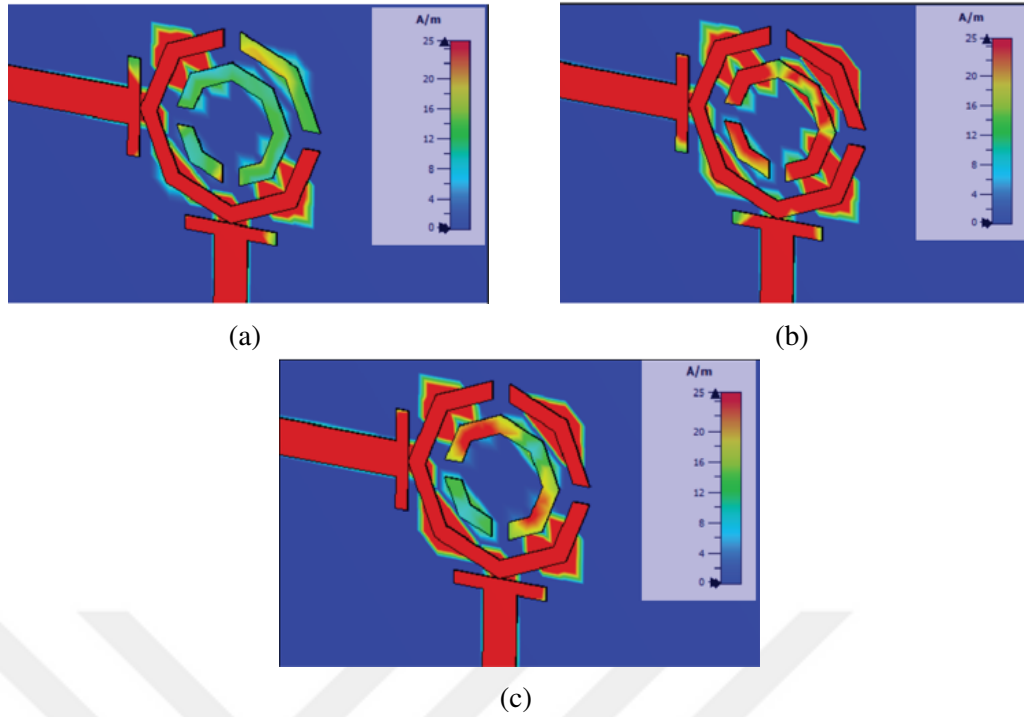
Figure 5. Proposed filter surface current distribution at (a) 32.3 GHz (b) 35.7 GHz (c) 38.1 GHz
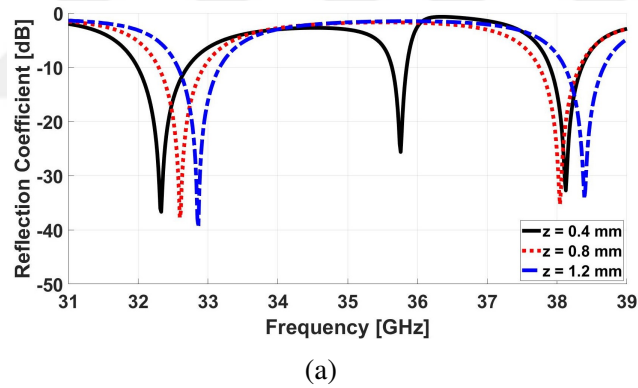
Figure 6. Simulated reflection coefficient for different z values

outer corner cuts shows a triple-band behavior for $\theta = 0°$, a double band for $\theta = 60°$, and a single band for $\theta = 30°$ as depicted in Fig. 8 (a). Changes do not affect the upper and lower resonant frequencies for inner cut rotation. However, the change in the inner corner cuts results in a significant change in the middle resonance. This effect provides a double band characteristic of this filter as shown in Fig. 8 (b).

11

(a)
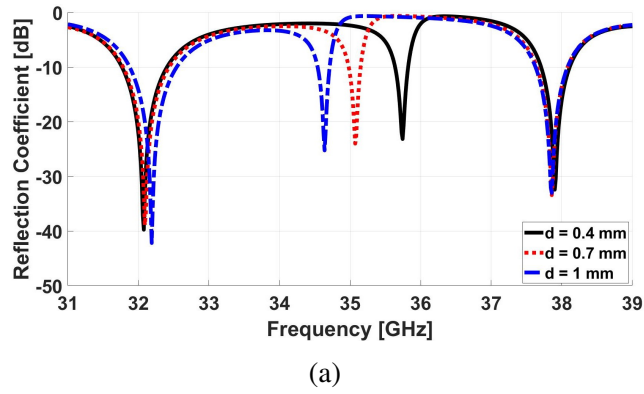
Figure 7. Simulated reflection coefficient for different d values

(a)

(b)
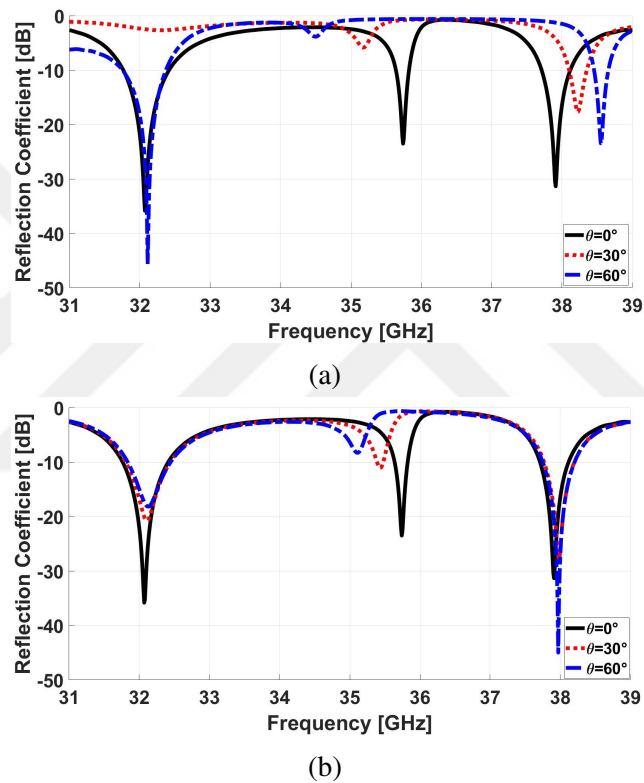
Figure 8. Reflecion coefficients for various corner cut positions (a) outer (b) inner

2.3 *Conclusion of IMGWG-based Triple-band BPF*

A triple-band BPF is designed using IMGWG feeding network for Ka-band applications. The double octagonal ring resonator is developed and optimized to obtain a triple-band behavior. The obtained operating resonant frequencies are 32.32 GHz, 35.75 GHz, and 38.12 GHz with about -35 dB, - 25 dB, and – 30 dB return losses, respectively. The filter exhibits low insertion losses of about 0.6 dB, 1.1 dB, and 0.9 dB at the three resonant frequencies, and the obtained -3 dB fractional band responses

12

are 5.2%, 1.37%, and 2.46% respectively. The effects of spacing between the inner and outer rings and the relative placements of the inner and outer corner cuts are considered in this study to achieve the required properties of the designed filter. The proposed design is suitable for Ka-band applications.

CHAPTER 3 : OPTIMIZING RIDGE GAP WAVEGUIDE BASED SLOT ANTENNA GEOMETRIES FOR MAXIMUM GAIN AND BANDWIDTH FOR SATELLITE APPLICATIONS

This work proposes different V-band antennas optimized to operate at 70 GHz with various geometric slots. The development is based on SIGW technology. Five geometries are considered, namely, rectangular, circular, hexagon, T-shape, and U-shape, with the target of maximizing the realized gain and bandwidth. The Finite Difference Time Domain (FDTD) technique is used to optimize the design parameters (CST studio simulator). The overall size of the developed antenna is 8.4 x 7.2 x 0.87 mm^3. The maximum obtained realized gain is found to be 10.98 dBi for the antenna with a rectangular slot. The circular slot antenna shows the highest $S_{11} <$ -10 dB bandwidth of 5.35 GHz in the range 66.53 - 71.88 GHz. The developed slot antennas are very appropriate for point-to-point wireless communication systems and inter-satellite and mobile satellite applications. The development process of the proposed work is summarized as follows:

- SIGW feeding network and antenna design

- Simulated results of the proposed antennas

- Conclusion of SIGW-based slot antennas

3.1 *SIGW Network and Antenna Design*

The SIGW is made up of two parallel substrate layers which are both connected to the ground layer, one of which contains periodic texturing to prevent wave propagation in all directions but only along the ridge. The second is the gap layer where the EM waves travel in a quasi-TEM mode. The unit cell of the periodic structure comprises a mushroom patch on the top of the substrate which is connected to the bottom ground layer using vias. The optimized height of the via is 0.508 mm, while the upper substrate layer height is 0.254 mm and the width of the ridge is 0.632 mm. Both layers are filled with Rogers RT5880 (ε_r =2.2 and tanδ = 0.0009). The structure of the unit cell is shown in Fig. 9 (a). The supercell is designed by repeating the unit cell on the two sides of the ridge with a repetition period of 1.2 mm as shown in Fig. 9 (b). Based on these dimensions the stop band of the supercell is from 42 to 87 GHz which covers the V-Band. The dispersion diagram of the unit cell and supercell are shown in Fig. 9 (c) and (d), respectively. One can notice that the Quasi-TEM mode is propagating

14

over the ridge on the same frequency band. The scattering parameters of the SIGW feeding network are depicted in Fig. 10. One can see the propagation of the wave over the ridge along the gap over these frequency bands. The surface current distribution is demonstrated in Fig. 11 at three different frequencies two of them are out of the frequency band and one of them is within the band.

(a)

(b)

(c)

(d)
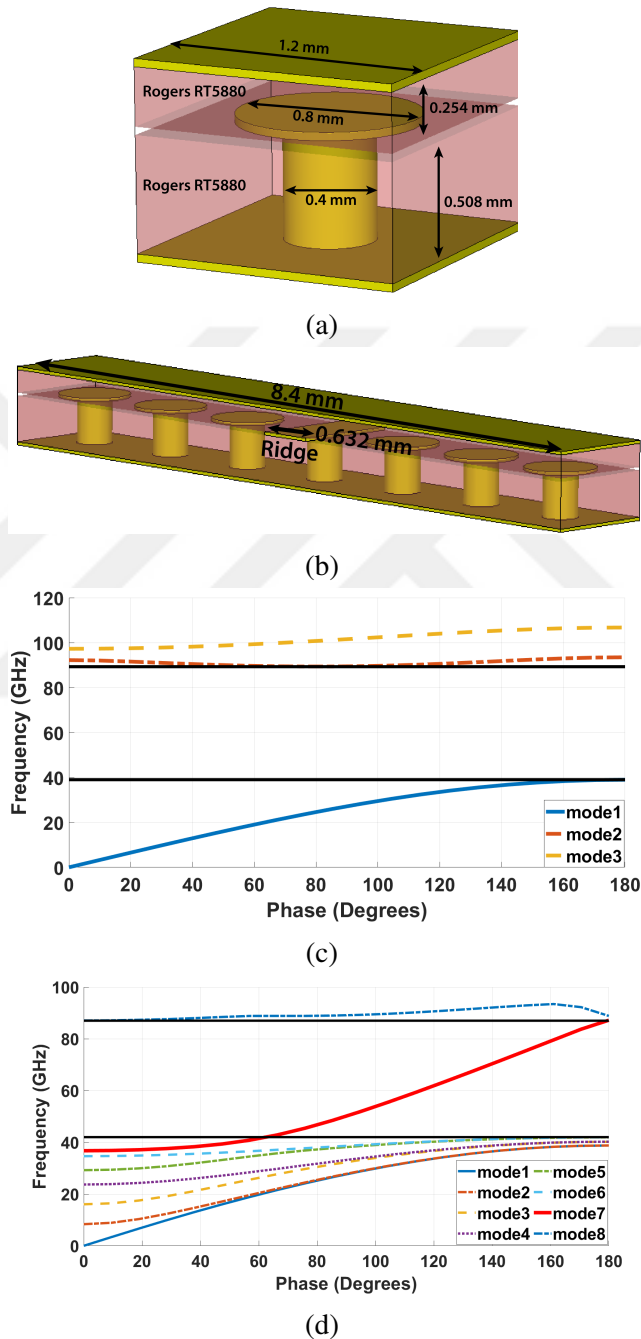
Figure 9. Prposed SIGW technology (a) design of mushroom unit cell (b) supercell design (c) dispersion diagram of the unit cell (d) dispersion diagram of the super cell

In this work, five different radiating slots, namely, rectangular, U- shape, T-shape,
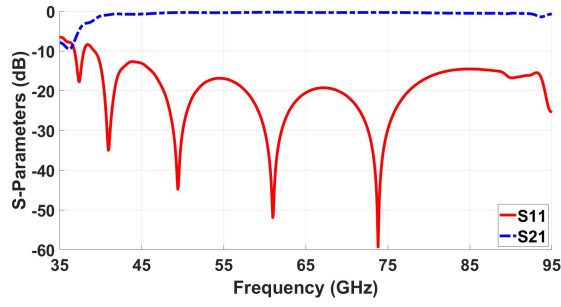
Figure 10. Scattering parameters of the SIGW feeding network

(a)

(b)

(c)
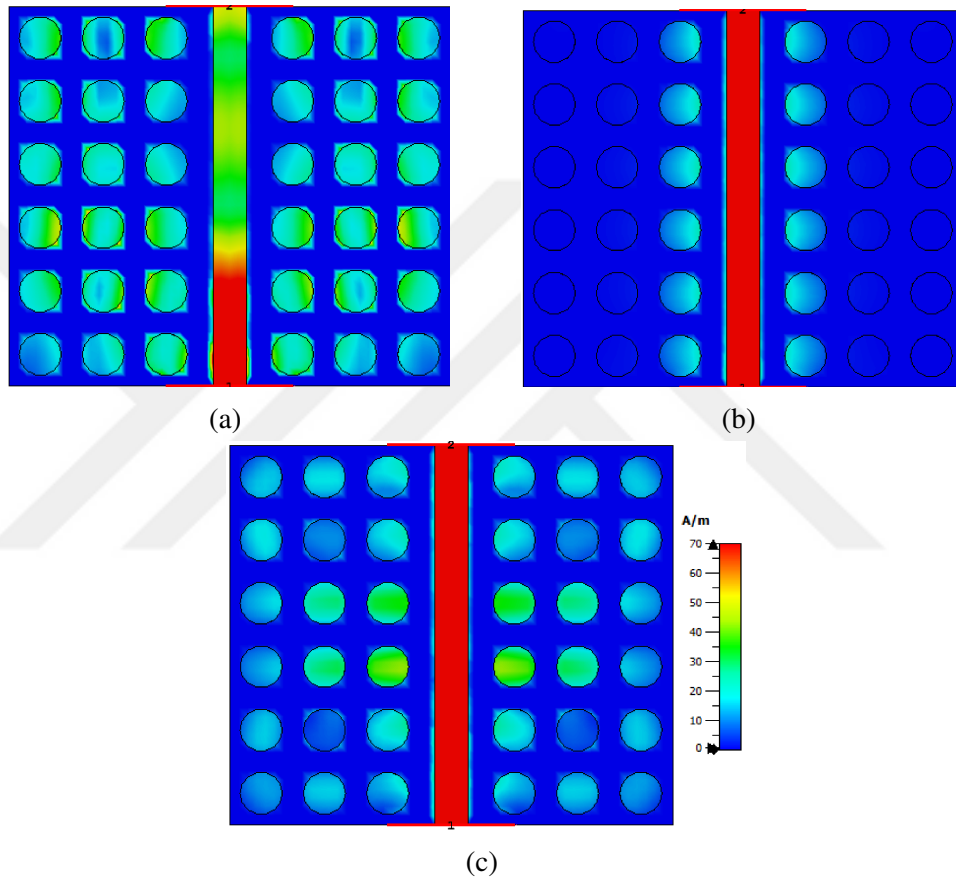
Figure 11. SIGW feeding network surface current distribution at (a) 35 GHz (b) 70 GHz and (c) 90 GHz

hexagon, and circular, and is etched on the top ground layer and fed via an underneath microstrip ridge. Their dimensions are optimized separately for a center frequency of 70 GHz. It is very important to point out that the slot antenna is matched with the ridge using two consecutive quarter transformers as depicted in Fig. 12. The suggested various slot antennas are seen in Fig. 13 and their dimensions are reported in Table 2.

16
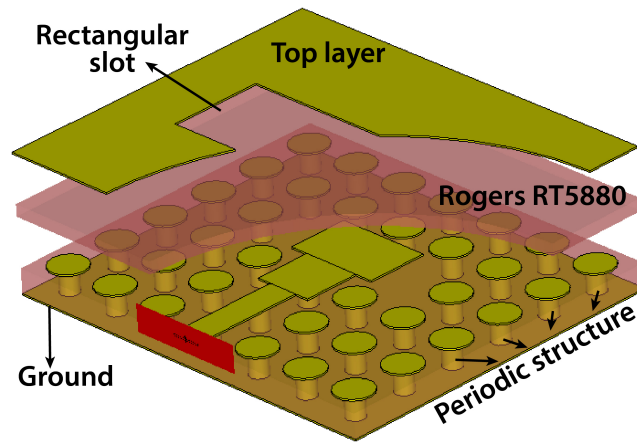
(a)
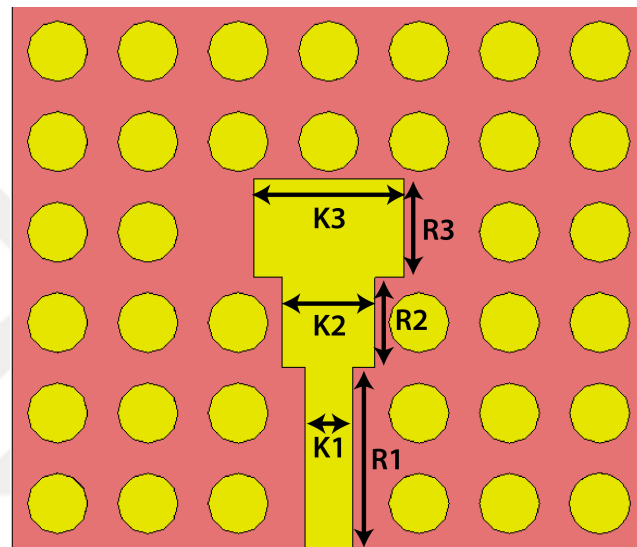
(b)

Figure 12. Proposed design (a) slot antenna (b) SIGW feeding network

Table 2. Parameters of the SIGW antennas

Parameters	K1	K2	K3	R1	R2	R3	L1	L2	L3	L4
Values (mm)	0.632	1.23	2	2.4	1.2	1.3	5.5	2.01	3.84	1.84
Parameters	L5	L6	L7	L8	L9	L10	L11	L12	L13	
Values (mm)	2.7	1.1	3.9	2.1	2.19	2.875	1.3	3.3	7.255	

3.2   *Simulated Results of The Proposed Antennas*

The dimensions and the geometries of the slots are the key parameters in the determination of the operating frequencies of the antenna. The optimization is generally made on the etched shape in order to get the 70 GHz centered resonance frequency. The scattering parameters of the antennas are shown in Fig. 14. The
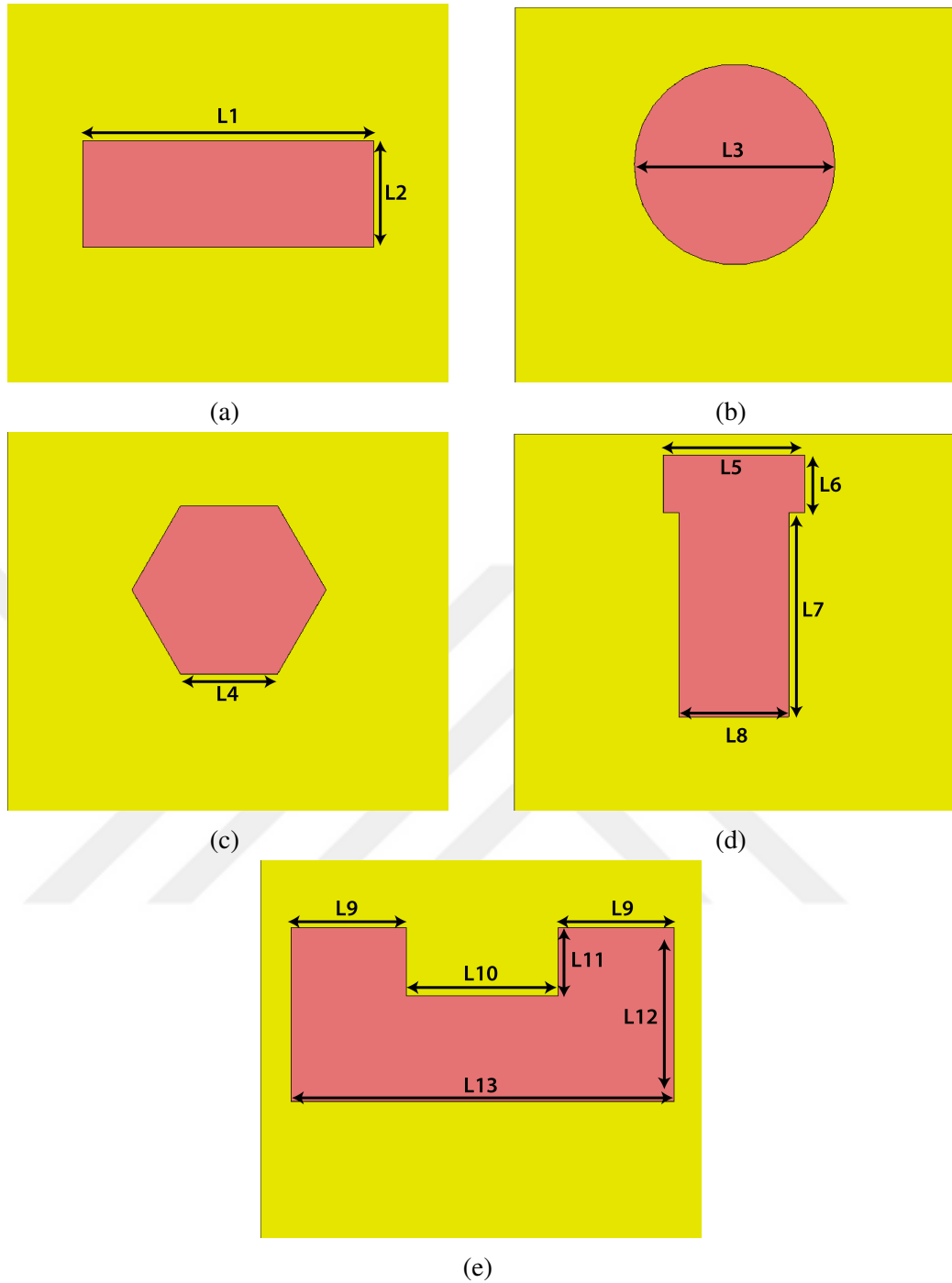
Figure 13. The proposed slot antenna geometries: (a) rectangular (b) circular (c) hexagon (d) T-shape (e) U-shape

circular slot antenna has the widest bandwidth of about 5.35 GHz while the T-shape antenna has the narrowest bandwidth of about 1.57 GHz, and the hexagon shows a bandwidth of about 1.61 GHz. The BW of the rectangular and U-shape are almost the same 3.04 GHz and 3.08 GHz, respectively. The S_{11} values are below the -25 dB level at the 70 GHz resonance frequency for all antennas. It is important to point out that

some of these antenna configurations are convenient to be applied for point-to-point wireless communications which meet the required bandwidth.
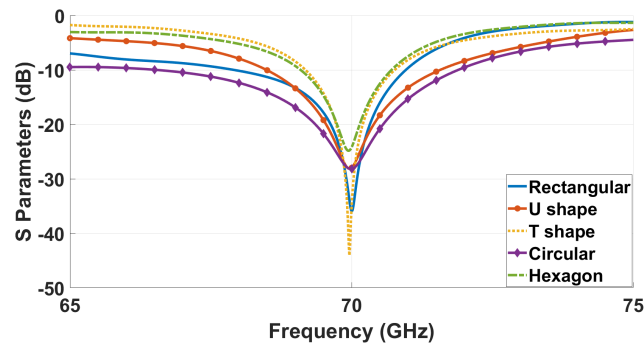
Figure 14. Simulated reflection coefficients of the proposed antennas
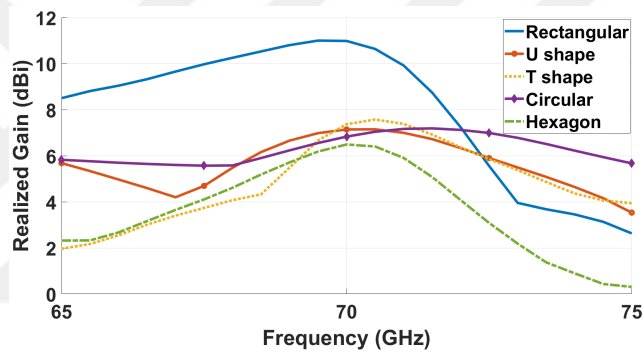
Figure 15. Realized gain of the antennas

The variations of the simulated realized gains with frequencies are shown in Fig. 15. Except for the rectangular slot antenna, all other geometrical shapes have approximately very close gain values in the range of 6.48 - 7.36 dBi. The values of the bandwidths and realized gains are listed in Table 3. The rectangular antenna has a maximum gain of about 10.98 dBi. The gain of the rectangular antenna is enhanced by about 3.61 dBi in comparison to the T-shape antenna.

The rectangular slot is unlike the other geometries in terms of realized gain. The difference is clarified by either the difference in the total antenna efficiency or by the directivity. The total efficiencies are described in Fig. 16, and the directivities of the antennas are shown in Fig. 17. The total radiation efficiencies of all antennas at the resonance frequency are close to 90%. The highest total efficiencies belong to the circular and U-shapes slots with values of 0.95%, and 0.94%, respectively. Although

19
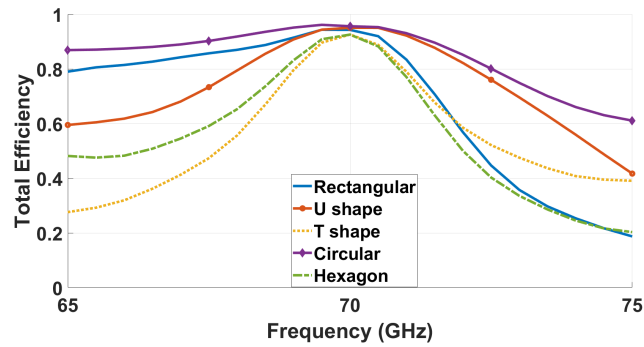
Figure 16. Total efficiencies of the antennas
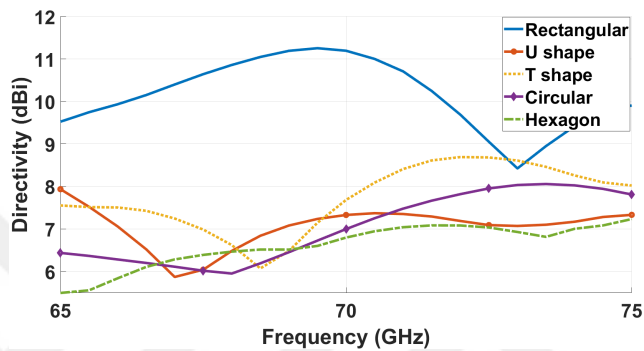
Figure 17. Directivities of the antennas

the efficiencies of the circular and U-shape are higher than the rectangular slot, their gains are lower than the rectangular. In this study, directivity is the dominant factor to determine the gain. It is obvious from Fig. 17 that the directivity of the rectangular slot is higher than those of the T-shape, U-shape, circular, and hexagonal slots by about 3.51 dBi, 3.86 dBi, 4.19 dBi, and 4.39 dBi, respectively.

Table 3. Simulated SIGW antenna results

Slot Shape	Freq. Range (GHz)	BW (GHz)	Realized Gain
Hexagon	69.09-70.7	1.61	6.49
Circular	66.53-71.88	5.35	6.83
U-Shape	68.49-71.57	3.08	7.14
T-Shape	69.19-70.76	1.57	7.368
Rectangular	67.92-70.96	3.04	10.98

The 3D radiation patterns support the high gain values of the rectangular slot as shown in Fig. 18. It indicates that the rectangular slot focuses on narrower beam areas in comparison to the other slots. The other slots have similar 3D radiation patterns that confine to wider directions.

The surface current distributions of the antennas are shown in Fig. 19. The current is outlined accurately at the ridge and the edges of the slots (marked in red). The current densities show a noticeable increase around the edges of the slots.

3.3 *Conclusion of the RGW-based Slot Antennas*

In this study, five different V-band slot antennas based on SIGW are presented. The developed antennas are compact in size with overall dimensions of 8.4 x 7.2 x 0.87 mm^3. Different slot geometries are considered, namely, rectangular, circular, hexagon, T-shape, and U-shape. All considered slot designs perform highly efficient with total radiation efficiencies above 90%. The realized gains of all designs are between 6.49 - 10.98 dBi, with the rectangular slot being the best design in terms of realized gain (about 10,98 dBi). Based on the Federal Communications Commission (FCC) frequency assignments, the frequency range is between 66-71 GHz our developed antennas are very suitable for mobile satellite and inter-satellite applications. The bandwidth of the antennas are varying between 1.57 - 5.35 GHz with fractional bandwidths of 2.24% - 7.73% depending on the etched shape. This shows these antenna designs are as well suitable for point-to-point wireless communication.
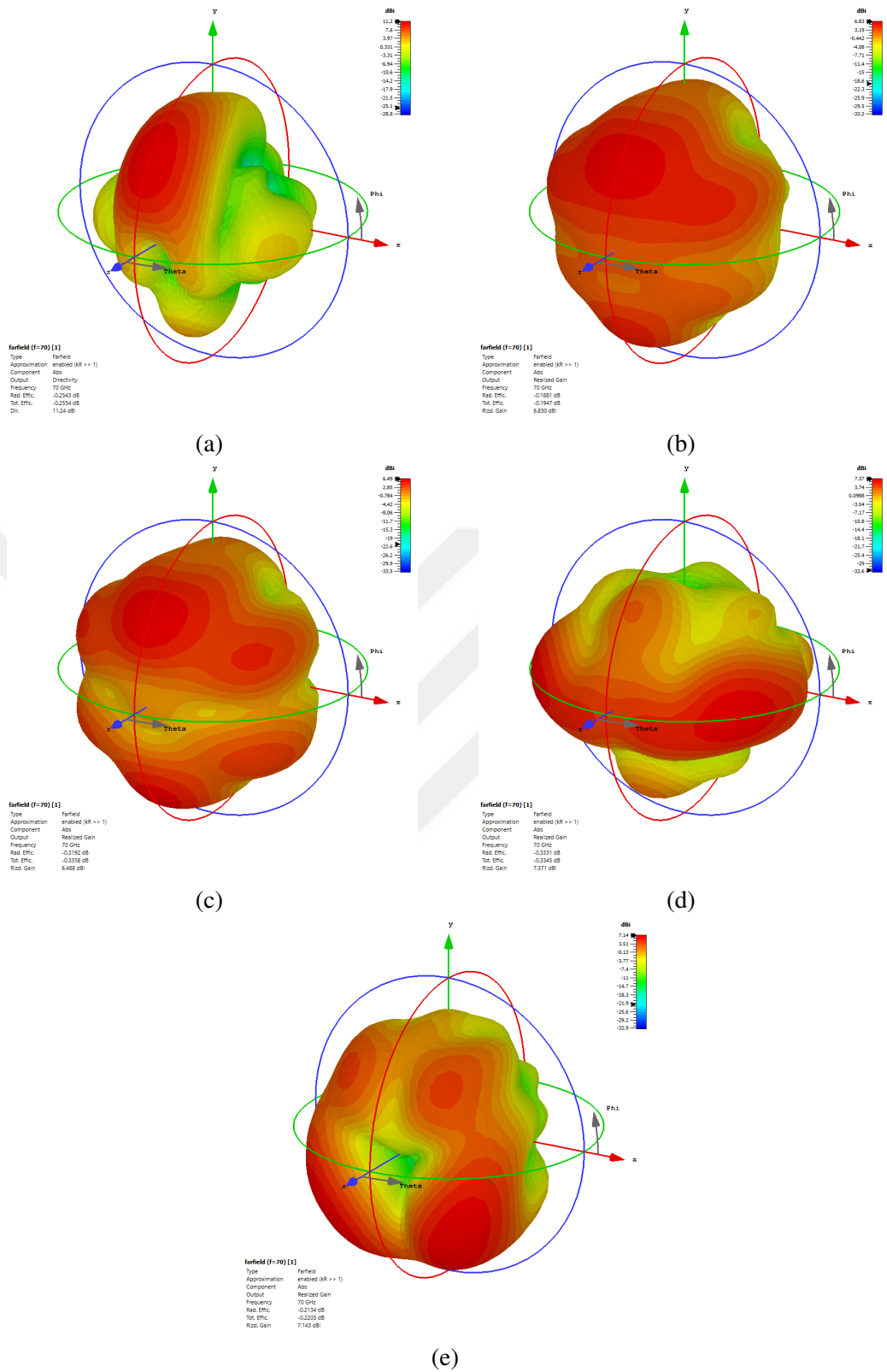
Figure 18. 3D radiation pattern at 70 GHz: (a) Rectangular (b) Circular (c) Hexagon (d) T-shape (e) U-shape
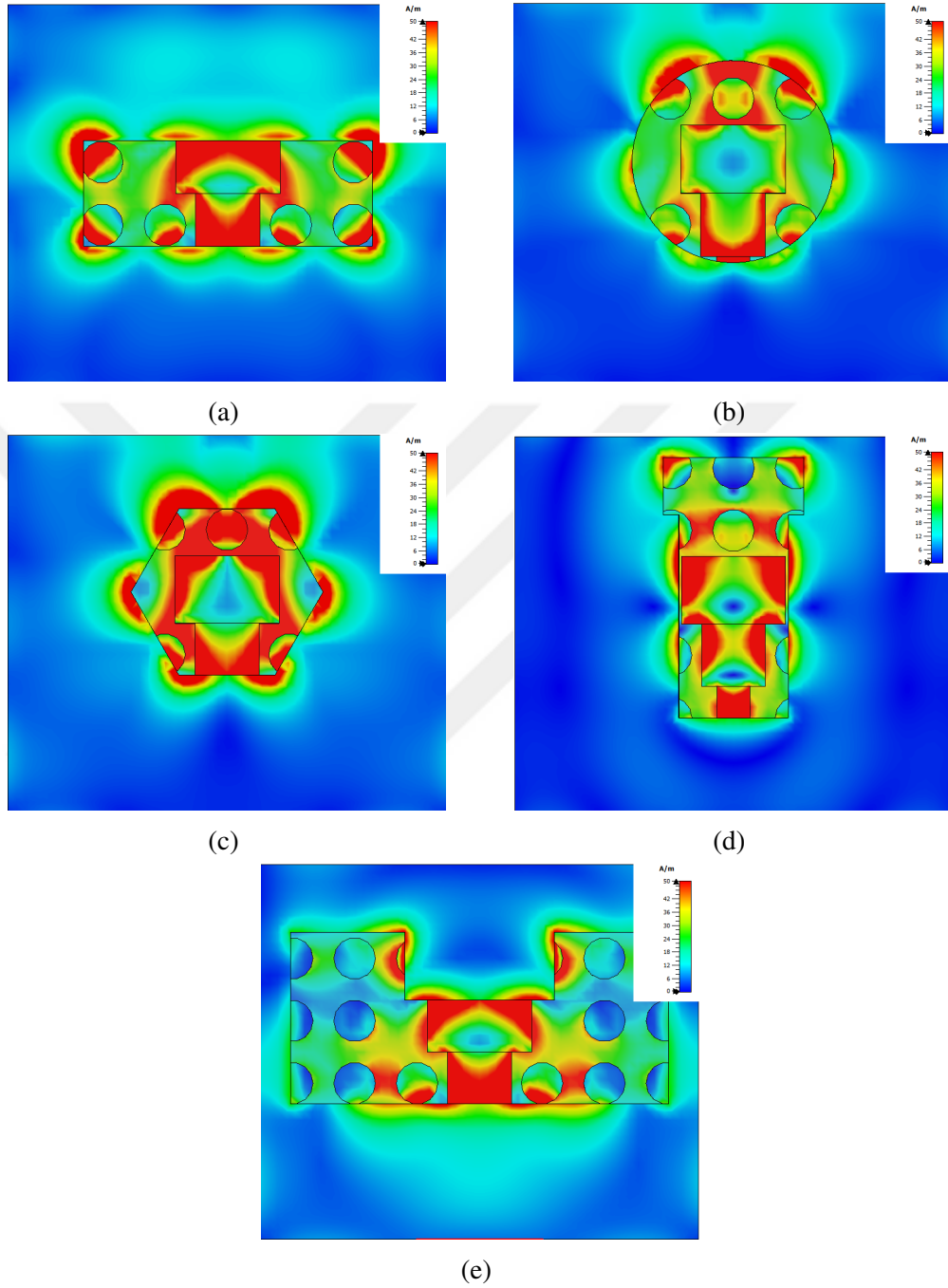
Figure 19. Surface current distribution at 70 GHz for the different designs: (a) Rectangular (b) Circular (c) Hexagon (d) T-shape (e) U-shape

CHAPTER 4 : UWB SIGW-BASED FOUR-PORT MIMO ANTENNA FOR V/W-BAND APPLICATIONS

In this work, we develop a new four-port multiple-input multiple-output (MIMO) antenna system for applications in V and W frequency bands based on SIGW technology. The antennas are suitable for use in automotive radar and inter-satellite applications in the range of 72.7 to 79.5 GHz. The design parameters are optimized using the Finite Integration Time-Domain (FITD) method. The MIMO antenna is composed of four rectangular radiating slots, they are positioned in three different configurations, namely, orthogonal to each other, rectangular, and linear. Each antenna element is fed by a low-dispersion SIGW feeding network. About 28.4%, 34.5%, and 32.1% compactness in size are achieved by eliminating the rows for the three configurations, respectively. The obtained results show that the mutual coupling is below -24 dB within the operating frequency band with minimum coupling obtained for the orthogonal configuration. The obtained results of the computed diversity performance parameters are ECC < 0.002, DG > 9.99 dB, CCL < 0.7 bits/s/Hz, ME > -0.7 dB, and TARC < -6 dB. The obtained results demonstrate that the proposed antennas have strong diversity performances in addition to compact sizes. The development process of the proposed work is summarized as follows:

- MIMO system design

- Simulated results of the proposed MIMO structure

- Conclusion of SIGW-based MIMO antenna

4.1 *MIMO System Design*

The design of the MIMO antenna system often begins with the development of a single optimized reference antenna element. In this work, a rectangular radiating slot antenna is used based on the previous study. The only difference is the rectangular slot optimized based on UWB that covers the desired frequency range. The dimension of the SIGW single reference antenna is 7.2 x 8.4 mm^2. The simulated 2D radiation patterns at three different frequencies are shown in Fig. 20. It is clearly seen that the beam width is getting narrower at higher frequencies. The total efficiency and the directivity of this proposed antenna are shown in Fig. 21. The total efficiency is higher than 80% within the operating frequency. It can be noted that the directivity is drastically increasing above 76 GHz. The peak value of the total efficiency and

directivity are 93% and 11.15 dBi, respectively.
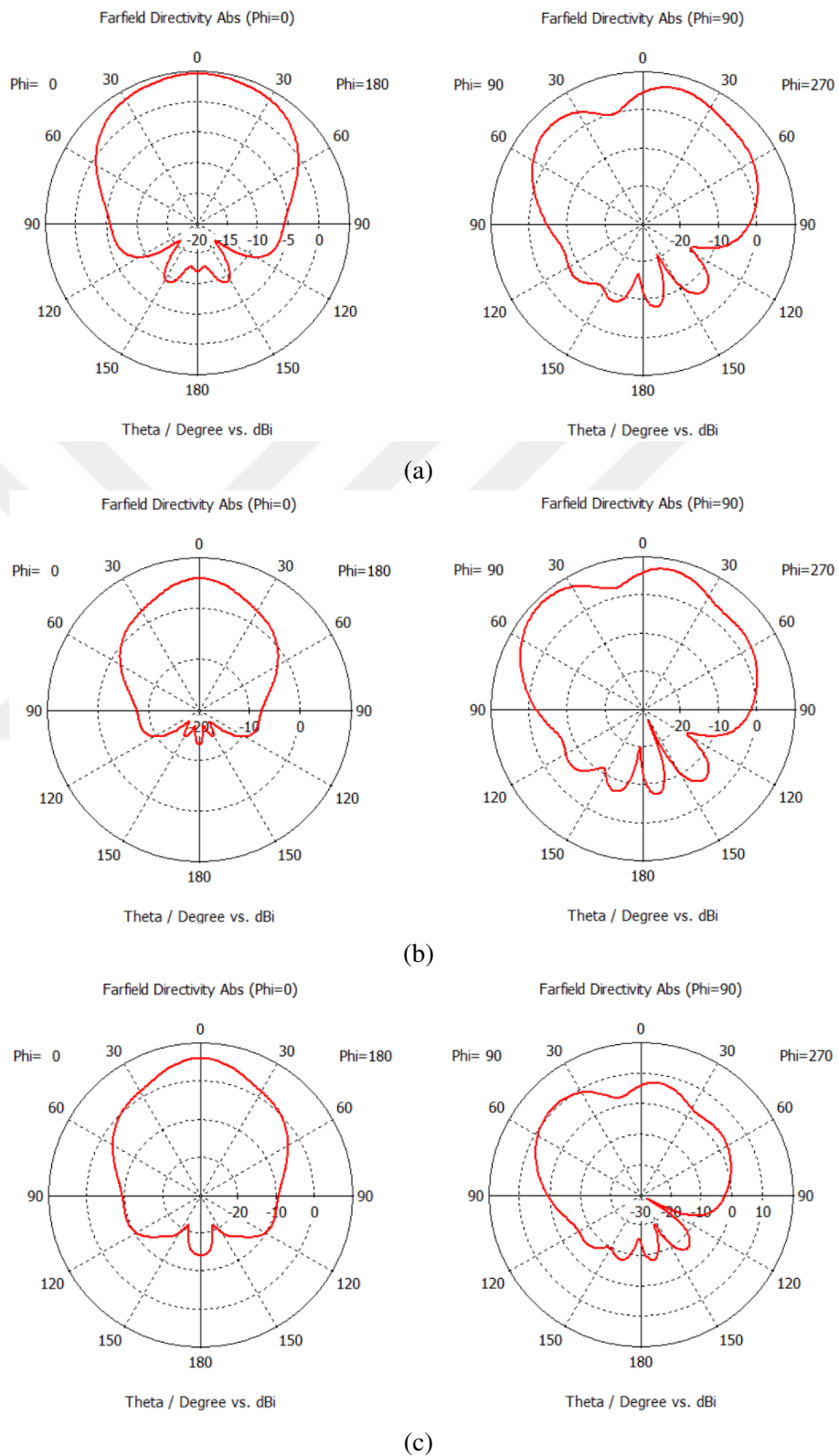
Figure 20. Simulated 2D radiation patterns at (a) 75 GHz (b) 77 GHz and (c) 79 GHz
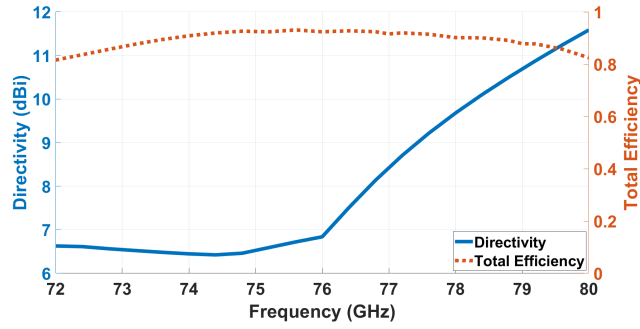
Figure 21. Directivity and total efficiency

The optimized single reference SIGW fed antenna is used to design a four-port MIMO antenna system. Three MIMO configurations are investigated, the first one is the orthogonal configuration in which the antenna elements are configured orthogonally to each other as shown in Fig. 22 (a) and (b). The second one is the rectangular positioning of the antennas as shown in Fig. 22 (c). The last one is the linear configuration where all antennas are placed side by side as shown in Fig. 22 (d). The compactness of the proposed MIMO structure is taken into consideration by eliminating two or three rows of the periodic structure when combining the antenna elements in all configurations. The total compact size of the four-port MIMO antenna structures are 13.2 x 13.2 mm^2 , 12 x 13.2 mm^2, and 7.2 x 22.8 mm^2 for orthogonal, rectangular and linear configurations, respectively.

4.2 *Results and Discussion*

4.2.1 *Antenna Simulation Results and Performance Analysis*

The scattering parameters of the MIMO antennas are depicted in Fig. 23, the -10 dB level of the reflection coefficients covers the frequency range from 72.7 to 79.5 GHz. One of the crucial variables in the MIMO system is the coupling among the antenna elements. Concerning the orthogonal configuration, one can notice that the coupling between all antenna elements is ranging from -24 dB up to -33 dB which is because the distance between slot antennas is nearly the same. However, for rectangular MIMO configuration, the coupling between antenna 1 and antenna 2 is highest because of the shortest distance between them. The lowest coupling is between antenna 1 and antenna 3. Also in the linear configuration, the lowest coupling is achieved between antennas 1 and 4 because of the longest distance. Finally, we can say that the orthogonal polarization in Fig. 23 (a) is considered the best one because the coupling is lower

26
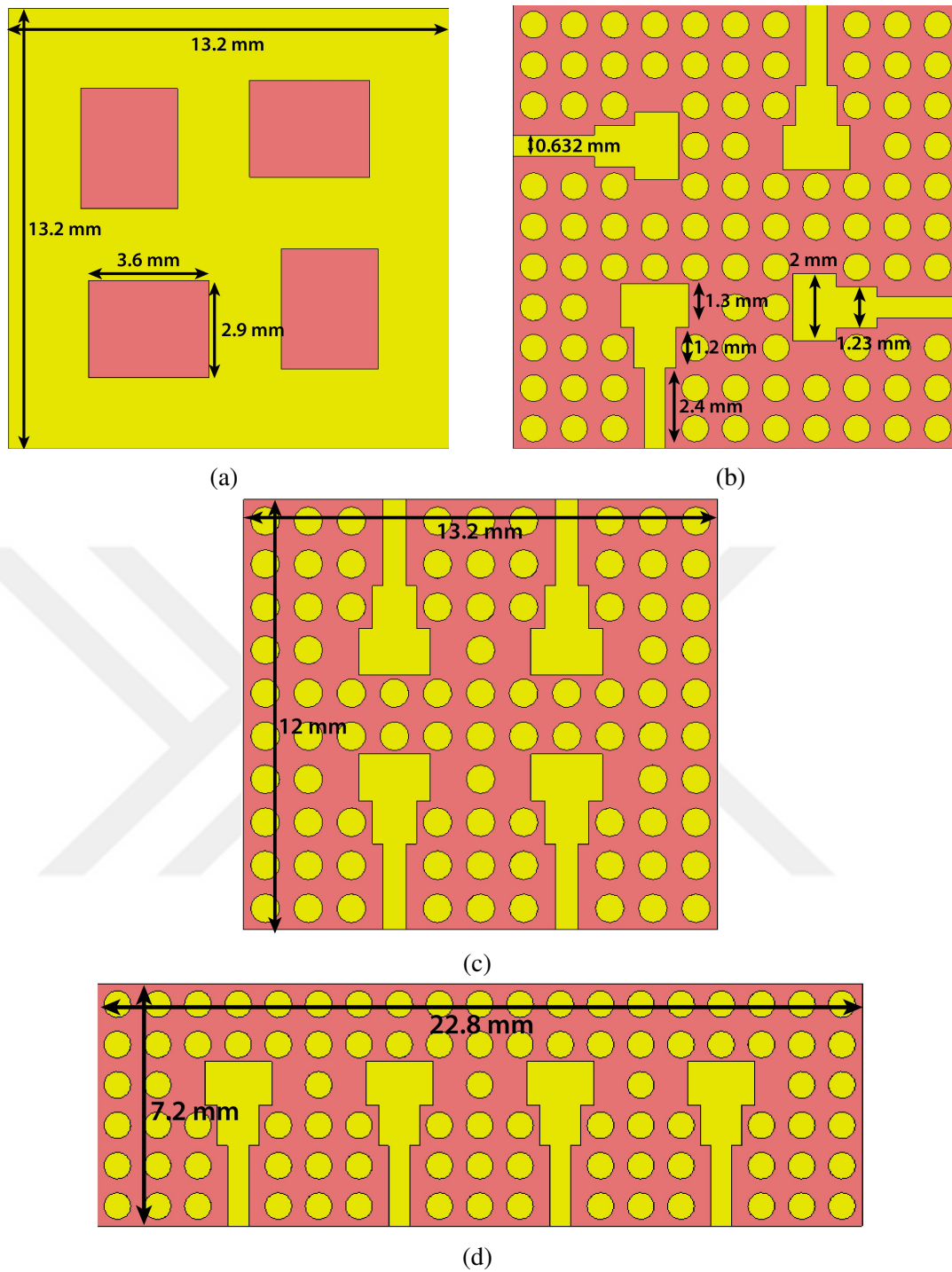
Figure 22. The MIMO system with different configurations (a) Orthogonal with top layer (b) Orthogonal with top layer hidden (c) Rectangular with top layer hidden (d) Linear with top layer hidden

and stable between -24 dB and -33 dB and on average is about -28.5 dB.
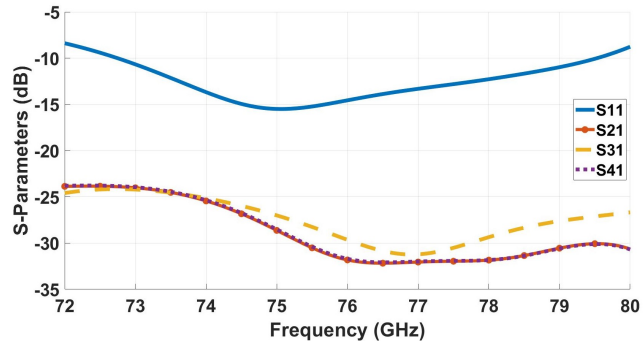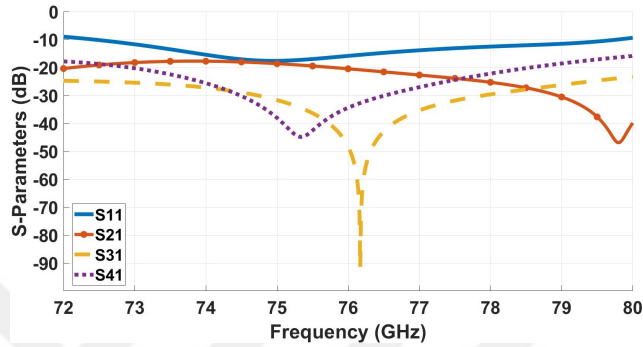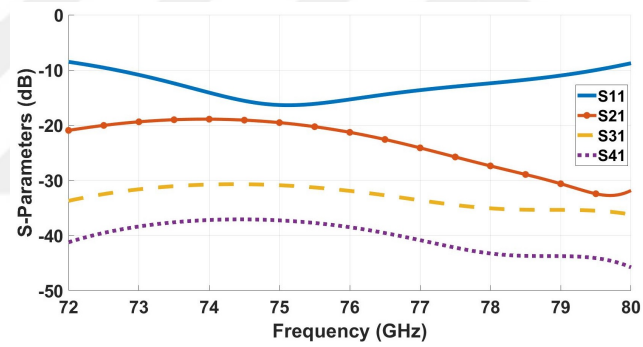
Figure 23. Scattering parameters of the proposed MIMO antenna structure.
(a) Orthogonal (b) Rectangular (c) Linear

4.2.2 *MIMO Diversity Performance*

To study the diversity performance of the proposed MIMO antennas, several crucial metrics are considered and computed, they are namely, ECC, DG, CCL, ME, and TARC.

The ECC is a parameter that describes the correlation among the antenna components. In other words, the ECC depicts the difference in radiation patterns between two antenna elements. As a result, in order to achieve good performance in a MIMO

28
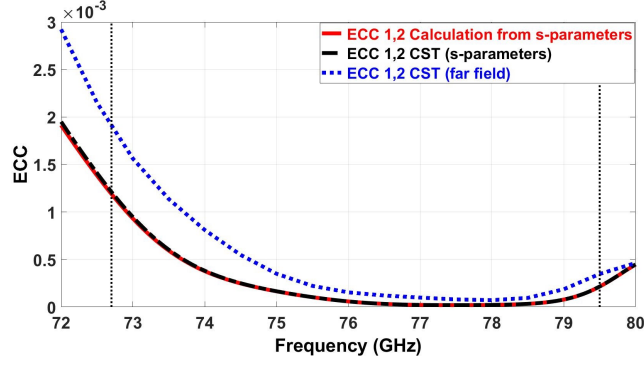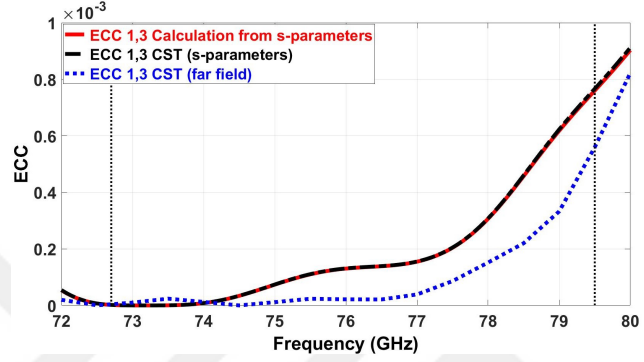
Figure 24. The ECC values of the proposed orthogonal MIMO antenna (a) between antennas 1 and 2 (b) between antennas 1 and 3

system, the ECC values between the antenna components must be small. The ideal case of ECC value is to be zero, for higher MIMO antenna efficiency, the ECC value should be less than 0.5 (Ibrahim and Ali, 2022; Raj et al., 2021). The ECC parameter is computed using two formulae, it can be either derived from the S-parameters (Eq. 1) or from the radiation patterns (Eq. 2) (Blanch et al., 2003).

$$\rho_e = \frac{|S_{ii}^* S_{ij} + S_{ji}^* S_{jj}|}{(1 - (|S_{ii}|^2 + |S_{ji}|^2))(1 - (|S_{jj}|^2 + |S_{ij}|^2))} \tag{1}$$

$$\rho_e = \frac{|\int \int 4 \prod [F_1(\theta, \phi) * F_2(\theta, \phi) d\Omega]|^2}{\int \int 4 \prod |F_1(\theta, \phi)|^2 d\Omega \int \int 4 \prod |F_2(\theta, \phi)|^2 d\Omega} \tag{2}$$

Fig. 24 demonstrates the ECC values of the orthogonal configuration using the S-parameters and the far-field values. It can be seen that all ECC values are (ρ_e) < 0.002.

The metric DG is derived from ECC; the correlation and diversity gain are inversely proportional to each other. The DG is computed using Equation (3) (Rosengren and
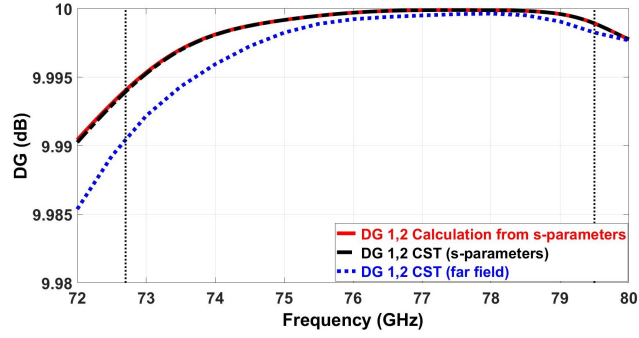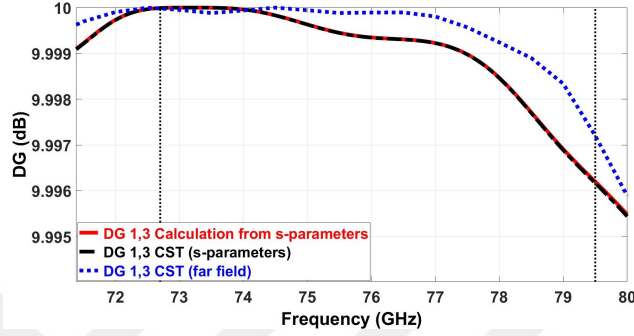
Figure 25. The DG values of the proposed orthogonal MIMO antenna. (a) between antennas 1 and 2 (b) between antennas 1 and 3

Kildal, 2005). According to the DG values, a decrease in the transmitted power will not significantly affect the performance of MIMO if a specified value of 10 dB is reached or is near to it. Our results show that the DG values for the full operational bandwidth are near 10 dB as shown in Fig. 25, which fulfills the required standards.

$$DG = 10 * \sqrt{1 - |ECC|} \qquad (3)$$

Another performance metric is the CCL, which designates the ideal information transfer rate. Equation (4) mathematically expresses the CCL value for a four-port MIMO antenna system. The obtained result is displayed in Fig. 26 and shows strong performance as well. The obtained CCL values are less than 0.7 bit/s/Hz for all operating frequency band. A lower CCL value indicates a signal that is simpler to be transferred with fewer losses (Masoodi et al., 2021). The lowest obtained CCL value is below 0.2 bit/s/Hz.

$$C_{loss} = -log_2 det(X^R) \qquad (4)$$

where,

$$X^R = \begin{bmatrix} X_{11} & X_{12} & X_{13} & X_{14} \\ X_{21} & X_{22} & X_{23} & X_{24} \\ X_{31} & X_{32} & X_{33} & X_{34} \\ X_{41} & X_{42} & X_{43} & X_{44} \end{bmatrix} \tag{5}$$

$$X_{ii} = 1 - \sum_{n=1}^{4} |S_{ij}|^2 \tag{6}$$

$$X_{ij} = -(S_{ii}^* S_{ij} + S_{ji}^* S_{ij}) \tag{7}$$
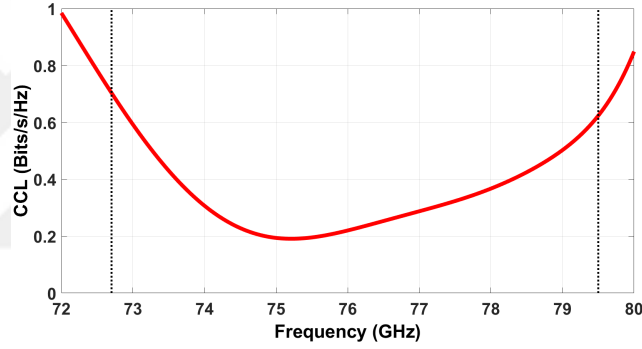
Figure 26. The CCL values for the proposed MIMO antenna

The ME of an antenna is a significant metric that not only informs the developers of the overall antenna efficiency but also of the efficiency imbalance in MIMO systems. The ME is determined as follows:

$$\eta_{mux} = \sqrt{(1 - |\rho_{eij}|)\eta_i \eta_j} \tag{8}$$

where η_i, η_j are the total efficiencies of the ith and jth antenna elements and ρ_{eij} is the magnitude of the complex correlation between the ith and the jth resonator elements (Kumar et al., 2022). As can be seen in Fig. 27, the obtained η_{mux} values of our proposed MIMO designs are higher than -0.7 dB over the operational frequency band. The η_{mux} reaches a maximum value of -0.3 dB at 75 GHz.

The square root of the total incident power divided by the square root of the total
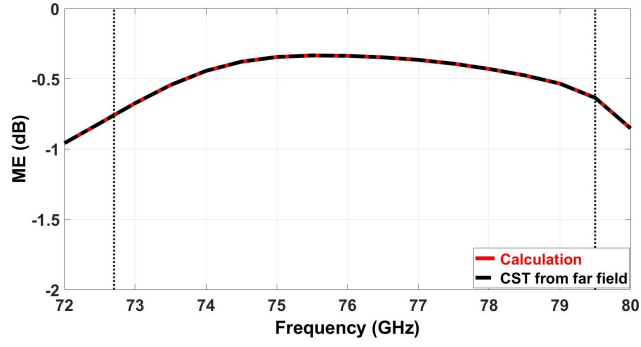
Figure 27. The ME values for the proposed MIMO antenna

reflected power at the same port is known as TARC, and it is derived using the S-parameters and the incident random phase angle θ. Equation (9) shows how to compute the TARC parameter.

$$TARC = N^{-0.5}\sqrt{\sum_{i=1}^{N}|\sum_{k=1}^{N}S_{ik}e^{j\theta_{k-1}}|^2} \tag{9}$$

where N is the number of antennas, S_{ik} denotes the S-parameters and θ is the phase angle of the incoming signals. For every MIMO antenna system, the TARC value needs to be less than 0 dB (Gautam et al., 2018). The currently simulated TARC results show that all the TARC values for various random phase angles are about below -6 dB as demonstrated in Fig. 28.
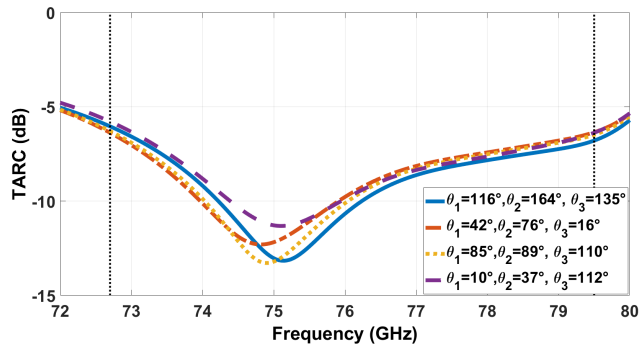
Figure 28. TARC for the proposed MIMO antenna

Table 4 shows the comparison between the proposed MIMO structure with other studies. Comparing our design with other similar systems in the literature reveals that the minimum reported isolation reported values are roughly around -17 dB (Huang et al., 2021; Mathur and Dwari, 2018; Kulkarni et al., 2021; Gomez and Jardon, 2019; Malhat et al., 2022; Kulkarni et al., 2022; Mohanty and Behera, 2021; Dwivedi et al.,

Table 4. Comparisons between the proposed MIMO antenna and other reported studies

Ref. no	No of ports	Max gain (dBi)	Isolation (dB)	ECC	DG	CCL	ME	TARC
Huang et al. (2021)	4	5.1	<16.5	0.01	NA	NA	NA	NA
Mathur and Dwari (2018)	2	5.5	>15	<0.2	9.8	NA	NA	NA
Kulkarni et al. (2021)	4	3.5	>17.5	<0.05	9.98	<0.4	NA	<-10
Gomez and Jardon (2019)	4	4.3	>17	<0.02	NA	NA	NA	<-5
Malhat et al. (2022)	4	10.3	30 (max)	<0.002	9.99	NA	>-1.4	NA
Kulkarni et al. (2022)	4	4	>20	<0.17	NA	NA	NA	NA
Mohanty and Behera (2021)	4	4.5	>15	0.2	NA	<0.4	NA	<-2
Dwivedi et al. (2020)	4	5.5	>18	0.03	9.8	NA	NA	<-10
Proposed work	4	10.5	>24	<0.002	>9.99	<0.7	> -0.7	<-6

2020) while the design offers maximum isolation exceptional values below -24 dB. The obtained ECC and DG values of the proposed work exhibit the best values closely to the ideal case which are approximately 0 and 10 dB, respectively, compared to the reported values in (Huang et al., 2021; Mathur and Dwari, 2018; Kulkarni et al., 2021; Gomez and Jardon, 2019; Malhat et al., 2022; Kulkarni et al., 2022; Mohanty and Behera, 2021; Dwivedi et al., 2020). Despite the fact that the majority of earlier research in the literature did not disclose the ME value, our result is the best among the published studies (Malhat et al., 2022).

4.3   *Conclusion of SIGW-based MIMO antenna*

In this article four-port three different, namely, orthogonal, rectangular and linear SIGW-based MIMO antenna configurations are proposed for automotive radar and inter-satellite applications. About 28.4%, 34.5%, and 32.1% compactness in size are achieved by eliminating the rows for the three configurations, respectively. The fractional bandwidth of the proposed orthogonal MIMO antenna design is approximately 8.95% and the coupling between resonators is below -24 dB. The obtained results of the computed performance parameters ECC < 0.002, DG > 9.99 dB, CCL < 0.7 bits/s/Hz, ME > -0.7 dB, and TARC < -6 dB demonstrate that the proposed antennas have strong diversity performance. The performance of the proposed orthogonal polarized antenna is adequate in every way and is appropriate for wireless point-to-point communications as well.

CHAPTER 5 : DESIGN AND IMPLEMENTATION OF AN RGW BASED UWB ANTENNA ARRAY FOR D-BAND APPLICATIONS

This study presents a new 4 x 1 rectangular slot antenna array based on ridge gap waveguide (RGW) technology for the use of D-band applications. The operating frequency of the proposed array antenna is 140.9 - 157.7 GHz. The Finite Integration Time-Domain (FITD) method is used to optimize the design parameters. Four rectangular slots are placed side by side and the RGW feeding network is used to feed them with minimal dispersion. Quarter-wavelength transformers are used to match the source to the load composed of the antenna array and feeding network. The antenna's overall efficiency is around 95%. The antenna array's maximum gain is about 10 dBi, compared to the single antenna's gain of roughly 7 dBi. The main focus of the current work is the development and analysis of the UWB RGW-based feeding network antenna array system. The development process of the proposed work is summarized as follows:

- RGW feeding network and array antenna design

- Simulation results of the proposed array antenna

- Conclusion of RGW-based array antenna

5.1 *RGW Feeding Network and Array Antenna Design*

Basically, the unit cell consists of two ground metallic conducting layers and the metallic pin connects to the bottom ground, in addition, the upper ground and the pin are separated by an air gap. The pin's height should be equal to approximately or less than ($\lambda/4$), which has a significant impact on the stopband of the intended frequency range. The height of the pin is 0.38 mm and the air gap thickness is 0.15 mm and 0.7 mm is the unit cell periodicity. The stopband of the unit cell is between 112.8 – 231.3 GHz. To activate the propagating Quasi-TEM mode, a supercell is built by positioning a 0.38 mm wide guiding ridge line in the middle of the six rows of unit cells. The supercell's frequency range is roughly 131 – 222.1 GHz. The frequency range clearly narrows by about 27.5 GHz when inserting the guiding ridge in the supercell. Figure (29) shows the unit cell and supercell configurations, whereas the dispersion diagrams are demonstrated in Fig. 29 (c) and Fig. 33 (d), respectively. Constructing the RGW feeding network is the final preparation step before designing a single antenna element.

The feeding network and its scattering parameters are depicted in Figs. 30 (a) and (b), respectively.
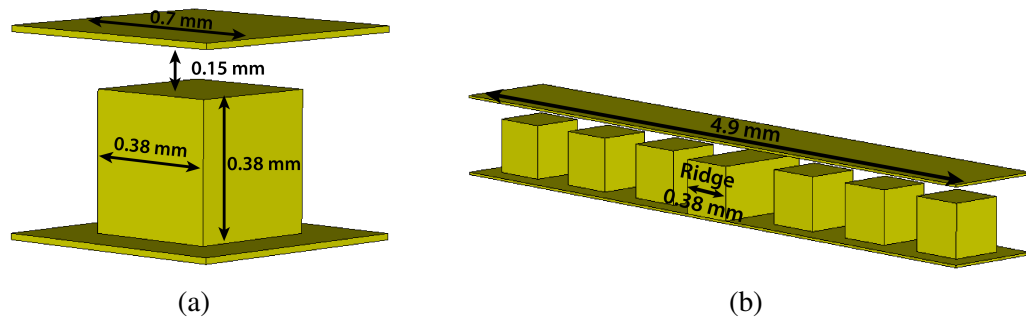
(a)

(b)
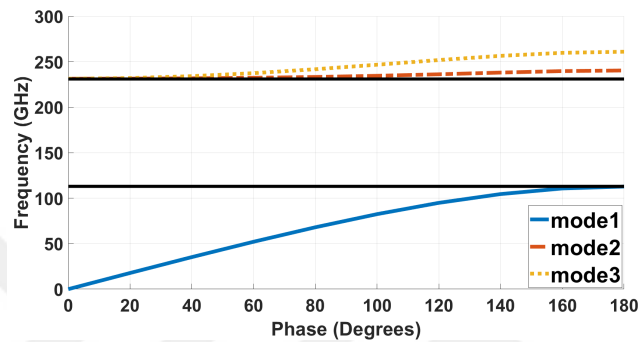
(c)
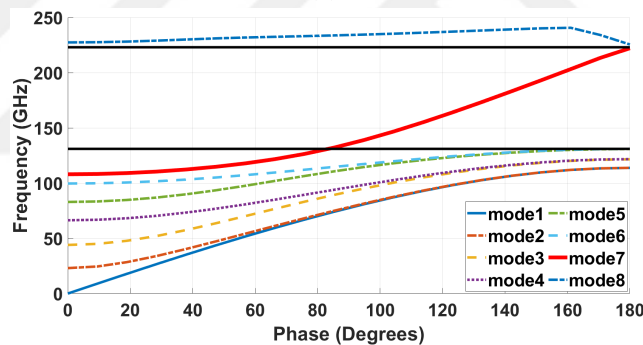
(d)

Figure 29. A Unit cell of RGW feeding network (a) Unit cell design (b) Supercell design (c) Dispersion diagram of the unit cell (d) Dispersion diagram of the supercell

The reference antenna is a rectangular slot etched on the top ground and fed via the RGW underneath. The dimension of the slot is 1.1 x 1.3 mm^2. An optimized rectangular slot is carved on the ridge's body to help with the slot antenna's fine-tuning to match the RGW feeding network to the source. The total size of the antenna including the network is 4.9 x 4.9 mm^2. Fig. 31 (a) shows the proposed reference antenna element.

An antenna array system is designed based on this single reference RGW-fed antenna. Four feeding ridges are connected together while a row of the periodic unit cells is
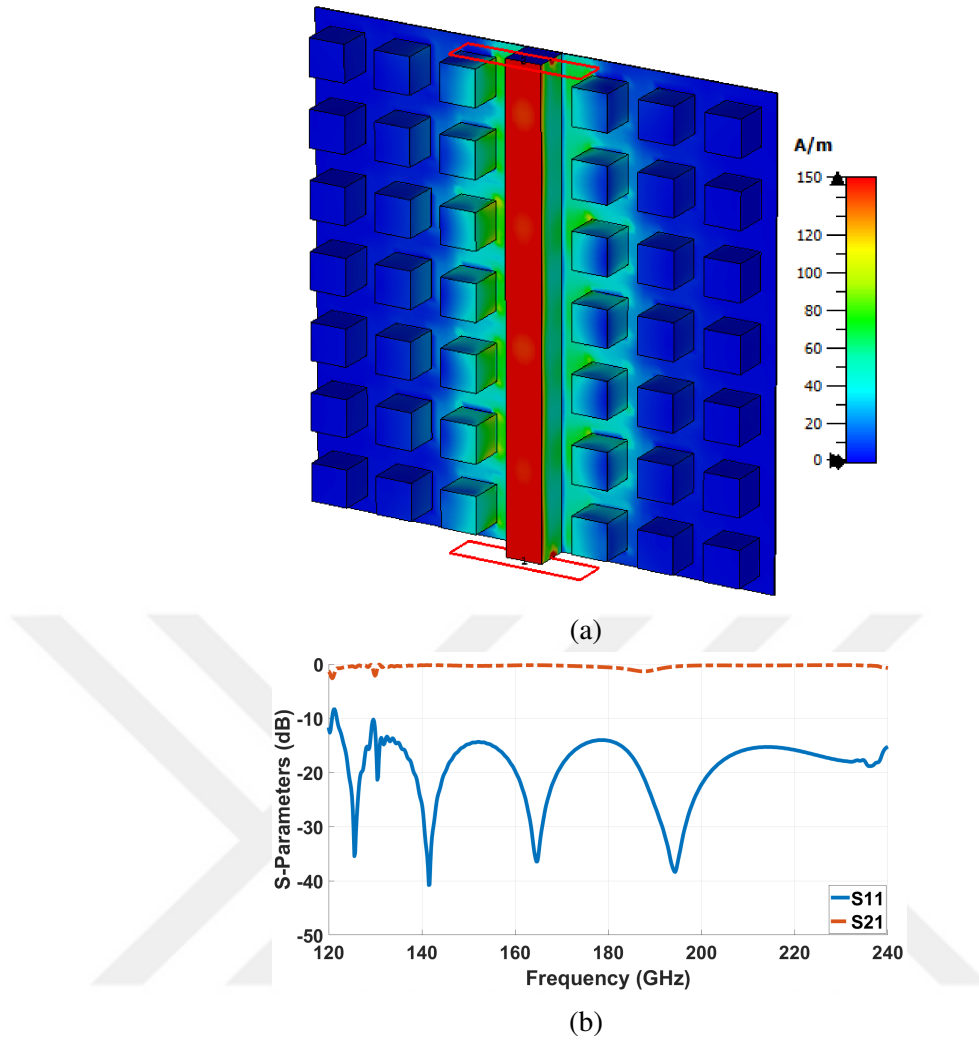
Figure 30. RGW feeding network (a) Surface current distribution at 150 GHz (b) Scattering parameters

between those ridges. Three consecutive quarter wavelength transformers with a length of 0.5 mm are used to match the source to the load represented by the feeding network and the array element. The widths of the transformers are 0.68 mm, 0.58 mm, and 0.48 mm, respectively. The distance between the radiating rectangular slots is 0.3 mm, which is less than $\lambda/2$, resulting in a whole array structure dimension of 7.7 x 9.1 mm^2. Figs. 31 (b) and (c) demonstrate the proposed RGW antenna array.

5.2 Simulations and Results

Fig. 32 depicts the simulated reflection coefficients of the proposed single and array antenna. The simulated bandwidth of the single antenna is $|S_{11}| < $ -10 between 144.9 – 154.2 GHz while the antenna array covers the frequency range from 140.9 to 157.7 GHz with fractional bandwidths (FBW) being 6.22% and 11.25%, respectively. The
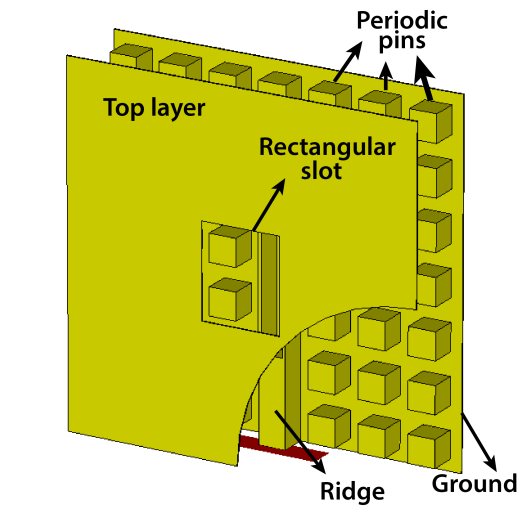
(a)

(b)

(c)
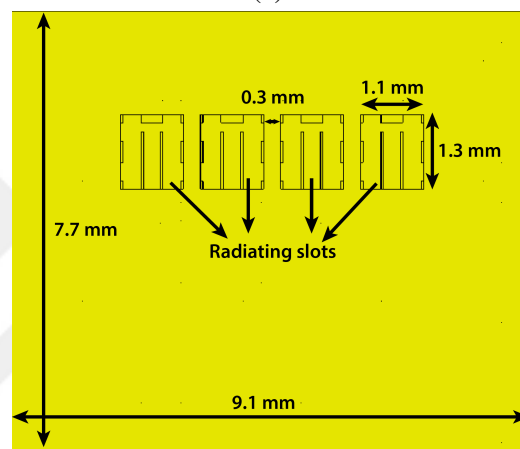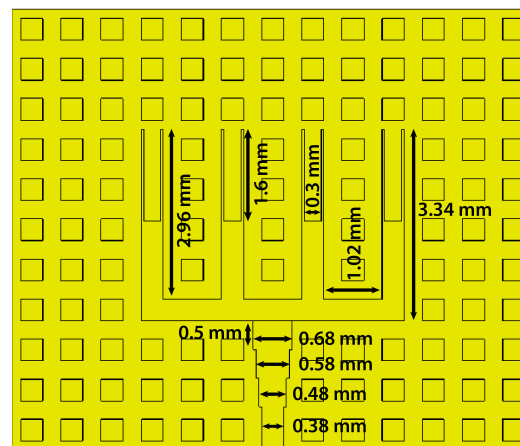
Figure 31. Referance antenna and antenna array (a) Single reference antenna (b) RGW antenna array top layer (c) RGW antenna array with top layer hidden

bandwidth of the antenna array is wider than that of the single reference antenna by approximately 7.5 GHz. This can be emphasized that the structure has two resonances,

an element resonance at 154 GHz and an array resonance at 143 and 154 GHz. Both are superimposed and result in a UWB response.
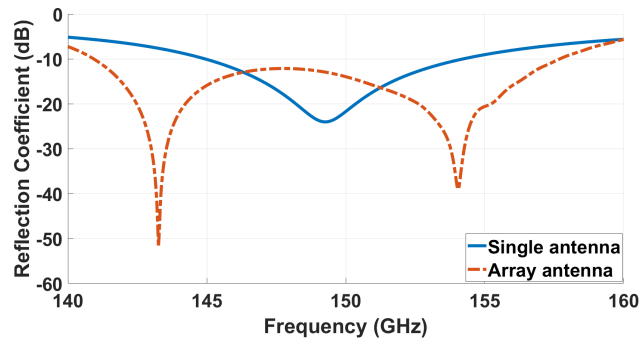
Figure 32. Reflection coefficient of the proposed antennas

It is very important to point out that the optimum bandwidth of the array is achieved after sweeping the via's height for many values as shown in Figs. 33 for selected values of 0.35 mm, 0.38 mm and 0.41 mm. The optimum bandwidth is obtained at h = 0.38 mm, the reason is that at that height the stop band of the array of the via is increasing and covers the whole operating frequency band (140.9 - 157.7 GHz). The realized gain is depicted for different values of the via height as shown in Fig. 34.
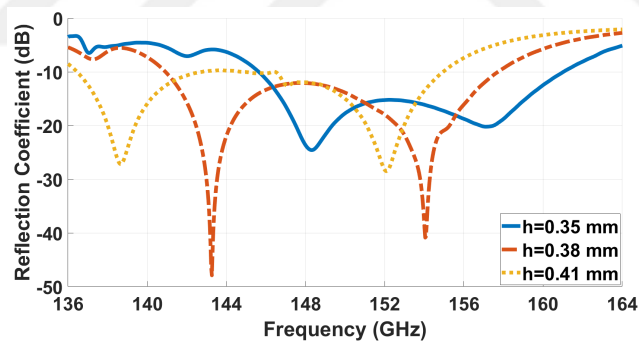
Figure 33. Reflection coefficients of the proposed antennas with different via height 'h'

Fig. 35 displays the directivity and the total efficiency of the simulated reference antenna element and the RGW array. The average directivity of the single antenna is roughly 7.2 dBi, while that of array antennas' is 9 dBi. The average directivity of the single antenna is less than the array antenna by 1.8 dBi. The total efficiency of the single antenna is above 90% while that of the array antenna a 95% efficiency is achieved over the whole operating frequency band. The peak values of the total efficiencies are 0.98 and 0.97 respectively.
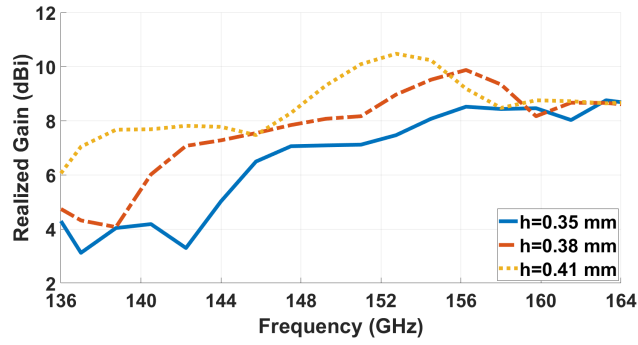
Figure 34. Realized gains of the proposed antennas with different via height 'h'
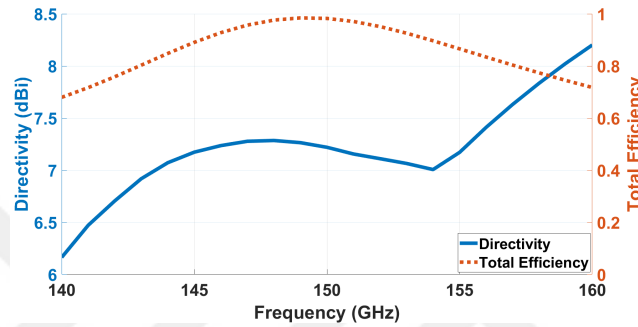
(a)
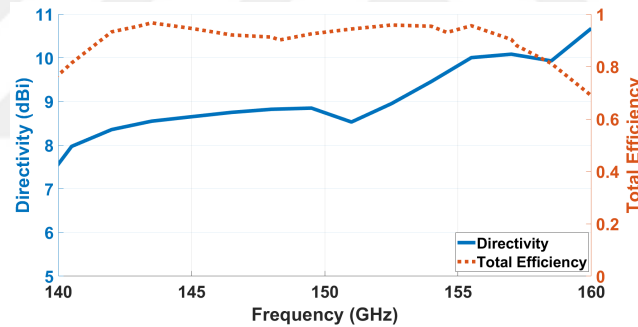
(b)

Figure 35. Directivity and total efficiency (a) Single reference antenna (b) Antenna array

Fig. 36 demonstrates the comparison of the realized gain for the proposed single and array antennas. It is evident that the antenna array gain is higher than the single antenna. The maximum gain of the single antenna is about 7 dBi while the array's gain is 10 dBi. The 3D radiation pattern is depicted in Fig. 37. It implies that the radiation beam concentrates on narrower beam regions at 154 GHz compared to 143 GHz.

The array antenna's current distributions are depicted for the resonance frequencies at
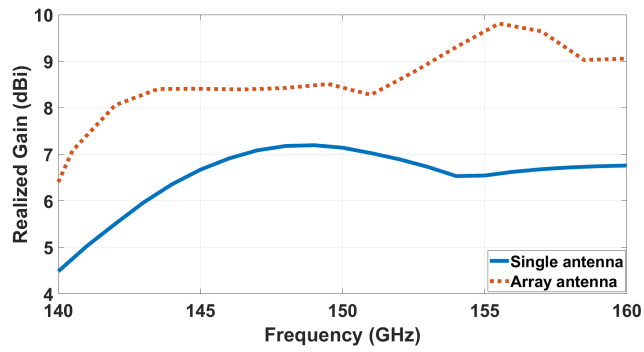
Figure 36. Realized gains of the proposed antennas

(a)

(b)
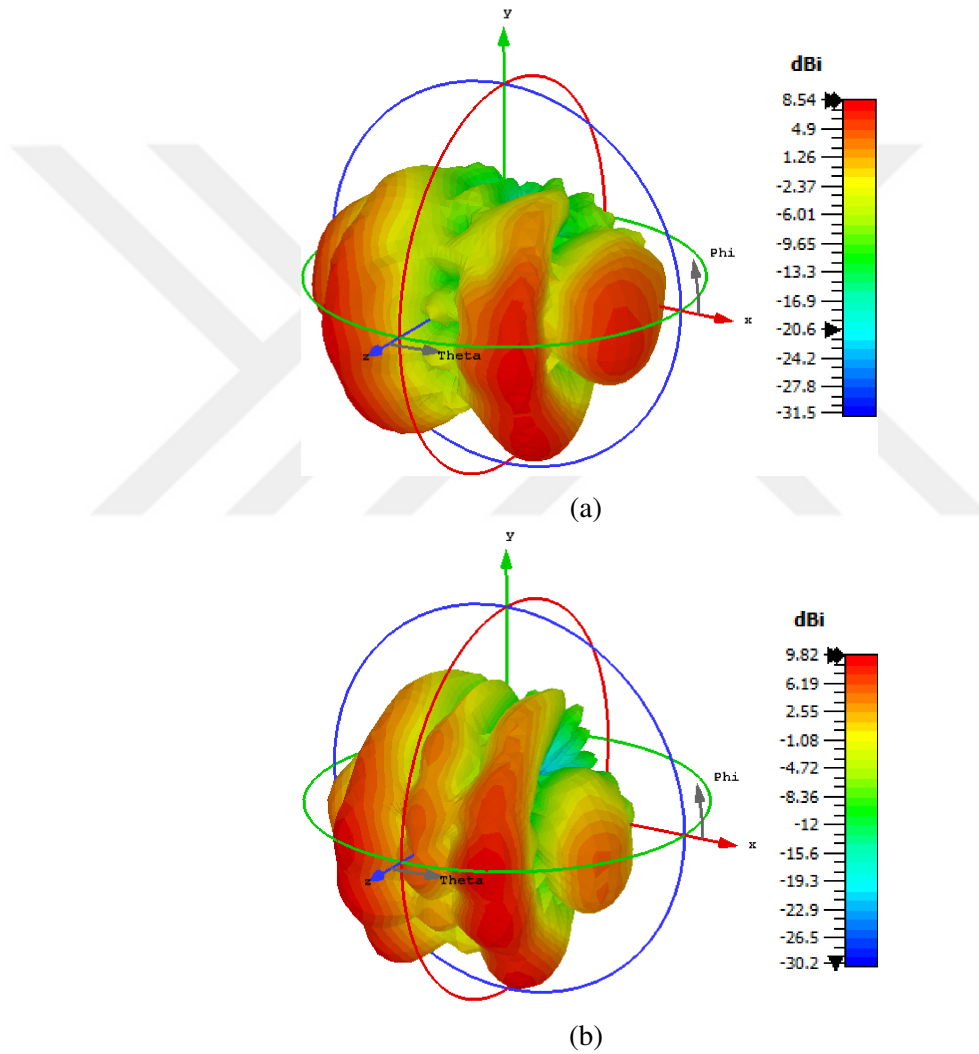
Figure 37. The 3D radiation patterns at (a) 143 GHz and (b) 154 GHz

143 GHz and 154 GHz in Fig. 38. The current density is rising around the center and the edges of the slots and it is highlighted in red.
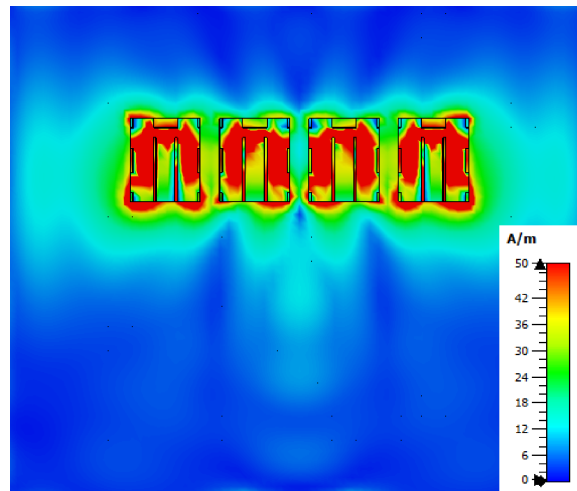
(a)
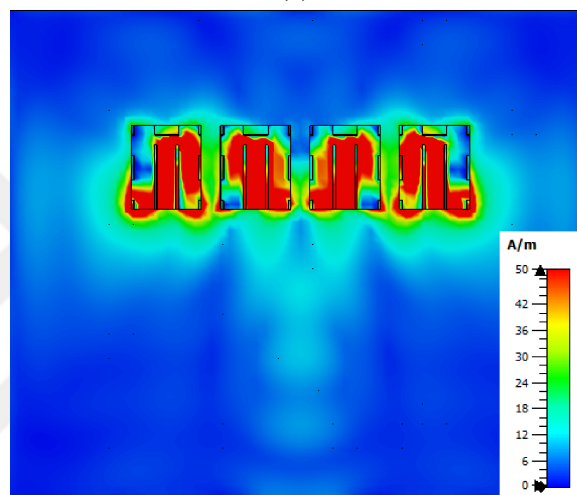
(b)

Figure 38. Surface current distributions at (a) 143 GHz and (b) 154 GHz

5.3 *Conclusion of RGW-based Array Antenna*

In this paper, a new UWB four-slot antenna array fed by the RGW feeding network is presented for D-band applications. Up to the authors' knowledge, no similar antenna designs using RGW in this frequency range are found in the literature. The four ridge feeding lines are connected side by side and matched to the source using three consecutive quarter wavelength transformers. The total size of the proposed antenna array is 7.7 x 9.1 mm^2. The operating frequency of the antenna array is 140.9 - 157.7 GHz. The bandwidth is approximately 17 GHz. The total efficiency of the antenna is around 95% over the whole operating frequencies. The gain of the array is optimized by changing the height of the via surrounding the feeding network. The peak realized gain is around 10 dBi which is higher than the single reference antenna

42

by approximately 3 dBi.

CHAPTER 6 : DGS-BASED ISOLATION ENHANCEMENT FOR RGW FED COMPACT MIMO ANTENNA SYSTEM

In this work, a new four-port compact MIMO wideband antenna based on RGW technology is developed for D-band applications. The single antenna element is designed as a circular matched slot on the top ground of the RGW feeding line. This antenna is considered a reference element of the four-port MIMO structure. Basically, for the sake of measurements the RGW technology requires a transition to a traditional microstrip line. Multi-section quarter-wave transformers are implemented to match the RGW to the transition. The reference antenna sizes are about 4.9 x 4.9 mm^2 without transition and 4.9 x 5.6 mm^2 with the transition. The proposed MIMO antenna is made up of four circularly matched reference antennas. Each consecutive radiating element is positioned orthogonally to each other for the enhancement of the isolation among the four elements. For further reduction of the mutual coupling, we consider five optimized DGS geometries on the upper ground plane. They are namely, line, octagon-centered, square-centered, long line, and triangular shapes. For the sake of verification of the outcomes, two different methods of analysis are considered for the development of the MIMO antenna structure associated with its transition. They are namely, the Finite Integration Time-Domain method (FITD; CST studio simulator) and the Finite Element Method (FEM; HFSS). The total optimized size of the proposed MIMO structure is about 7.7 x 7.7 mm^2. The simulated impedance bandwidth extends from 148 GHz to 161.7 GHz. The use of different DGS geometries is very effective in coupling reductions, the highest coupling level obtained from different DGS geometries is -26.4 dB the lowest level reaches about -96 dB. The maximum realized gain is 7.97 dBi. The simulation results demonstrate outstanding performance throughout the operational spectrum with diversity properties: ECC < 0.0006, DG ~10 dB, CCL < 0.4 bit/s/Hz, TARC ~ -23.4 dB and ME η_{mux}>-1 dB. The development process of the proposed work is summarized as follows:

- RGW feeding network and antenna design

- MIMO antenna design

- Antenna Simulation Results and Performance Analysis

- MIMO diversity performance

- Conclusion of RGW-based MIMO antenna

6.1   *RGW Feeding Network and Antenna Design*

Fig. 39 shows the unit cell of the proposed RGW structure and its dispersion diagram. The dispersion diagram of the unit cell is calculated using the CST Eigen Mode Solver and it covers the frequency range from 117.83 to 240.21 GHz. Placing the guiding ridge instead of only the pin in the center of the EBG structure activates the desired propagating Quasi-TEM mode. The width of the ridge is 0.38 mm and the height is the same as the pin's height. Fig. 40 demonstrates the supercell design and the simulated dispersion diagram. The frequency range in the supercell design is between 137.76 - 226.78 GHz and noticeably seen that the stopband is reduced by approximately 27% because of the ridge.
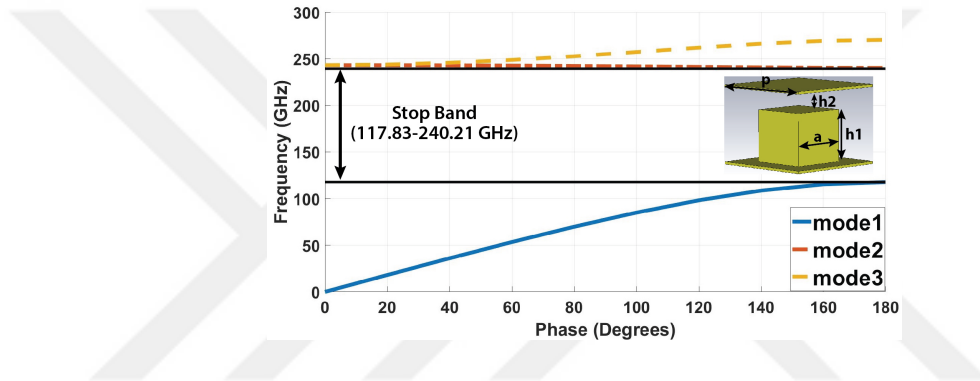
Figure 39. Dispersion diagram of the unit cell
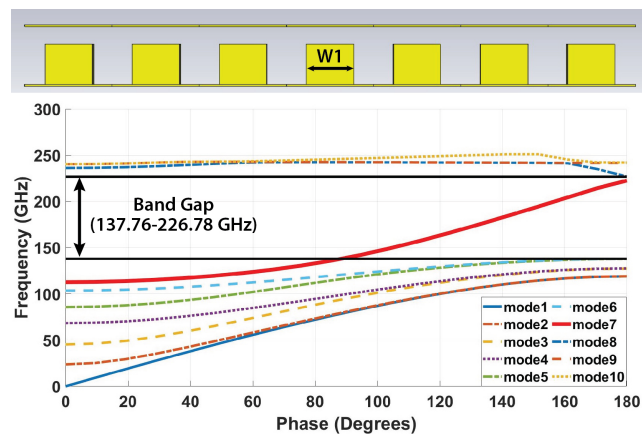
Figure 40. Dispersion diagram of the RGW super cell

The scattering parameters of the RGW structure are shown in Fig. 41 and the surface current distribution for two different frequencies, one in the band and the other out of the band to show the guiding structure of the feeding network as demonstrated in Fig. 42.

45
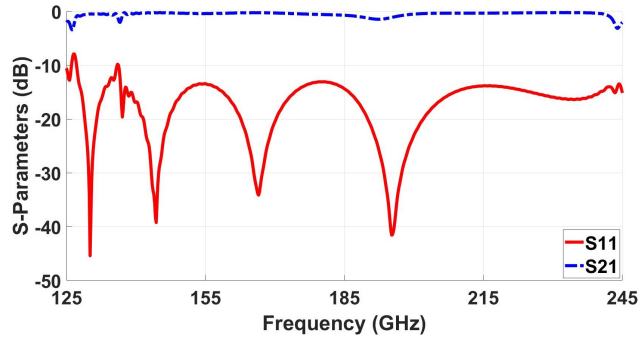
Figure 41. Scattering parameters of proposed RGW

(a)   (b)
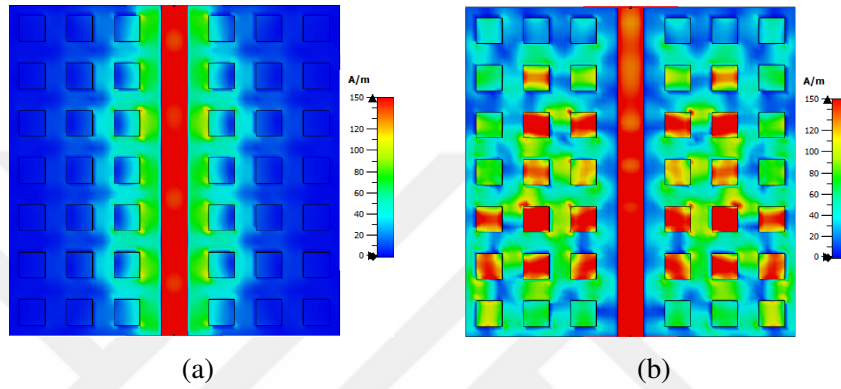
Figure 42. Surface current density at different frequencies (a) 150 GHz (b) 270 GHz

A simple transitional microstrip line structure with a characteristic impedance of 50 Ω can be used to tie the ridge line to an ordinary RF edge SMA connector required for the measurement of the scattering parameters and the antenna's different radiating parameters. To match the transition with the feeding network (ridge), an optimized quarter wavelength transformer is employed at the end of the 50 Ω microstrip line. The microstrip line contacts the upper surface of the ridge and it is implemented on Rogers RT5880 with relative dielectric constant 2.2, thickness 0.15 mm, and loss tangent 0.0009.

To design the reference antenna element of the MIMO structure, a circular radiating slot is etched on the top layer to achieve a wideband response. Figs. 43 and 44 present the proposed RGW antenna where the dimensions of the unit cell and the proposed single antenna element dimensions are listed in Table 5. The optimized circular slot diameter 'D' is 1.6 mm. The RGW single reference antenna size with the transition is 4.9 x 5.6 mm^2. For the sake of fine-tuning the matching of the slot antenna to the RGW

46

feeding network, an optimized rectangular slot is etched on the body of the ridge. The antenna performance in terms of the reflection coefficient with and without microstrip line transition and the comparison between FITD and FEM are shown in Fig. 45 and Fig. 46. The bandwidth of the antenna is between 147.81 – 161.21 GHz which satisfies the RGW boundary conditions inside the stopband. Changing the D-value results in a narrower response and increasing the D-value shifts the resonant frequency response to the lower frequencies. The rectangular sloth width 'S' affects the resonance frequency and bandwidth (BW). The BW is getting narrower and is shifted on lower frequencies with the decrease in S values. The variations of the radiating slot diameter D and S values and the resulting return losses are depicted in Fig. 47 and Fig. 48, respectively.

Table 5. Parameters of the unit cell, supercell, and single RGW antenna

Parameters	Dimensions (mm)	Parameters	Dimensions (mm)
p	0.7	L1	2.8
a	0.38	L2	1.6
h1	0.35	T1	1.443
h2	0.15	T2	0.357
w	0.18	D	0.8
w1	0.38	S	0.3
w2	0.4		
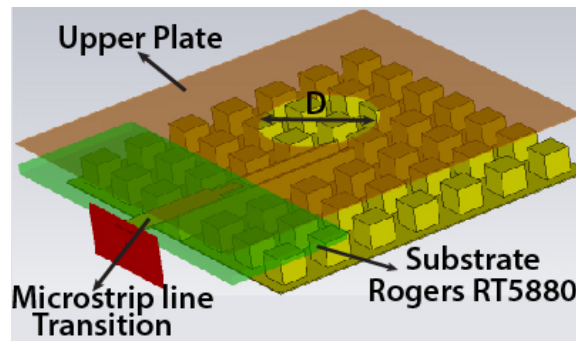
Figure 43. Proposed RGW single antenna with microstrip line transition

6.2 *MIMO antenna design*

A four-port MIMO antenna system is designed by using the optimized single reference RGW fed antenna. Four antenna elements are arranged orthogonally in this construction, and the overall size of the MIMO system is about 9.8 x 9.8 mm^2. As mentioned before, increasing the distance between the radiators is a simple approach to achieving
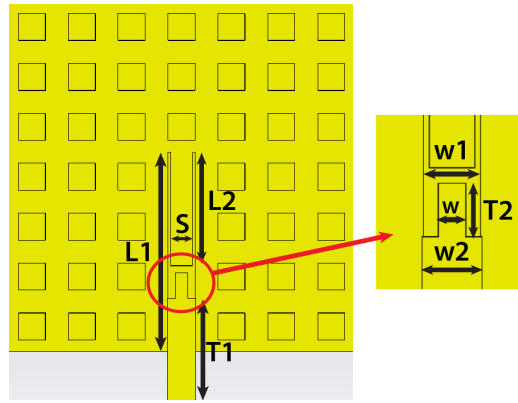
Figure 44. Microstrip-RGW transition
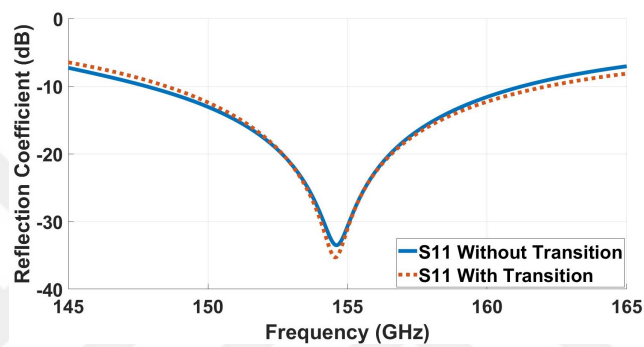
Figure 45. Reflection coefficient for RGW single antenna
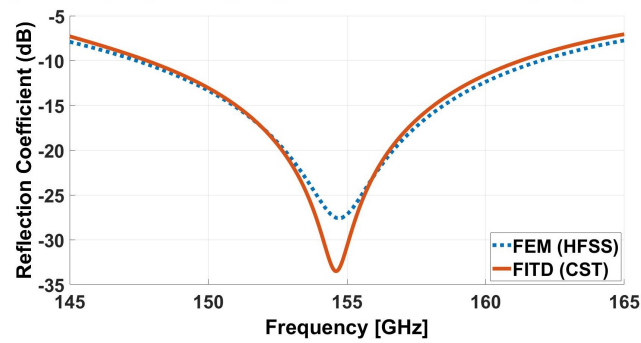
Figure 46. Reflection coefficient for RGW single antenna

great isolation. However, with our main target to develop a smaller size structure, the mutual coupling is expected to increase. For this task, we consider different DGS shapes that are etched on the top ground plane for the sake of achieving optimum antenna performance in addition to the best diversity properties which in turn increase the system capacity and throughput. Three rows are subtracted from the central part of the structure to achieve a compact size of 7.7 x 7.7 mm^2 for all configurations as shown in Fig. 49.

48
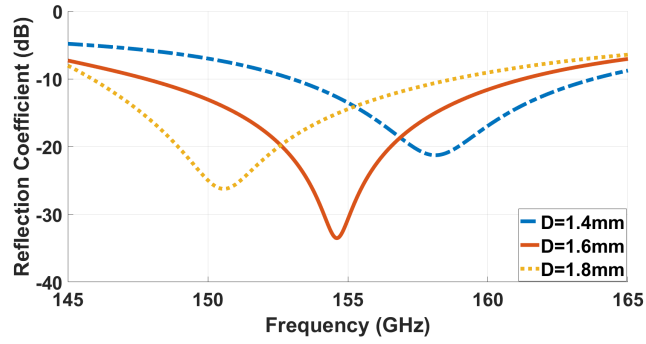
Figure 47. S_{11} values for different D values
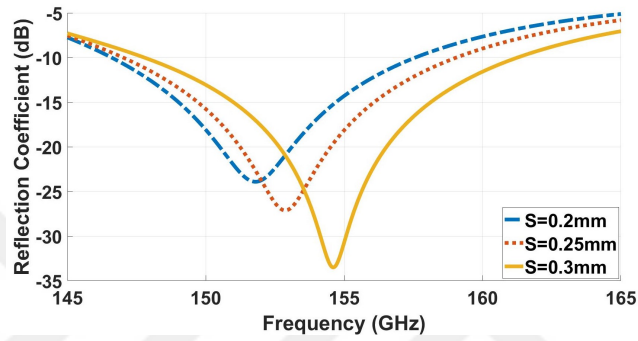
Figure 48. S_{11} values for different S values

Six different compact MIMO antenna configurations are investigated, namely an antenna structure without DGS, and other five MIMO structures with the line, octagon-centered, square-centered, long line, and triangular DGS shapes. The whole DGS MIMO structures are optimized in order to decrease the mutual couplings. The Line DGS shape consists of two orthogonal single lines, the width of the line DGS shape is L4 = 0.2 mm, and the length L3 = 2.4 mm which is approximately proportional to a half wavelength. The design of the octagon-centered and square-centered DGS geometries are implemented such that the octagon and square slots are etched in the center of the line DGS. The line width and length are the same as the line DGS. L6, L7, and L8 values are equal to 0.72 mm, 0.57 mm, and 0.6 mm, respectively. The longline shape is the expanded version of line DGS. The width is kept constant and the length L10 = 2.8 mm. The last DGS shape is triangular which is composed of four triangle shapes etched on the front edge of the line DGS. The dimensions of the triangle are L12 = 2 mm, L13 = 1.7 mm, and the line length is 0.96 mm.
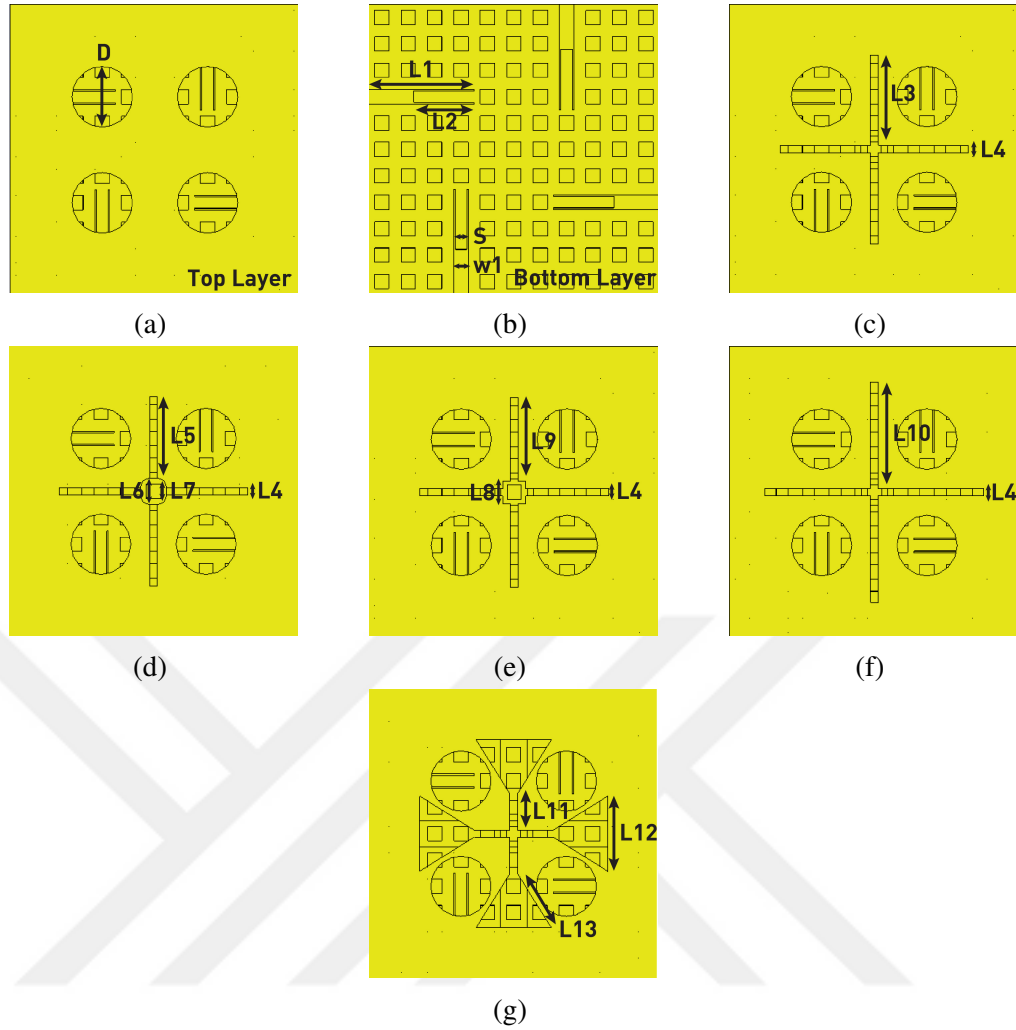
Figure 49. Proposed MIMO antenna geometries: (a) without DGS (b) bottom layer (c) line (d) octagon-centered (e) square-centered (f) long-line (g) triangular

6.3   *Results and Discussion*

6.3.1   *Antenna Simulation Results and Performance Analysis*

Figs. 50 and 51 illustrate the reflection coefficients and gains of the different antenna configurations with and without DGS. The operating frequencies of the proposed MIMO antenna designs are approximately between 148 and 161 GHz. The wide bandwidths are generated from the square and octagon DGS with FBW of 13.8% and 13.67%, respectively. The long-line shape has the lowest return loss of -44.5dB, while the highest one is obtained using the triangular shape whose return loss is -25.2 dB. Concerning the antenna gain, the triangular DGS has the highest realized gain of 7.97 dBi, however, this happens at the expense of lowering the bandwidth by

approximately 2% relative to the other geometries. One of the main targets of this study is to achieve both good diversity parameters in addition to optimum antenna parameters. It is important to point out that, the choice of the antenna parameters or the diversity properties is application-based. Concerning the antenna parameters, the bandwidths and the gains of the proposed designs are listed in Table 6.

Table 6. Proposed MIMO antenna performance

DGS Shape	Op.Freq.(GHz)	FBW (%)	Realized Gain (dBi)	Return Loss (dB)
Square-centered	147.9-161.7	13.8	7.50	-25.8
Octagon-centered	148-161.67	13.67	7.53	-26
Line	148.06-161.7	13.64	7.25	-30.9
Without DGS	148-161.1	13.1	6.95	-35.6
Long-Line	149.32-161.55	12.23	7.31	-44.5
Triangular	150.5-161.6	11.1	7.97	-25.2
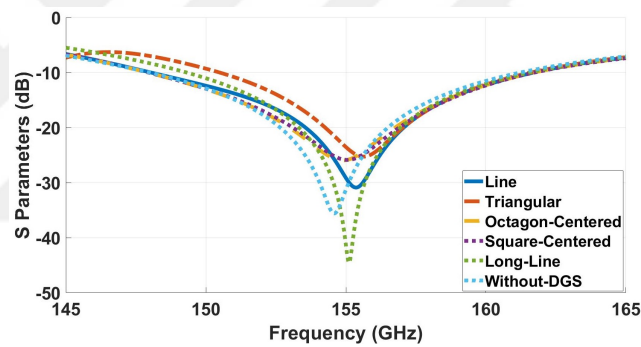
Figure 50. Reflection coefficient of the proposed antennas
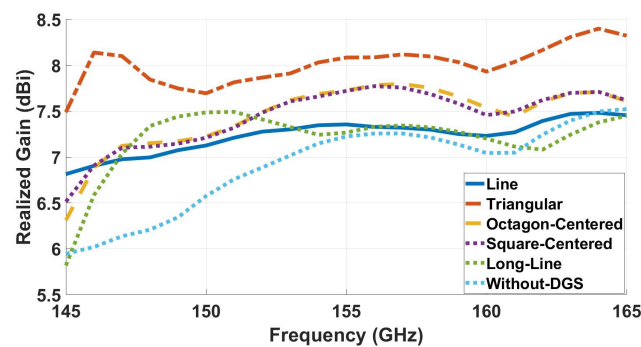
Figure 51. Realized gain of the proposed antennas

One of the most essential characteristics of the MIMO system is the port isolation. As demonstrated in Fig. 52 and Fig. 53, the coupling within the operating frequency is

approximately < -30 dB for all configurations. It is very important to point out that the most stable coupling parameters (S_{21}, S_{31}, and S_{41}) are for the antenna without DGS which varies between -31.9 dB to -38.9 dB. On the other hand, the variation of the coupling for other DGS configurations is steep.
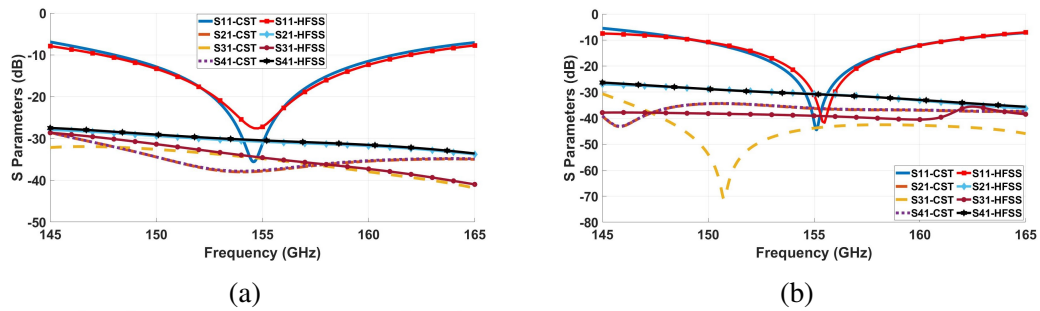
Figure 52. Scattering parameters HFSS verification: (a) without DGS (b) long line DGS

Concerning the other antenna parameters, the configurations of the MIMO antenna structures loaded with DGS of different shapes are achieving either high gain or wide bandwidth keeping the structure performing well for MIMO diversity while giving a wide variation of coupling values of the operating band. This is because each structure is considered as a slot antenna that radiates beside the actual antenna and it will do more coupling in some frequencies and low coupling in other frequencies to the basic antenna elements. In other words, the slot is considered as an aperture antenna that radiates and represents an equivalent current induced on its surface which comes from the basic aperture field fed via the RGW feeding network with low dispersion. Moreover, from an equivalent circuit point of view, the slot is considered an LC circuit giving different resonances for each DGS shape. Different resonances give a shift in the frequency response of S_{11} and the TARC as well. The directivities and the total efficiencies are described in Fig. 54.

The total efficiency values are very similar to each other and are higher than 0.95%. However, at the central frequency of 155 GHz, the directivity varies between that of the triangular structure and the antenna without DGS (8.23-7.34) dBi. One can conclude that the performance of all DGS antennas is getting better than that without DGS and at the same time, the gain is higher. Figure 55 shows the 3D radiation pattern of the MIMO antennas.
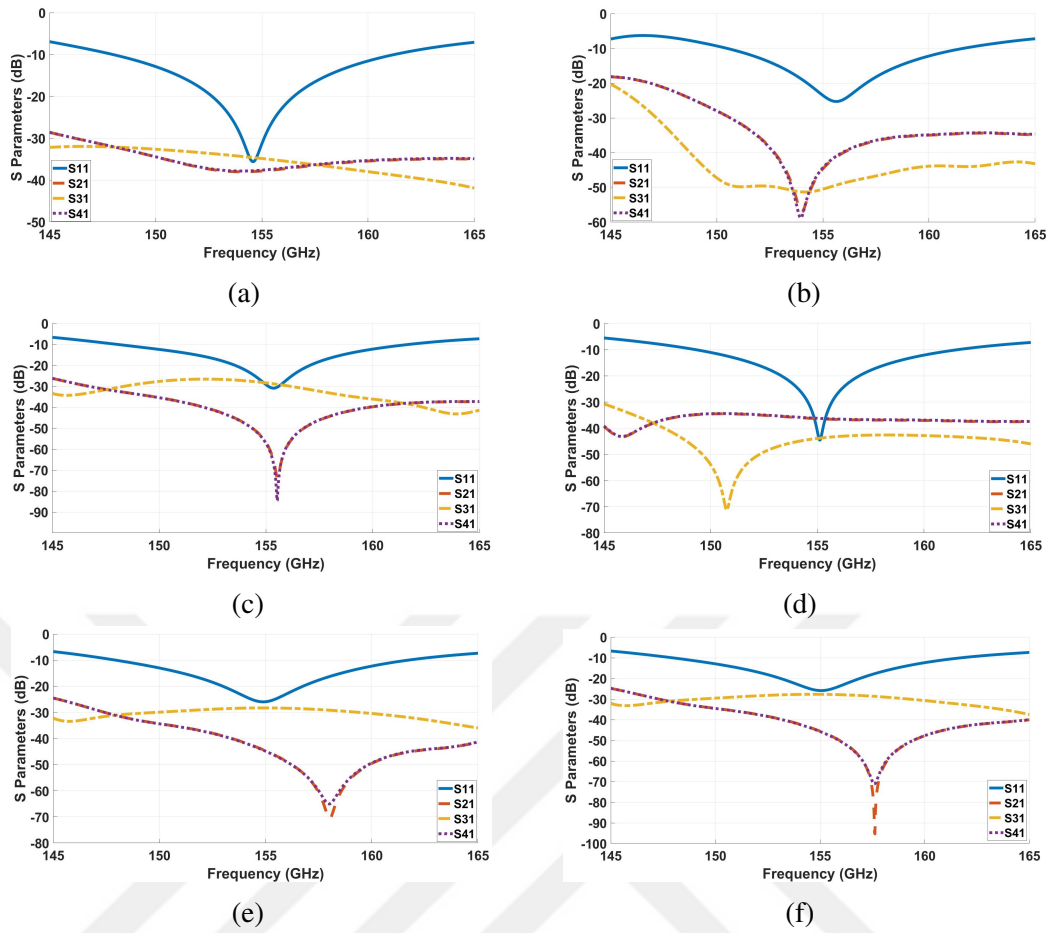
Figure 53. Scattering parameters of the proposed antennas: (a) without DGS (b) triangular (c) line (d) long line (e) octagon-centered (f) square-centered

6.3.2 *MIMO Diversity Performance*

In this part, we look at the key factors that influence the antenna performance in MIMO systems. The ECC, DG, ME, CCL, and TARC characteristics are used to verify the MIMO's performance.

Fig. 56 shows the ECC results with the use of the radiation pattern formula, it is important to note that this approach gives more accurate results compared to the formula based on scattering parameters. The obtained ECC values of all MIMO configurations are less than 0.0006 for their operating frequency band. These results prove that the proposed designs are uncorrelated. The simulated DG graphs are illustrated in Fig. 57. It is important to point out that all antenna configurations are performing well in term of ECC and DG. From the DG's point of view, all DG values are higher than 9.997 dB. The Line, octagon-centered, and squared-centered DGS
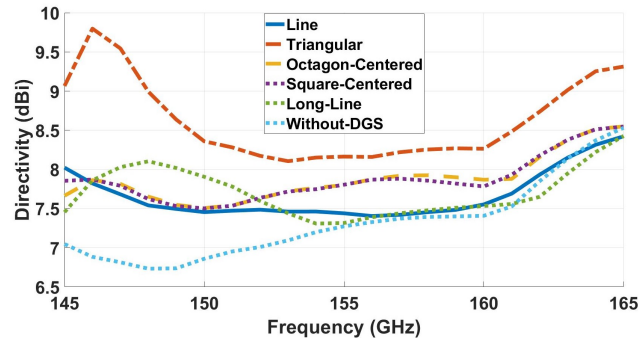
(a)
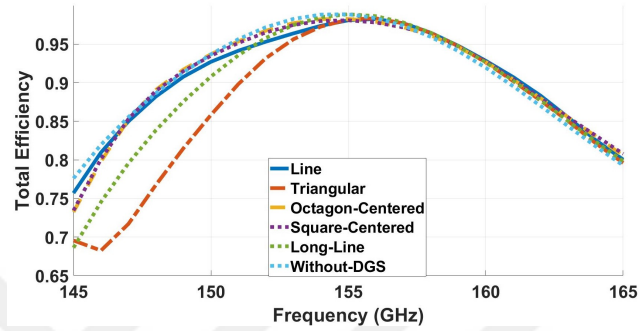
(b)

Figure 54. Proposed antennas (a) directivities (b) total efficiencies

show weak performance compared to the others. In conclusion, the best performance is provided by the triangular DGS which with DG value of almost 10 dB. The ECC and DG values for ports (1,4) and ports (2,4) are not considered because they are symmetric to those of ports (1,2) and ports (1,3).

The simulated ME values are shown in Fig. 58 for different DGS shapes. The ME values are very close to each other for the different proposed designs. The ME value is above -1 dB for the operating frequency range for all antennas. However, the antenna with long-line DGS and those without DGS are contributing with low ME values at 0.05 dB, whereas, the highest ME value is exhibited by the antenna with square-centered DGS at 0.084 dB.

The simulated CCL values are shown in Fig. 59. The obtained CCL values are less than the stated minimum limit for all antennas. The maximum CCL value is 0.025 bit/s/Hz and the minimum obtained CCL value is 0.003 bit/s/Hz for the square-centered and the long-line shapes, respectively at a resonance frequency of 155 GHz.

The obtained results of the TARC metric are shown in Fig. 60 for two cases, the first

Table 7. Comparisons between the proposed MIMO antenna system and other published studies.

Ref.	Band(GHz) or f_c(FBW)	N	Mutual Coup. (dB)	ECC	DG	CCL	ME	TARC
Ahmad et al. (2022)	29 (3.7%)	4	-36(min)	0.0001	>9.8	NA	~ -2.3	NA
Ibrahim and Ali (2022)	2.7-11	4	<-20	<0.0004	>9,96	<0.4	-8(min)	NA
Sharma et al. (2020)	23-29	4	<-28	<0.01	>9.95	NA	NA	<-5
Khalid et al. (2020)	28 (4.1%)	4	<-17	<0.01	>9.96	<0.4	NA	NA
Ojaroudi Parchin et al. (2019)	3.3–3.9	8	<-17	<0.01	NA	NA	NA	-30(min)
Jetti and Nandanavanam (2018)	3.1–11.8	2	<-20	<0.03	NA	NA	NA	NA
Okan (2021)	95-205	2	<-17	<0.006	>9.97	<0.4	NA	NA
Square-cent.	147.9-161.7	4	-27,1(max)-96(min)	<0.0002	>9.999	<0.4	>-1	-19.4
Octagon-cent.	148-161.67	4	-28(max)-71.3(min)	<0.0002	>9.999	<0.4	>-1	-18.9
Line	148.06-161.7	4	-26.4(max)-84.6(min)	<0.0006	>9.997	<0.4	>-1	-23.4
Long-Line	149.32-161.55	4	-34.2(max)-71.6(min)	<0.0003	>9.998	<0.4	>-1	-23
Triangular	150.5-161.6	4	-29.6(max)-59.1(min)	<0.0006	>9.997	<0.4	>-1	-15
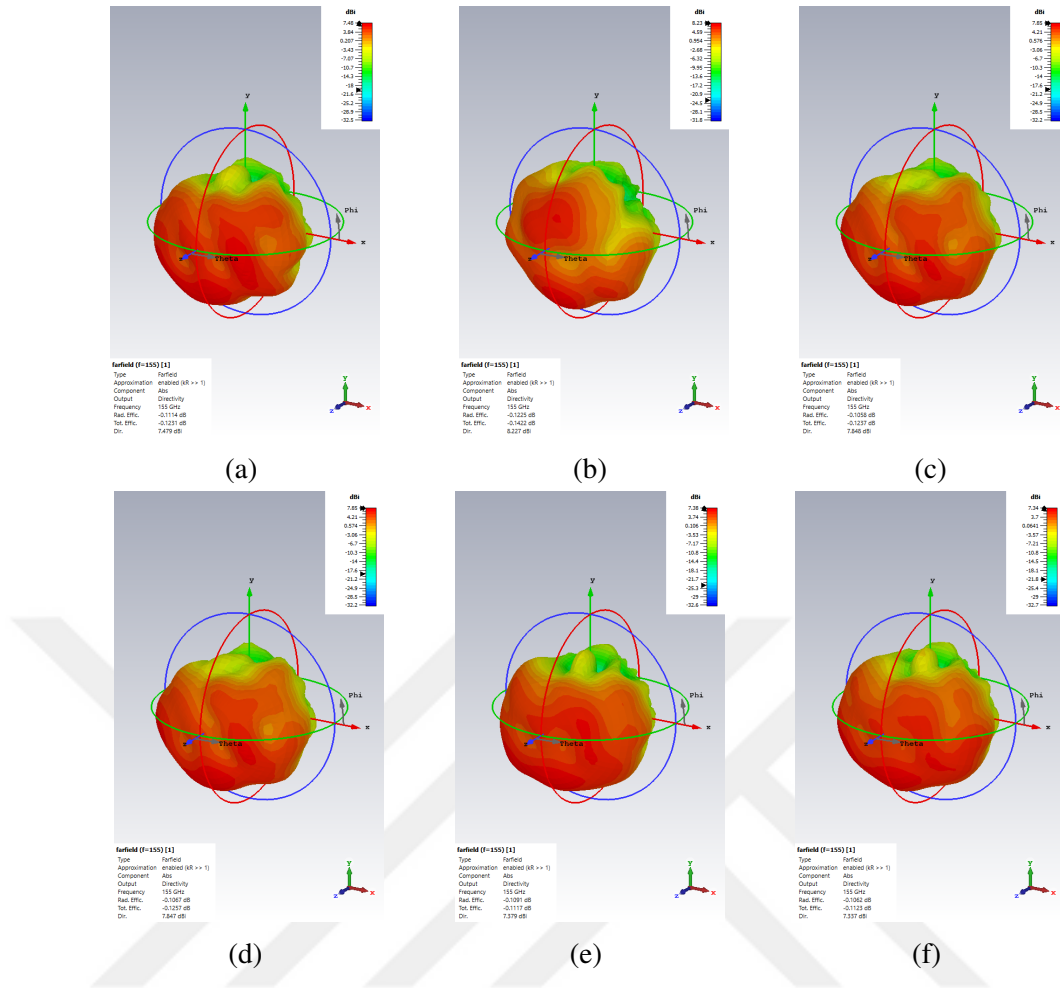
Figure 55. 3D Radiation patterns of the proposed antennas:a) line b) triangular c) octagon-centered d) square-centered f) long-line g) without DGS

case considers different random phases of the incoming signal Fig. 60 (a), (b) and the second one considers fixed phase angle of the incoming signal to each antenna element Fig. 60 (c), (d) it is apparently noticed that there is a decrease in the BW of most of the antennas by about 5% for both cases. Most of the structures exhibit a center frequency shift to the right when the θ values are increased in all antenna configurations. Triangular DGS is the least affected structure by the changes in θ.

Table 7 compares the performance of the five different configurations of this study to previously published works. Our results show more optimized values in terms of the diversity parameters DG close to 10 dB and a TARC value of about -23.4. The obtained mutual coupling values show very low levels compared to other studies, the maximum coupling level is -26.4 dB and the minimum reached level is -96 dB. It is important to note that we consider both fixed and random phase angles in the computations of the
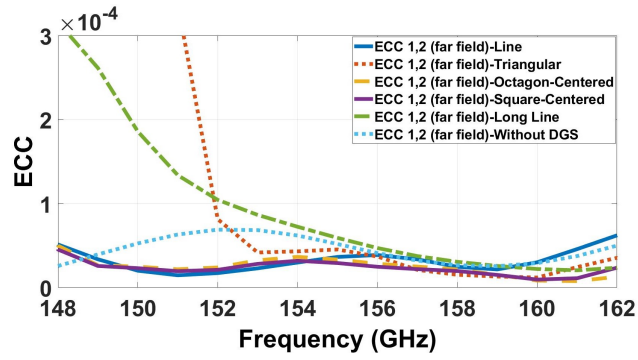
(a)
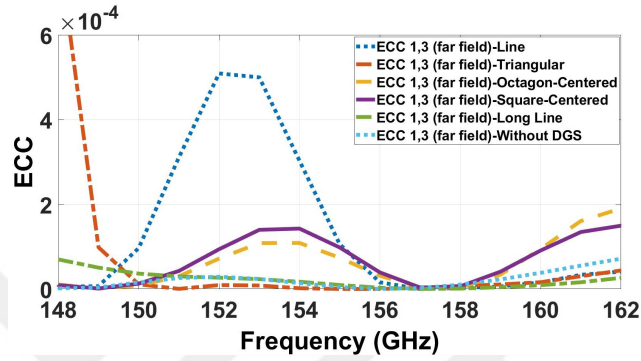
(b)

Figure 56. The ECC performance of the proposed four-element MIMO antenna. (a) between ports 1 and 2. (b) between ports 1 and 3

TARC parameter relative to other studies. Considering the MIMO antenna with the long-line DGS design, a comparison with the existing similar systems in the literature shows that our design provides maximum mutual coupling values of about -34.23 dB, while the maximum reported values are approximately below -17 dB (Ibrahim and Ali, 2022; Sharma et al., 2020; Khalid et al., 2020; Ojaroudi Parchin et al., 2019; Jetti and Nandanavanam, 2018; Okan, 2021). Our design is not only satisfying the ECC requirement but also shows values closer to zero (ECC < 0.0003) compared to the values reported in the literature (Ibrahim and Ali, 2022; Sharma et al., 2020; Khalid et al., 2020; Ojaroudi Parchin et al., 2019; Jetti and Nandanavanam, 2018; Okan, 2021). The obtained DG value of the proposed design is converging to the ideal value of 10 dB. Even though most of the previous studies in the literature did not provide the ME value, our result is found to be the best among the reported values (Ahmad et al., 2022; Ibrahim and Ali, 2022). It is important to note here that, random phase angles θ should be included in the computations of the TARC values, but this is not considered in most reported studies. In a study conducted by Ojaroudi Parchin et al. (2019), in the calculation of the TARC value, they did not consider random phase angles and
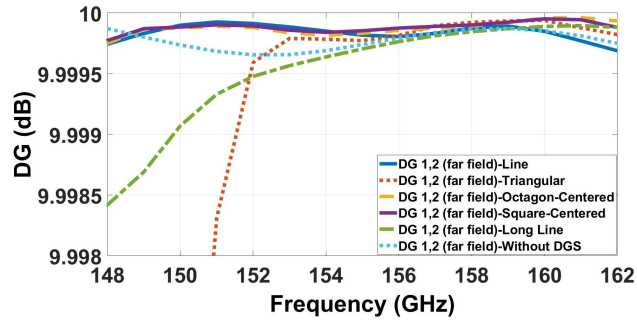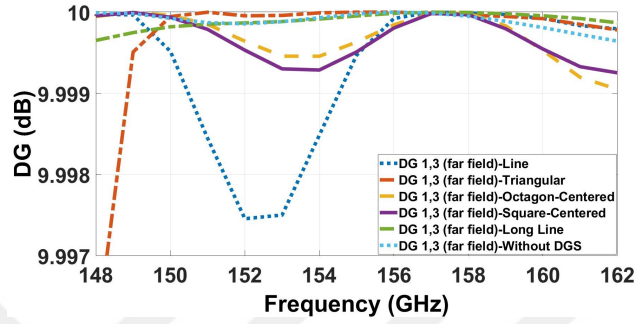
Figure 57. The DG performance of the proposed four-element MIMO antenna. (a) between ports 1 and 2. (b) between ports 1 and 3.

obtained a value of about -30 dB. The obtained TARC value for the current design is about -23 dB which is the best among other reported values (Sharma et al., 2020).

6.4   *Conclusion of DGS MIMO Antenna*

Compact four-port RGW MIMO antennas are proposed for D-band applications. The designs consider various DGS shapes in addition to a design without DGS. A 38.27% compactness in size is achieved by eliminating 3 rows of pins in the center of the MIMO structure. Five different DGS shapes, namely, line, octagon-centered, square-centered, long line, and triangular shapes are etched to minimize the coupling effect. The total size of the proposed MIMO antenna structure is 7.7x7.7 mm^2. The MIMO structure without DGS shows coupling levels between -31.9 dB to -38.9 dB, while the minimum coupling (-96 db) was reached by using the square-centered DGS. The most stationary coupling is exhibited by the antenna without DGS while the variation of coupling for other DGS configurations is abruptly changed. Square-centered DGS shows the most unstable coupling values S_{31}, S_{41}, and S_{21} which are -27.1dB, -71 dB, and, -96 dB, respectively. On the other hand, the triangular DGS has the highest realized gain of 7.97 dBi, however, this happens at the expense of lowering
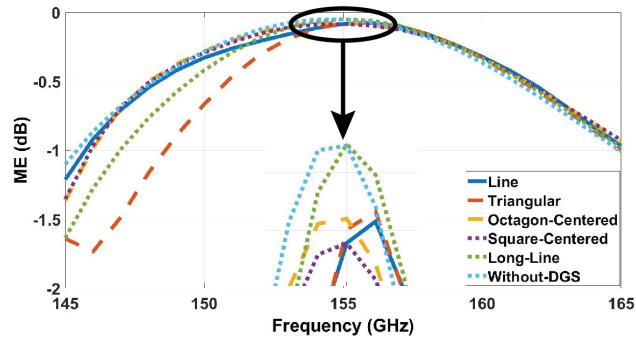
Figure 58. ME of the proposed antennas
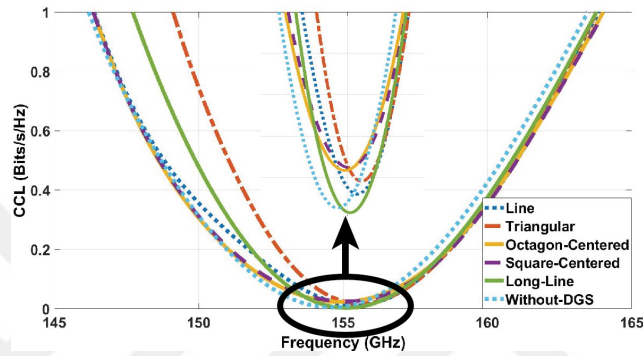
Figure 59. CCL of the proposed antennas

the bandwidth by approximately 2% relative to the other shapes. The choice of the antenna parameters or the diversity properties is application-wise. The simulation results for diversity properties ECC < 0.0006 and DG > 9.997dB, CCL < 0.4 bit/s/Hz, and η_{mux}>-1 dB show excellent performance within the operating band. The TARC metric is investigated for random incident signal phase angles. The TARC bandwidth (< -10 dB) is approximately 5% narrower compared to the S11 because of the sharp variations of the coupling parameters. In terms of antenna parameters and MIMO diversity parameters, the DGS antennas show better performance compared to the structure without DGS.
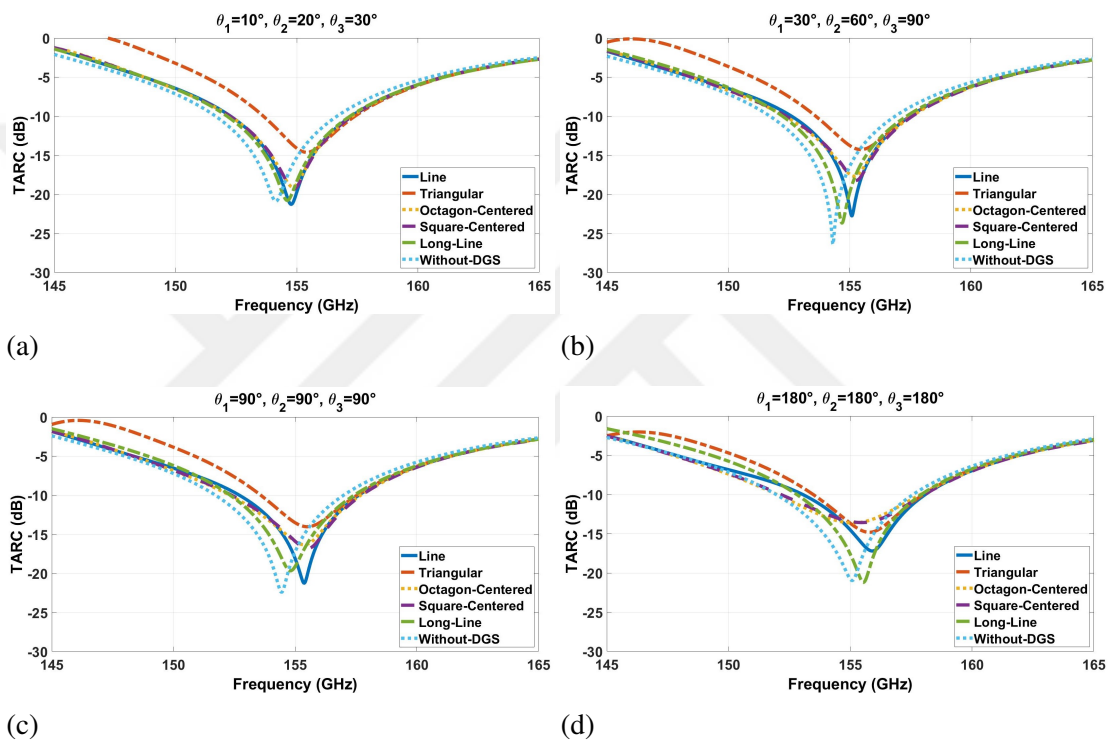
Figure 60. Simulated TARC values for different values of θ_1, θ_2, and θ_3 : (a,b) random phase angle (c,d) fixed phase angle

CHAPTER 7 : A NOVEL CIRCULAR RECONFIGURABLE METASURFACE-BASED COMPACT UWB HYBRID COUPLER FOR KU-BAND APPLICATIONS

A novel circular reconfigurable metasurface (MS) based compact ultra-wideband (UWB) hybrid coupler is developed for Ku-band applications. The coupler is developed using the substrate-integrated gap waveguide (SIGW) technology. The coupler structure consists of two layers, the bottom layer represents the artificial magnetic surface of the periodic structures, and the ridges in between that guide the wave in the required direction with minimum dispersion. It involves the coupling section with a centered etched slot and two additional vias to achieve the basic hybrid coupler properties. This layer is nominated as the ridge layer. The second layer is a circular shape of a dielectric gap loaded with the top ground. The top ground is left solid for a non-reconfigurable coupler. Concerning the reconfigurable coupler, this layer contains an artificial metasurface of Jerusalem cross elements where the copper is etched around. This layer is nominated as the gap layer. This MS surface is mechanically rotated to offset the magnitude and phase of the signal going to the through and coupled ports. The findings obtained from the simulations show that the reconfiguration can be accomplished by rotating the MS around the source coupler's central axis. The rotation is tested between 0° to 180° in the counter-clockwise direction. The operating frequency range of the coupler is between 11.94 to 16.91 GHz, which covers approximately the whole Ku-band. The coupler delivers continuously adjustable amplitude between 2.6 and 4.8 dB while the phase differences within 77° to 105° over a fractional bandwidth (FBW) of 34.45%. It is manufactured using PCB technology and measured using a network analyzer. A strong agreement is achieved between simulations and measurements. The proposed coupler can be used in traditional beam-forming and beam-steering networks by changing the rotation angle or the operating frequency. The developed coupler can replace the Butler and Bless matrices with their complication, heavy number of phase shifters, and crossover problems. The current work can be extended to operate in the mm-Wave band by changing the dimension and the material of the unit cell of the ridge layer of the coupler. The development process of the proposed work is summarized as follows:

- SIGW coupler design and fabrication

- Results and discussion

- Conclusion of the reconfigurable coupler

7.1   *SIGW Coupler Design and Fabrication*

7.1.1   *SIGW Design*

Based on SIGW technology, the unit cell of the current design is composed of two parallel layers positioned as a bottom Rogers RO4350B (ε_r=3.66) and a top Rogers RO4003C (ε_r =3.55) substrates. In the bottom layer, the ground and the conductor mushroom patches are connected by vias. The directing ridge is positioned in the middle of the unit cells to activate the desired propagating quasi-TEM mode. Fig. 61 depicts the simulated dispersion diagram of the unit cell and supercell. The dispersion diagram of the unit cell covers the frequency range from 8.1 to 22.4 GHz as simulated by the CST Eigen Mode Solver. The frequency range of the supercell design is 8.6 to 22.1 GHz, and it is obvious that the ridge lowers the stopband by approximately 5.6%. Fig. 62 demonstrates the feeding network of the proposed SIGW and the surface current distribution for two distinct frequencies, one is in the band and the other is out of the band. At 15 GHz, it is evident that the wave is constrained while leaking occurs at 5 GHz which is out of the band. Table 8 shows all the dimensions of the unit cell and supercell structures. It is determined that 1.6 mm is the optimal ridge width value. In essence, by adapting the strip line impedance equation, the characteristic impedance of the ridge can be determined. A small deviation from the results is predicted because the structure consists of two different substrates with close ε_r values.

Table 8. Dimensions of the unit cell and supercell

Parameters	p	r1	r2	a	h1	h2	w
Values (mm)	18.2	0.4	1.6	2.6	1.524	0.203	1.6

For the measurement of the scattering parameters of the coupler, a standard RF edge SMA connector should be connected to the ridge which is difficult to be implemented. A transition shown in Fig. 63 is designed for this purpose. A microstrip line of the characteristic impedance of 50 Ω connects the ridge line to the SMA connector. The microstrip line is implemented on the top layer with a thickness of 0.45 mm and it contacts the upper surface of the ridge as shown in Fig. 63. Table 9 shows the microstrip transition dimensions.
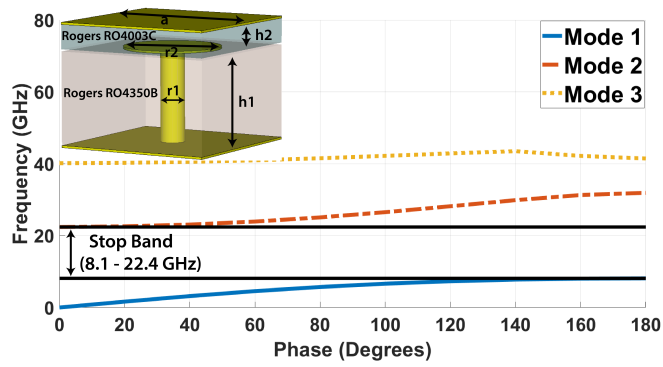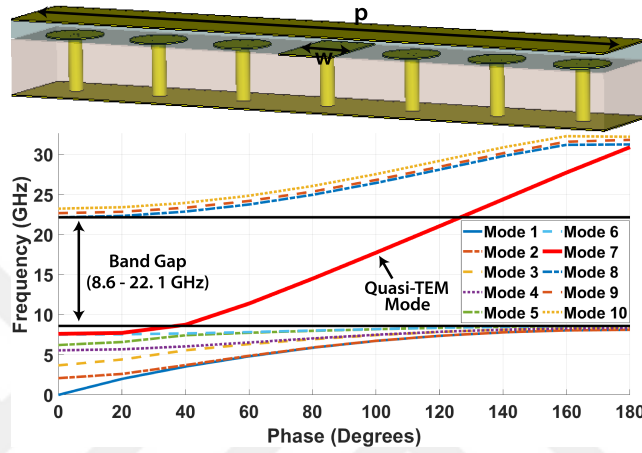
Figure 61. Dispersion diagram of a) unit cell b) supercell
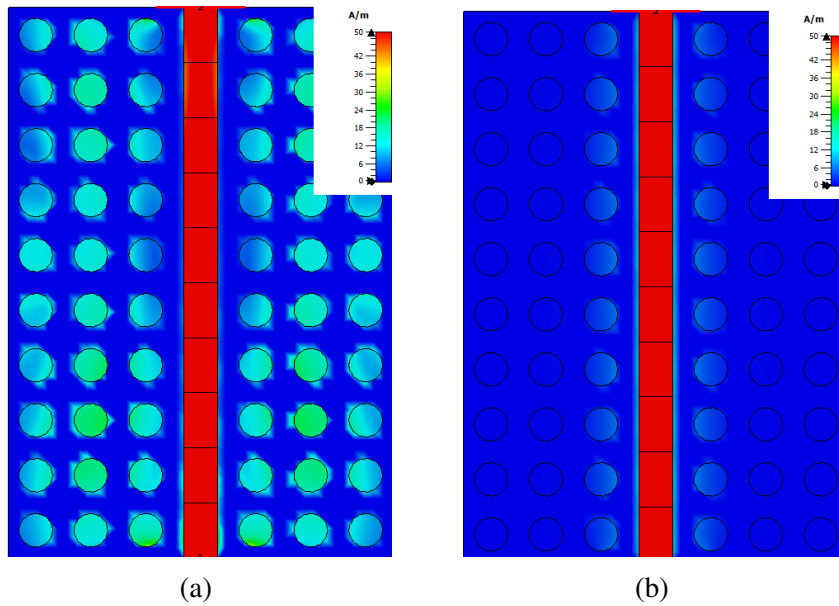
Figure 62. SIGW feeding network surface current distribution at (a) 5 GHz (b) 15 GHz
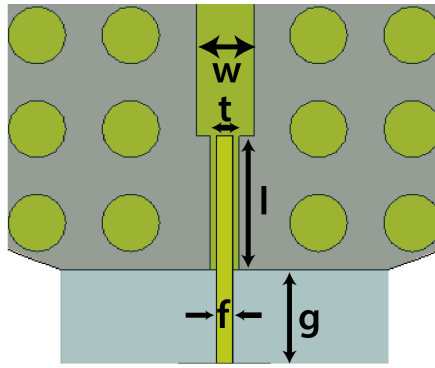
Figure 63. SIGW microstrip line transition

Table 9. Dimensions of the microstrip-SIGW transition

Parameters	t	l	f	g
Values (mm)	0.8	3.7	0.45	2.6
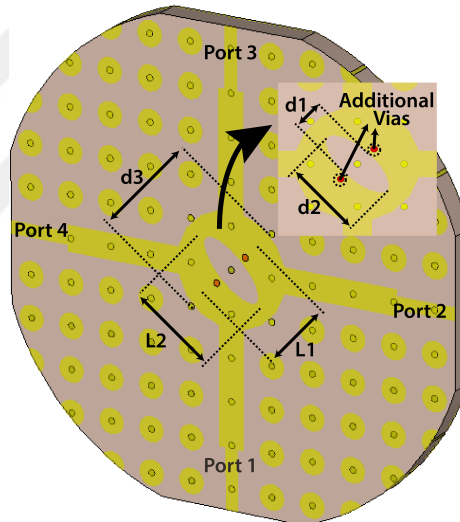
Figure 64. Bottom (Ridge) layer of the proposed coupler

Table 10. Dimensions of the new mm-Wave unit cell

Parameters	b	r3	r4	h3	h4
Values (mm)	2.5	0.4	1	0.504	0.203

The bottom layer of the coupler is illustrated in Fig. 64, it contains four reciprocally coupled PRGW lines. The coupling section is a circular junction patch with a 45° elliptical slot in the center of those lines. In addition, two more vias are added at an orthogonal angle to the slot axis. This slot and vias are intended for achieving a better power distribution in a 3 dB hybrid coupler. This coupler's design is comparable to a
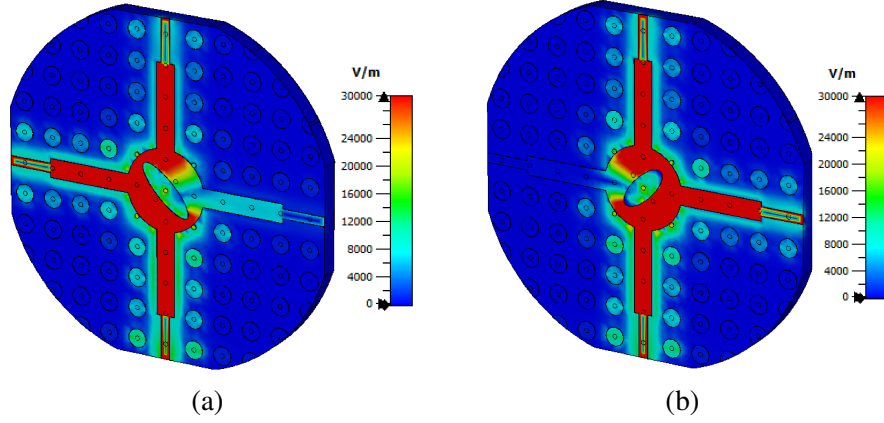
Figure 65. E-field distribution at 13.5 GHz. a) slot is left inclined b) slot is right inclined

(a)

(b)
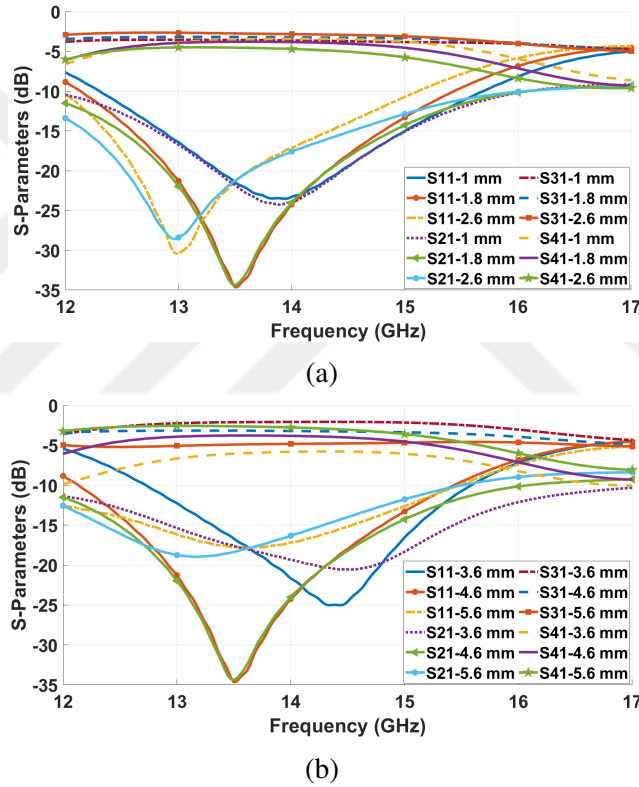
Figure 66. Simulated scattering parameters a) d1 variation b) d2 variation

typical microstrip or a bulky wave coupler. According to the basic design concept (Shen et al., 2018) of the hybrid coupler, if two parallel lines have characteristic impedances of Z_0, the other two parallel lines should have impedances of $Z_0/\sqrt{2}$. The lengths L1 and L2 are not precisely identical to the $\lambda_g/4$ value, two correction factors are provided for designing the SIGW coupler effectively as given by Eqs. (1, 2).

$$L1 = (1+b)*(\lambda_g/4). \tag{1}$$
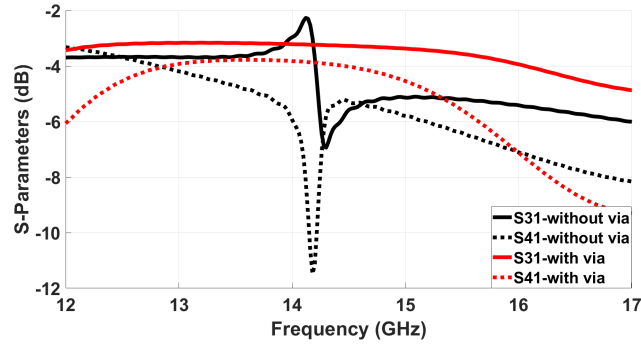
Figure 67. Effects of additional vias on the scattering parameters of the proposed coupler
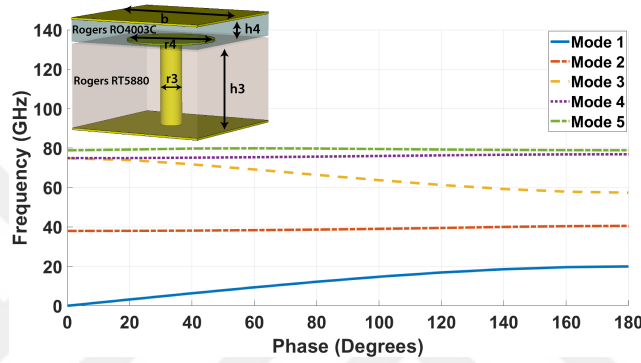
Figure 68. Dispersion diagram of the mm-Wave unit cell

$$L2 = (1+c)*(\lambda_g/4). \tag{2}$$

where b and c represent two additional correction factors. The starting values of b and c can be set to zero, but the final values must be tuned depending on the optimal passband and the isolation performance. The optimum values for L1 and L2 are 3.1 mm and 5.8 mm, respectively. The elliptical slot's location specifies the isolation port to be used. The isolation is port 2 if the slot is slanted to the left; if it is inclined to the right, the isolation is port 4. Fig. 65 demonstrates the electric field distribution in terms of elliptical slot placement. In order to improve the power distribution, two vias were also placed at the bottom of the circular patch. The optimized dimensions of the elliptical slot are $d1 = 1.8$ mm and $d2 = 4.6$ mm and the diameter of the circular patch $d3 = 7$ mm. The scattering parameter variations with the elliptical slot dimensions d1 and d2 are depicted in Fig. 66. It can be seen that the center frequency shifts depending on the size of the slot. The optimized values of d1 and d2 are obtained by changing one parameter while keeping the second one constant and vice versa. If d1 and d2 decrease, the center frequency shifts to higher frequencies. If d1 values

increase, the shifting occurs at lower frequencies. An increase in the d2 does not affect the center frequency. The effects of additional vias in terms of power division are shown in Fig. 67. It is evident that huge losses occur between 14 GHz and 15 GHz without vias. Adding two extra vias helps in the equal power division. It is important to point out that this structure can be easily extended to operate in the mm-Wave band for 5G/6G applications. This can be achieved by the precise design of the unit cell of the ridge layer of the coupler as depicted in Fig. 68. This dispersion diagram shows that the AMC vias can generate a bandstop to accommodate a quasi-TEM mode over two subbands of mm-Wave applications with a BW of more than 18 GHz. The material layer is changed to Rogers RT5880 and the dimension is changed according to the values in Table 10. It is considered for the future work of the current structure.

7.1.2 *Metasurface design*

Fig. 69 demonstrates the Jerusalem cross-unit cell and the MS design. The finite size MS is investigated in order to determine its effective permittivity (ε_r), permeability (μ_r), reflection, transmission and absorption performances. The plane wave analysis is performed by the CST simulator. The basic formulas for the MS's equivalent impedance Z, the refractive index n, μ_r, and ε_r can be written as (Szabo et al., 2010):

$$Z = \pm\sqrt{\frac{(1+S_{11})^2 - S_{21}^2}{(1-S_{11})^2 - S_{21}^2}} \tag{3}$$

$$X = 1/[2S_{21}(1/S_{11}^2 + S_{21}^2)] \tag{4}$$

$$e^{jnk_0d} = X \pm j\sqrt{1-X^2} \tag{5}$$

where k_0, and d are the wave number and MS equivalent thickness, respectively.

$$\varepsilon_r = Re\{n/Z\} \quad \text{and} \quad \mu_r = Re\{nZ\}. \tag{6}$$

The scattering parameters and the normalized absorption rates are shown in Fig. 70. One can see that the MS behaves as a reflector over the whole operating frequency range except between 16 and 17 GHz, it is an absorber. In the frequency range from 16.4 to 16.7 GHz, the MS is a left-hand metasurface with a negative index of refraction n, negative μ_r, and negative ε_r values. It is a right-hand gap absorber from 16.7 up to
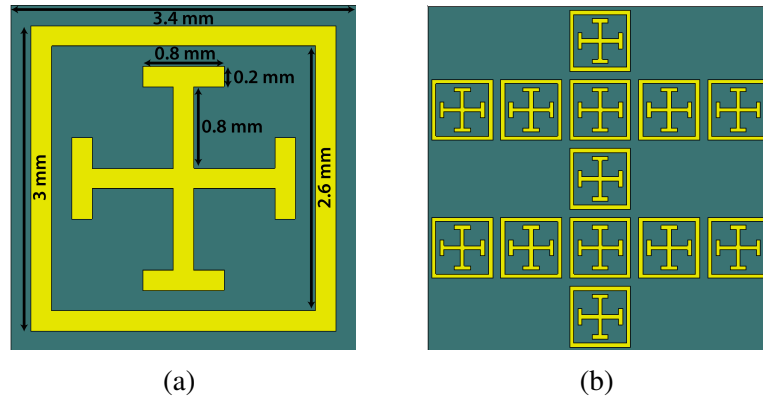
Figure 69. Proposed MS design a) Unit cell b) Metasurface
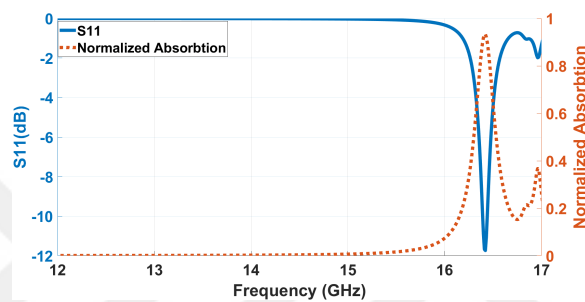
Figure 70. Simulated reflection coefficients and normalized absorption rates

17 GHz as shown in Fig. 71.
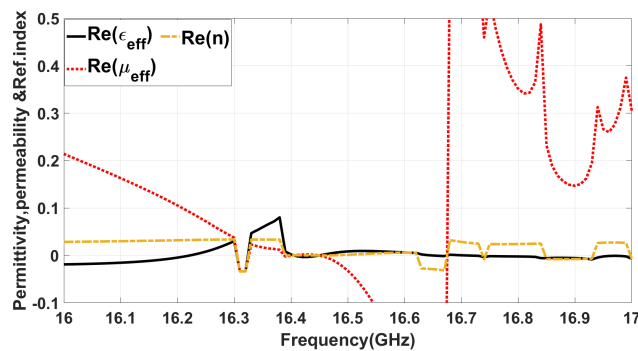
Figure 71. Calculated real part of relative permittivity, permeability and refractive index of the metasurface

The proposed reconfigurable coupler design is based on Jerusalem cross MS as depicted in Fig. 72. The top layer of the SIGW is circularly cut for the MS to be mechanically adjusted and rotated. The diameter of the rotating surface is 20 mm.

68
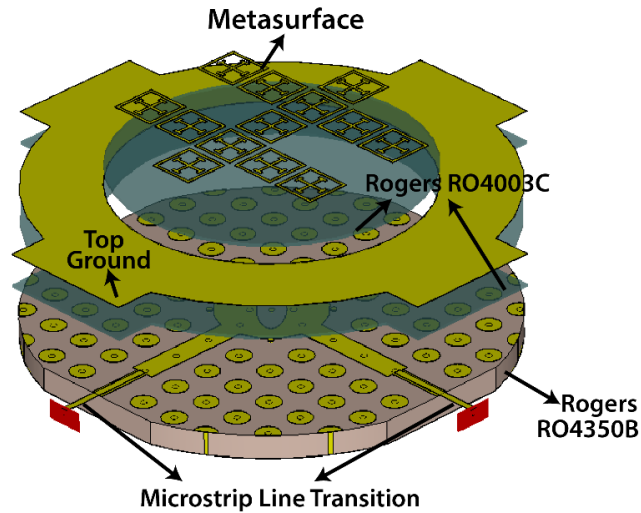
Figure 72. Proposed MS-based reconfigurable coupler

7.1.3 *Fabricated Coupler*

This section is devoted to the fabrication of the proposed coupler using PCB technology. Concerning the coupler structure, it is divided into two main layers. The gap layer includes the dielectric gap and top ground. The ridge layer comprises the vias, the ridge, and the feeding network including the transition as depicted in Fig. 73. For the sake of reconfiguration, the top ground of the gap layer includes a separate interior circular section of the MS structure which can be rotated for different angles as shown in Fig. 74. Fig. 75 illustrates the measurement setup for measuring the scattering parameters of both couplers using network analyzer ROHDE & SCHWARZ ZVB20.

7.2 *Results and Discussion*

Concerning the non-reconfigurable coupler, Fig. 76 depicts the simulated and measured scattering parameters of the proposed design. One notices that it operates 12.14 to 15.4 GHz under -10 dB level. Also, the coupling coefficients at port 3 and port 4 are nearly 3 dB with isolation at port 2. Fig. 77 shows the phases of the scattering parameters at ports 3 and 4. One can infer that the phase difference between them is nearly 90°. It is clear that the proposed coupler is a SIGW-based technology that achieves the hybrid parameters performance of the conventional couplers. The strong agreement between the measured results and the simulated ones validates all the new findings of the study.
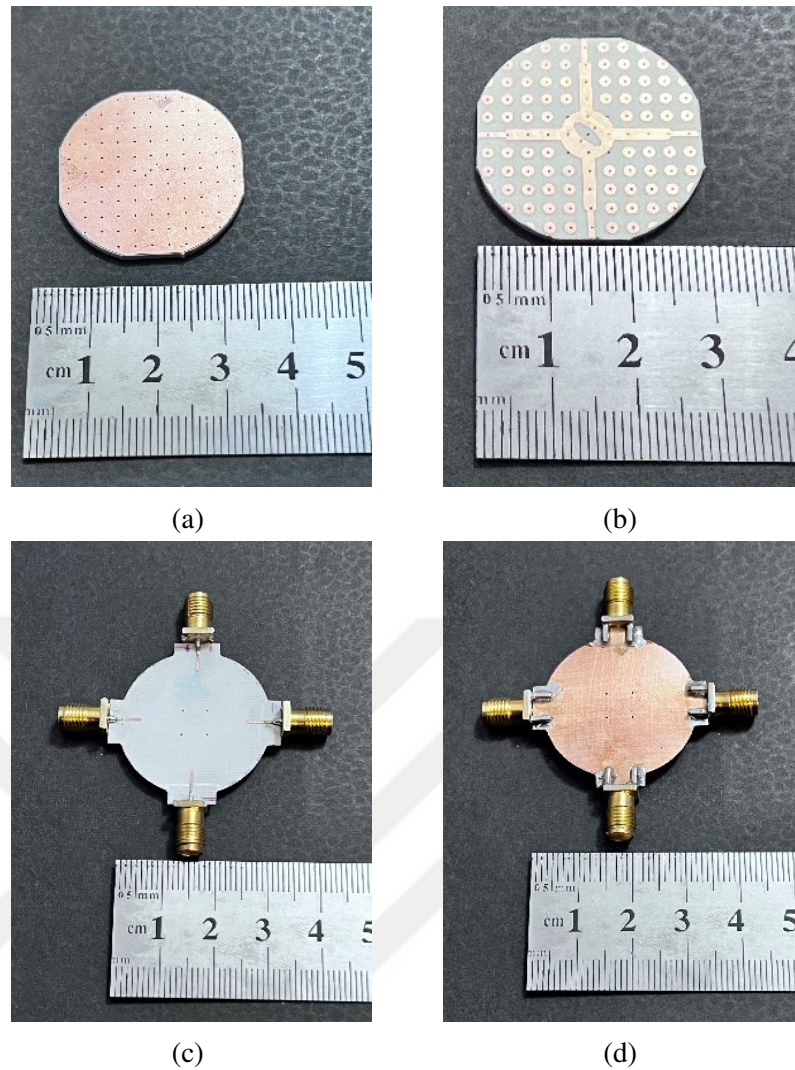
Figure 73. Fabricated coupler (without MS) a) bottom view of ridge layer b) top view of ridge layer c) bottom view of the gap layer d) top view of the gap layer

Concerning the proposed reconfigurable coupler, the top MS layer is mechanically rotating in counter-clockwise directions to achieve different scattering parameters at ports 3 and 4. As shown in Fig. 78 the reflection coefficient values vary with rotation keeping a persistent common frequency band. The widest bandwidth (UBW) occurs between 11.94 GHz to 16.91 GHz at 150° while the narrowest one is between 13.07 GHz to 16.34 GHz at 30°. The common BW among the different angles of incidence is approximately 4.2 GHz. The return loss is almost below -20 dB for all rotation angles. The isolation is greater than 15 dB for all cases. As can be observed, the two-output amplitude responses are slightly changing according to the rotation angle. The output power remains steady between 2.6 dB and 4.8 dB range in the middle as shown in

(a)   (b)

(c)   (d)
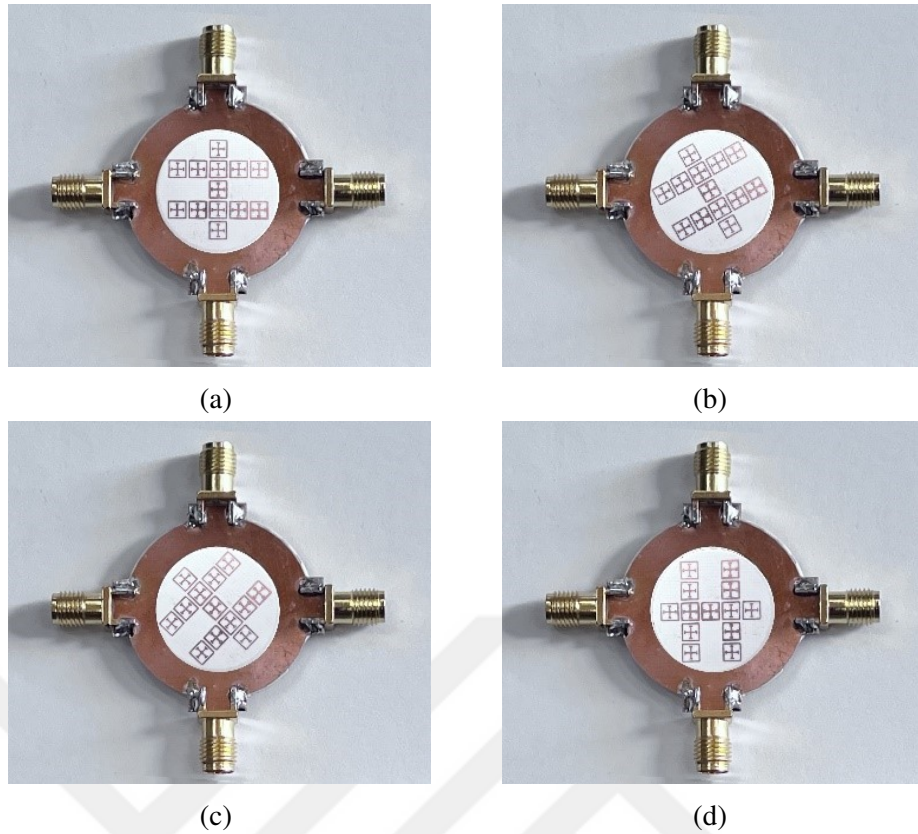
Figure 74. The fabricated reconfigurable coupler (with MS) at different rotated angles
a) 0° b) 30° c) 45° d) 90°

(a)   (b)
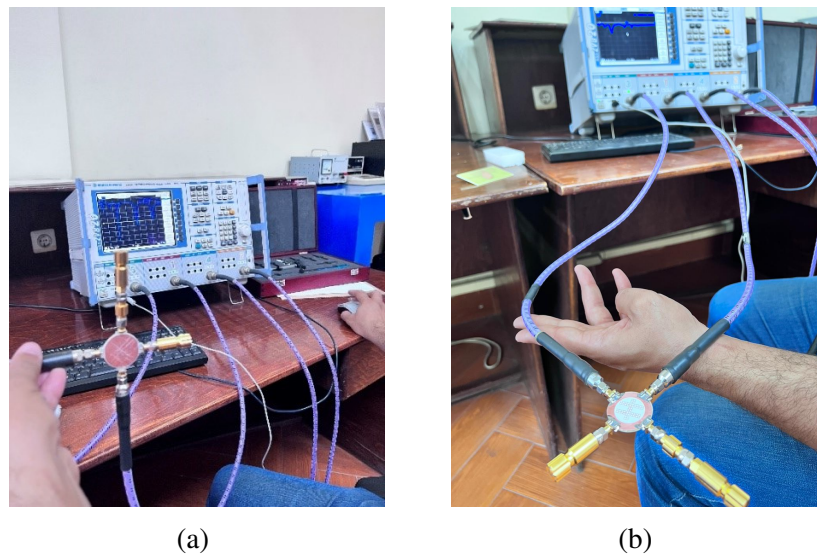
Figure 75. The measurement setup of the proposed couplers using ROHDE &
SCHWARZ ZVB20 vector network analyzer a) without reconfiguration b) for a
reconfigurable coupler

Fig 79. However, the power fluctuates in port 4 at 8 dB at the corner of the operating

frequency. As demonstrated in Fig. 80, one can notice that the phase variation at ports

71
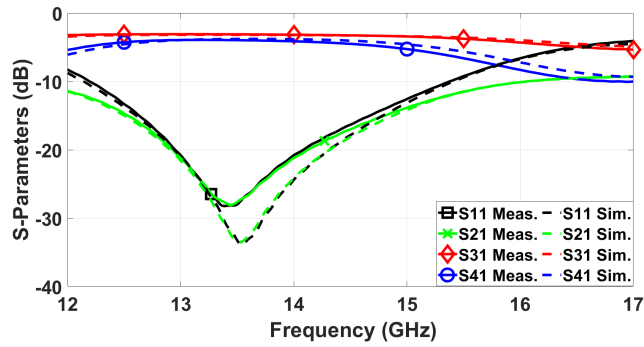
Figure 76. Scattering parameters of the coupler
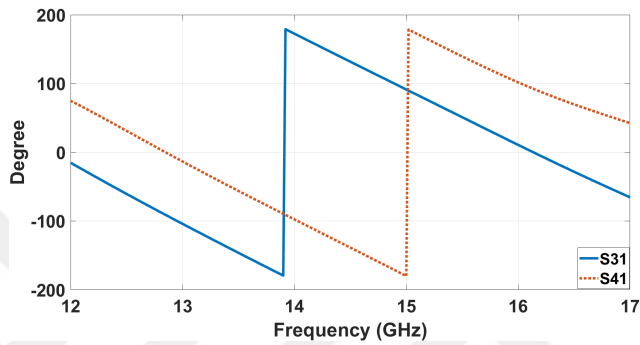
Figure 77. Phase responses of port 3 and port 4

3 and 4 cover the range from 180° to -180° keeping the phase difference between them ($\angle S_{41}$- $\angle S_{31}$) tunable in the range from 77° to 105°. The maximum phase difference of 105° is attained with the MS at 0° position, while a rotation of 90° achieves the lowest phase difference of 77°. Various rotation angles can be employed to produce different phases in the range from 77° to 105°.

Table 11 provides an extensive comparison of the proposed design with previously reported tunable couplers. Firstly, to the best of the authors' knowledge, our proposed design is the first adjustable phase coupler in the Ku band/mm band ranges. That is why we compare our work with reconfigurable couplers in different frequency ranges. Our work supplies the widest FBW compared to other studies. For example, GW-based hybrid couplers reported in (Taraji, 2022; Zhao and Denidni, 2020; Taraji, 2022) provide a fixed phase difference. The currently proposed coupler design can provide a narrower phase tuning range in comparison to the previously reported ones (Xu, Wang and Liu, 2019; Zhu and Abbosh, 2017; Pan et al., 2019). These authors used many varactor diodes to be able to tune the phase. However, using this type of lumped element causes huge losses at high frequencies. The frequency reconfigurable

Table 11. Comparison between the proposed coupler and previous studies.

Ref.	Technology	Freq. (GHz)	FBW(%)	Return Loss (dB)	Tuning types	Phase difference	Additional insertion loss (dB)
Taraji (2022)	GGW	13-15	14.3	<-20	Non-tunable	90 ± 1	NA
Zhao and Denidni (2020)	PRGW	27.5-31.5	13	-23	Non-tunable	90 ± 5	NA
Taraji (2022)	RGW	10.36-11.77	13	-34	Non-tunable	$84°\text{-}94°$	NA
Wan et al. (2020)	Microstrip (MS)	2.1-2.45	15.2	<-20	Freq.	$0°\text{-}10°$	NA
Xu, Wang and Liu (2019)	Microstrip (Varactor)	2.2-2.75	31.6	<-10	Freq. & Phase	$30°\text{-}150°$	<1.4
Zhu and Abbosh (2017)	Microstrip (Varactor)	0.9-1.1	20	<-10	Phase	$45°\text{-}135°$	<3
Pan et al. (2019)	Microstrip (Varactor)	2.4 f_c	20	<-10	Phase	$0°\text{-}180°$	<2.2
This work	MS-based SIGW	11.94-16.91	34.45	<-20	Phase	$77°\text{-}105°$	<0.2

73
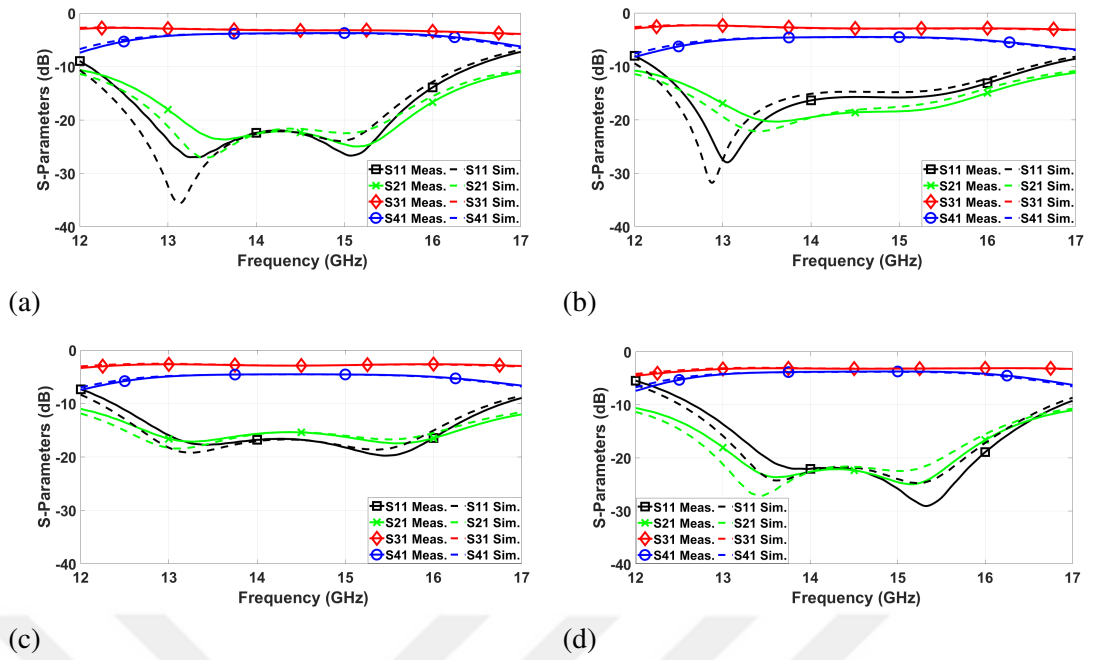
Figure 78. Scattering parameters of reconfigurable coupler at different angles a) 0° b) 30° c) 45° d) 90°
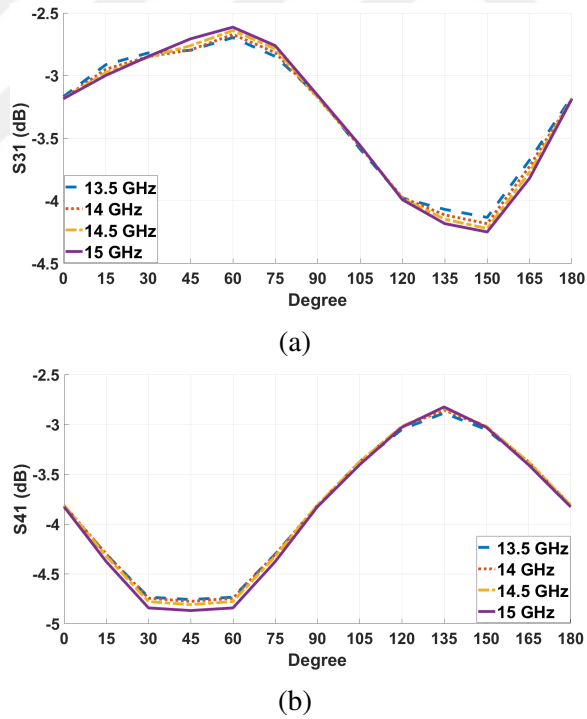
Figure 79. The response of rotation angle on output ports a) S_{31} b) S_{41}

coupler in (Wan et al., 2020) employed an MS to adjust the frequency however the phase difference was kept fixed. Finally, our obtained results show that the additional insertion loss of the proposed coupler is minimum compared to the other studies. It is
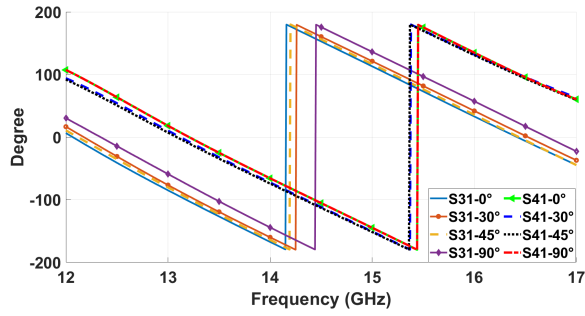
(a)
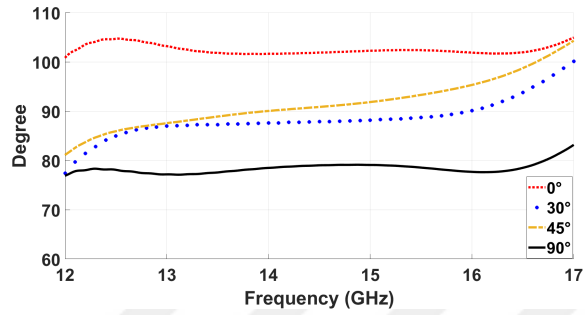
(b)

Figure 80. The phase variations with angles of rotation a) phases at port 3 and port 4 b) phase differences ($\angle S_{41}$- $\angle S_{31}$).

maintained within the acceptable range.

7.3 *Conclusion of the MS-based Reconfigurable Coupler*

In this study, a novel reconfigurable MS-based small UWB hybrid circular coupler is developed utilizing the SIGW technology. To the best of the authors' knowledge, our proposed design is the first adjustable phase coupler in the Ku band/mm band ranges. The findings obtained from the simulation show that phase reconfiguration can be accomplished by rotating the MS around the source coupler's central axis. The proposed design is continuously providing a variable phase difference over a fractional bandwidth of 34.45% between 77° and 105°. It is manufactured using PCB technology and measured using a network analyzer. The findings from simulation and measurement exhibit good agreement. This novel proposed coupler can be best used as a traditional beam-forming network. It can also be used for beam steering by changing the rotating angle or the operating frequency. So, it could be a good candidate for radar applications. Moreover, it could also be used for generating the well Grid Of Beams (GOB) networks. The current design supplies the widest FBW compared to other studies. It is very important to point out that our design provides a simple,

easy fabrication and implementation, compact in size, and easy-to-integrate solution with array antennas etched on the top layer of the structure as slot antennas without adding extra PCB materials to construct the antenna array. These novel features are solely comparing our design with all others mentioned in the literature. Also, the amplitude variation can be adjusted to change the beamwidth of the generated beams in the beamforming network. This work is being extended by changing the unit cell material and dimensions in the mm-Wave band.

CHAPTER 8 : CONCLUSION

Mm-wave technologies have recently gained popularity to expand the available BW and capacities. Higher frequencies provide the advantage of reducing the size of the system components, resulting in more compact designs. In addition, higher frequency bands facilitate short-range communications while operating over wideband. Various topologies for passive system elements exist in the literature for the mm-wave bands.

In this thesis, we mainly focused on developing GW technology-based filter, antenna, and directional coupler designs for mm-wave applications. We aim to minimize the overall structure size while optimizing the performance of the system components.

The first study is "Design of Triple-Band Bandpass Filter Using Inverted Microstrip Ridge Gap Waveguide for Ka-Band Applications". Double octagonal ring resonator is designed and optimized to provide a triple-band response. The IMGWG structure is used as a feeding network. The obtained operating three resonant frequencies are between 31 - 39 GHz with < -25 dB return losses. The obtained -3 dB FBW responses are 5.2%, 1.37%, and 2.46% and the filter exhibits low insertion losses of lower than 1.1 dB at the three resonant frequencies. This study is the first multi-band BPF proposed in the Ka-band using IMGWG technology.

In the second study "Optimizing Ridge Gap Waveguide Based Slot Antenna Shape for Maximum Gain and Bandwidth for Satellite Applications" five alternative slot antennas are shown based on SIGW at 70 GHz. The designed antennas are small, with a size of 8.4 x 7.2 x 0.87 mm^3 in total. Different slot geometries are studied, including rectangular, circular, hexagon, T-shape, and U-shape. All slot designs evaluated are very efficient, with overall radiation efficiencies above 90%. The realized gains of all designs are between 6.49- 10.98 dBi. The bandwidth of the antennas are varying between 1.57-5.35 GHz depending on the etched shape. The developed antennas are as well suitable for point-to-point wireless communication, mobile satellites, and inter-satellite applications.

In the third study, "UWB SIGW Based Four-Port MIMO Antenna for V/W-Band Applications", four-port compact SIGW-based MIMO antenna configurations are proposed for automotive radar and inter-satellite applications in the range of 72.7 to

79.5 GHz. The FBW of the proposed MIMO antenna design is approximately 9% and the isolation between resonators is higher than 24 dB. The calculated performance parameters' results ECC < 0.002, DG > 9.99 dB, CCL < 0.7 bits/s/Hz, ME > -0.7 dB, and TARC < -6 dB demonstrate that the proposed antennas have strong diversity performance in addition to compact sizes.

In the fourth study, "Design and Implementation RGW Based UWB Antenna Array for D-Band Applications", a new UWB 4 x 1 rectangular slot antenna array fed by the RGW feeding network is presented. To the best of the authors' knowledge, no similar antenna designs employing RGW in this frequency range can be found in the literature. Multiple quarter wavelength transformers were used to match the four ridge feeding lines side by side. The antenna array operates in D-band at 140.9 - 157.7 GHz. The bandwidth is roughly 17 GHz. The total efficiency of the antenna is around 95% over the whole operating frequencies. The peak realized gain is around 10 dBi which is higher than the single reference antenna by approximately 3 dBi.

In the fifth study, "DGS Based Isolation Enhancement for RGW Fed Compact MIMO Antenna System", a new four-port compact MIMO UWB antenna based on RGW technology is developed for D-band applications. The reference antenna element is designed as a circular slot on the top ground of the RGW feeding line. A transition to a traditional microstrip line is implemented. Multi-section quarter-wave transformers are implemented to match the RGW to the transition. The MIMO antenna is made up of four circularly matched reference antennas. The simulated impedance bandwidth extends from 148 GHz to 161.7 GHz. For the reduction of the mutual coupling, we consider five optimized DGS geometries on the upper ground plane. Two methods of analysis are considered in the current design. The use of different DGS geometries is found to be very effective in coupling reductions, the highest coupling level obtained from different DGS geometries is -26.4 dB and the lowest level reaches about -96 dB. The maximum realized gain is 7.97 dBi. The simulation results demonstrate outstanding performance with the following diversity properties: Envelop Correlation Coefficient ECC < 0.0006, Diversity Gain DG ~10 dB, Channel Capacity Loss CCL < 0.4 bit/s/Hz, Total Active Reflection Coefficient TARC ~ -23.4 dB and Multiplexing Efficiency ME η_{mux}>-1 dB.

In the final study "A Novel Circular Reconfigurable Metasurface-based Compact UWB

78

Hybrid Coupler for Ku-band Applications", a novel reconfigurable MS-based small UWB hybrid circular coupler is developed utilizing the SIGW technology. To the best of the authors' knowledge, our proposed design is the first reconfigurable coupler in the Ku band ranges. The suggested design constantly offers a changeable phase difference between 77° and 105° across an FBW of 34.45%. It is produced using PCB technology, and a network analyzer is used to measure it. The results of the simulation and the measurement show perfect agreement.

REFERENCES

Aghoutane, B., Das, S., Ghzaoui, M. E., Madhav, B. and El Faylali, H. (2022). *A novel dual band high gain 4-port millimeter wave MIMO antenna array for 28/37 GHz 5G applications*, AEU-International Journal of Electronics and Communications Vol. 145, p. 154071.

Ahmad, A., Choi, D.-y. and Ullah, S. (2022). *A compact two elements MIMO antenna for 5G communication*, Scientific Reports Vol. 12(1), pp. 1‒8.

Ali, M. M. M., El-Gendy, M. S., Al-Hasan, M., Mabrouk, I. B., Sebak, A. and Denidni, T. A. (2021). *A Systematic Design of a CompactWideband Hybrid Directional Coupler Based on Printed RGW Technology*, Ieee Access Vol. 9, pp. 56765‒56772.

Ali, M. M. M., Shams, S. I. and Sebak, A. (2017). *Printed ridge gap waveguide 3dB coupler: Analysis and design procedure*, IEEE Access Vol. 6, pp. 8501‒8509.

Birgermajer, S., Jankovic, N., Crnojevic-Bengin, V., Bozzi, M. and Radonic, V. (2017). *Forward-wave 0 dB directional coupler based on microstrip-ridge gap waveguide technology*, 2017 13th International Conference on Advanced Systems and Services in Telecommunications (TELSIKS), IEEE, pp. 154‒157.

Blanch, S., Romeu, J. and Corbella, I. (2003). *Exact representation of antenna system diversity performance from input parameter description*, Electronics letters Vol. 39(9), pp. 705‒707.

Castro, N., Pizarro, F., Herran-Ontanon, L. F. and Rajo-Iglesias, E. (2021). *Evaluation of inverted microstrip gap waveguide bandpass filters for Ka-band*, AEU-International Journal of Electronics and Communications Vol. 134, p. 153677.

Chen, S.-C., Wu, P.-W., Hsu, C.-I. G. and Sze, J.-Y. (2017). *Integrated MIMO slot antenna on laptop computer for eight-band LTE/WWAN operation*, IEEE Transactions on Antennas and Propagation Vol. 66(1), pp. 105‒114.

Chu, H. N. and Ma, T.-G. (2019). *Tunable directional coupler with very wide tuning range of power division ratio*, IEEE Microwave and Wireless Components Letters Vol. 29(10), pp. 652‒654.

Dwivedi, A. K., Sharma, A., Singh, A. K. and Singh, V. (2020). *Design of dual band four port circularly polarized MIMO DRA for WLAN/WiMAX applications*, Journal of Electromagnetic Waves and Applications Vol. 34(15), pp. 1990‒2009.

Dwivedy, B. and Behera, S. K. (2019). *Modelling, analysis and testing of an active element based wide-band frequency tunable compact rat-race hybrid*, AEUInternational Journal of Electronics and Communications Vol. 103, pp. 24‑31.

Fakharian, M. M., Alibakhshikenari, M., See, C. H. and Abd-Alhameed, R. (2022). *A high gain multiband offset MIMO antenna based on a planar log-periodic array for Ku/K-band applications*, Scientific Reports Vol. 12(1), pp. 1‑13.

Farahani, M., Akbari, M., Nedil, M., Denidni, T. A. and Sebak, A. R. (2017). *A novel low-loss millimeter-wave 3-dB 90° ridge-gap coupler using large aperture progressive phase compensation*, IEEE Access Vol. 5, pp. 9610‑9618.

Frecassetti, M. G., Mazzanti, A., Sevillano, J. F., Del Rio, D. and Ermolov, V. (2019). *D-band transport solution to 5G and beyond 5G cellular networks,* 2019 European Conference on Networks and Communications (EuCNC), IEEE, pp. 214‑218.

Gautam, A. K., Yadav, S. and Rambabu, K. (2018). *Design of ultra-compact UWB antenna with band-notched characteristics for MIMO applications*, IET Microwaves, Antennas & Propagation Vol. 12(12), pp. 1895‑1900.

Ghalib, A. and Sharawi, M. S. (2017). *TCM analysis of defected ground structures for MIMO antenna designs in mobile terminals*, IEEE Access Vol. 5, pp. 19680‑19692.

Ghaly, M. H., El-Din, M. S., Allam, A. and Fawzy, D. E. (2022). *SIGW Based Bidirectional Coupler for Ku-Band Applications*, 2022 9th International Conference on Electrical and Electronics Engineering (ICEEE), IEEE, pp. 36‑39.

Gomez, Villanueva, R. and Jardon, Aguilar, H. (2019). *Compact UWB uniplanar four-port MIMO antenna array with rejecting band*, IEEE Antennas and Wireless Propagation Letters Vol. 18(12), pp. 2543‑2547.

Gorur, A. (2004). *Description of coupling between degenerate modes of a dual-mode microstrip loop resonator using a novel perturbation arrangement and its dual-mode bandpass filter applications*, IEEE Transactions on Microwave Theory and Techniques Vol. 52(2), pp. 671‑677.

Hassani, N., Ostovarzadeh, M. H. and Razavi, S. A. (2018). *Realization of a dual mode filter in ridge gap waveguide technology*, Microwave and Optical Technology Letters Vol. 60(8), pp. 1975‑1979.

Huang, J., Dong, G., Cai, J., Li, H. and Liu, G. (2021). *A quad-port dual-band MIMO antenna array for 5G smartphone applications*, Electronics Vol. 10(5), p. 542.

Ibrahim, A. A. and Ali, W. A. (2022). *High isolation 4-element ACS-fed MIMO antenna with band notched feature for UWB communications*, International Journal of Microwave and Wireless Technologies Vol. 14(1), pp. 54‑64.

Iqbal, A., Saraereh, O. A., Ahmad, A. W. and Bashir, S. (2017). *Mutual coupling reduction using F-shaped stubs in UWB-MIMO antenna*, IEEE access Vol.6, pp. 2755‑2759.

Jetti, C. R. and Nandanavanam, V. R. (2018). *Trident-shape strip loaded dual bandnotched UWB MIMO antenna for portable device applications*, AEU-international Journal of Electronics and Communications Vol. 83, pp. 11‑21.

Khalid, M., Iffat Naqvi, S., Hussain, N., Rahman, M., Mirjavadi, S. S., Khan, M. J. and Amin, Y. (2020). *4-Port MIMO antenna with defected ground structure for 5G millimeter wave applications*, Electronics Vol. 9(1), p. 71.

Khan, J., Ullah, S., Ali, U., Tahir, F. A., Peter, I. and Matekovits, L. (2022). *Design of a millimeter-wave mimo antenna array for 5G communication terminals*, Sensors Vol. 22(7), p. 2768.

Kulkarni, J., Desai, A. and Sim, C.-Y. D. (2021). *Wideband four-port MIMO antenna array with high isolation for future wireless systems*, AEU-International Journal of Electronics and Communications Vol. 128, p. 153507.

Kulkarni, N. P., Bahadure, N. B., Patil, P. and Kulkarni, J. S. (2022). *Flexible Interconnected 4-Port MIMO Antenna for Sub-6 GHz 5G and X Band Applications*, AEUInternational Journal of Electronics and Communications p. 154243.

Kumar, A., Saxena, G., Kumar, P., Awasthi, Y. K., Jain, P., Singhwal, S. S. and Ranjan, P. (2022). *Quad-band circularly polarized super-wideband MIMO antenna for wireless applications*, International Journal of RF and Microwave Computer-Aided Engineering Vol. 32(6), p. e23129.

Li, M., Ma, J. and Ma, A. (2018). *Ka band orthogonal dumbbell groove substrate integrated waveguide filter*, 2018 12th International Symposium on Antennas, Propagation and EM Theory (ISAPE), IEEE, pp. 1‑4.

Li, Z., Du, Z., Takahashi, M., Saito, K. and Ito, K. (2011). *Reducing mutual coupling of MIMO antennas with parasitic elements for mobile terminals*, IEEE Transactions on Antennas and Propagation Vol. 60(2), pp. 473‑481.

Li, Z., Yin, C. and Zhu, X. (2019). *Compact UWB MIMO vivaldi antenna with dual band-notched characteristics*, IEEE Access Vol. 7, pp. 38696‑38701.

Liu, J. (2019). *Millimeter-Waves Slot Array Antennas Based on Gap Waveguide Technology*, Chalmers Tekniska Hogskola (Sweden).

Mahmoud Ali, M. M., Shams, S. I. and Sebak, A. (2019). *Ultra-wideband printed ridge gap waveguide hybrid directional coupler for millimetre wave applications*, IET Microwaves, Antennas & Propagation Vol. 13(8), pp. 1181‑1187.

Malhat, H. A., Zainud-Deen, S. H., El-Hemaily, H., Hamed, H. A. and Ibrahim, A. A. (2022). *Reconfigurable Circularly Polarized Hemispherical DRA Using Plasmonic Graphene Strips for MIMO Communications*, Plasmonics Vol. 17(2), pp. 765‑774.

Manzoor, Z. and Pak, A. (2018). *Narrowband Passband Microstrip Filter Using Octagonal Ring Resonator with DGS Technique*, International Journal of Engineering Science Invention (IJESI) Vol. 7(8), pp. 24‑27.

Marcaccioli, L., Farinelli, P., Tentzeris, M. M., Papapolymerou, J. and Sorrentino, R. (2008). *Design of a broadband MEMS-based reconfigurable coupler in Ku-band*, 2008 38th European Microwave Conference, IEEE, pp. 595‑598.

Masoodi, I. S., Ishteyaq, I., Muzaffar, K. and Magray, M. I. (2021). *A compact band-notched antenna with high isolation for UWB MIMO applications*, International journal of microwave and wireless technologies Vol. 13(6), pp. 634‑640.

Mathur, R. and Dwari, S. (2018). *Compact CPW-Fed ultrawideband MIMO antenna using hexagonal ring monopole antenna elements*, AEU-International Journal of Electronics and Communications Vol. 93, pp. 1‑6.

Mazinani, M., Arezoomand, M. and Pirhadi, A. (2018). *Ku-band gap waveguide filter design with improved out of band response*, Microwave and Optical Technology Letters Vol. 60(9), pp. 2154‑2161.

Mohanty, A. and Behera, B. R. (2021). *CMA assisted 4-port compact MIMO antenna with dual-polarization characteristics*, AEU-International Journal of Electronics and Communications Vol. 137, p. 153794.

Mousavirazi, Z., Ali, M. M. M., Gheisanab, H. N. and Denidni, T. A. (2022). *Analysis and Design of Ultra-Wideband PRGW Hybrid Coupler Using PEC/PMC Waveguide Model*. Sci Rep 12, 14214.

Nasr, M. A. and Kishk, A. A. (2020). *Analysis and design of broadband ridge-gapwaveguide tight and loose hybrid couplers*, IEEE Transactions on Microwave Theory and Techniques Vol. 68(8), pp. 3368‑3378.

Nematpour, E., Ostovarzadeh, M. H. and Razavi, S. A. (2019). *Development of a wide band TEM-based Bethe Hole coupler using ridge gap waveguide technology*, AEUInternational Journal of Electronics and Communications Vol. 111, p. 152933.

Ojaroudi Parchin, N., Jahanbakhsh Basherlou, H., Alibakhshikenari, M.,Ojaroudi Parchin, Y., Al-Yasir, Y. I., Abd-Alhameed, R. A. and Limiti, E. (2019). *Mobile-phone antenna array with diamond-ring slot elements for 5G massive MIMO systems*, Electronics Vol. 8(5), p. 521.

Okan, T. (2021). *High efficiency unslotted ultra-wideband microstrip antenna for subterahertz short range wireless communication systems*, optik Vol. 242, p. 166859.

Pan, Y. F., Zheng, S. Y., Chan, W. S. and Liu, H. W. (2019). *Compact phasereconfigurable couplers with wide tuning range*, IEEE Transactions on Microwave Theory and Techniques Vol. 68(2), pp. 681‑692.

Peng, H., Lei, P., Yang, H., Zhao, S. and Ding, X. (2021). *Π-type reconfigurable coupler based on a complementary tunable method*, Journal of ElectromagneticWaves and Applications Vol. 35(12), pp. 1611‑1618.

Puentes, M.,Weis, C., Schusler, M. and Jakoby, R. (2011). *Sensor array based on ring resonators for analysis of organic tissues*, in ʻ2011 IEEE MTT-S International Microwave Symposiumʼ, IEEE, pp. 1‑4.

Raj, U., Sharma, M. K., Singh, V., Javed, S. and Sharma, A. (2021). *Easily extendable four port MIMO antenna with improved isolation and wide bandwidth for THz applications*, Optik Vol. 247, p. 167910.

Rosengren, K. and Kildal, P.-S. (2005). *Radiation efficiency, correlation, diversity gain and capacity of a six-monopole antenna array for a MIMO system: theory, simulation and measurement in reverberation chamber*, IEE Proceedings-Microwaves, Antennas and Propagation Vol. 152(1), pp. 7‑16.

Shah, U., Sterner, M. and Oberhammer, J. (2013). *High-directivity MEMS-tunable directional couplers for 10‑18-GHz broadband applications*, IEEE transactions on microwave theory and techniques Vol. 61(9), pp. 3236‑3246.

Shamseldin, S. I. (2016). *Analysis and design of microwave devices based on ridge gap waveguide technology*, PhD thesis, Concordia University.

Sharma, S., Kanaujia, B. K., Khandelwal, M. K. et al. (2020). *Implementation of fourport MIMO diversity microstrip antenna with suppressed mutual coupling and crosspolarized radiations*, Microsystem Technologies Vol. 26(3), pp. 993‑1000.

Shen, D.,Wang, K. and Zhang, X. (2018). *A substrate integrated gap waveguide based wideband 3-dB coupler for 5G applications*, IEEE Access Vol. 6, pp. 66798‑66806.

Shu, M., Wu, W., Guo, C., Yang, Q., Chen, J. and Zhang, A. (2020). *A Ka-band Filter Based on the Quarter-height Pin Gap Waveguide with Improved Reliabilit*y, 2020 IEEE 3rd International Conference on Electronic Information and Communication Technology (ICEICT), IEEE, pp. 359‑361.

Sorkherizi, M. S. and Kishk, A. A. (2016). *Fully printed gap waveguide with facilitated design properties*, IEEE Microwave and Wireless Components Letters Vol. 26(9), pp. 657‑659.

Sorkherizi, M. S. and Kishk, A. A. (2017). *Self-packaged, low-loss, planar bandpass filters for millimeter-wave application based on printed gap waveguide technology*, IEEE Transactions on Components, Packaging and Manufacturing Technology Vol. 7(9), pp. 1419‑1431.

Sun, L., Li, Y., Zhang, Z. and Wang, H. (2020). *Self-decoupled MIMO antenna pair with shared radiator for 5G smartphones*, IEEE Transactions on Antennas and Propagation Vol.68(5), pp. 3423‑3432.

Szabo, Z., Park, G.-H., Hedge, R. and Li, E.-P. (2010). *A unique extraction of metamaterial parameters based on Kramers‑Kronig relationship*, IEEE Transactions on Microwave Theory and Techniques Vol. 58(10), pp. 2646‑2653.

Tan, X. and Lin, F. (2019). *A novel rat-race coupler with widely tunable frequency*, IEEE Transactions on Microwave Theory and Techniques Vol. 67(3), pp. 957‑967.

Tan, X., Lin, F., Sun, H. and Xue, Q. (2020). *Planar reconfigurable balanced ratrace coupler with improved amplitude imbalance performance and common-mode noise absorption*, IEEE Transactions on Microwave Theory and Techniques Vol. 68(10), pp. 4276‑4289.

Tan, X., Wang, W., Wu, Y., Liu, Y. and Kishk, A. A. (2019). *Enhancing isolation in dual-band meander-line multiple antenna by employing split EBG structure*, IEEE Transactions on Antennas and Propagation Vol. 67(4), pp. 2769‑2774.

Taraji, Mahboubeh, N. M. M. (2022). *Design of Branch line coupler based on ridge gap waveguide technology for X-band application*, IETE Journal of Research Vol. 68(2), pp. 917‑923.

Tebache, S., Belouchrani, A., Ghanem, F. and Mansoul, A. (2018). *Novel reliable and practical decoupling mechanism for strongly coupled antenna arrays*, IEEE Transactions on Antennas and Propagation Vol. 67(9), pp. 5892‑5899.

Teng, X., Ma, K., Yan, N. and Luo, Y. (2022). *A Low-Cost Antenna Using SISL Technology With Suppressed Sidelobe Level for 77 GHz Automotive Radar*, IEEE Antennas and Wireless Propagation Letters Vol. 21(9), pp. 1832‑1836.

Vassilev, V., He, Z. S., Carpenter, S., Zirath, H., Yan, Y., Hassona, A., Bao, M., Emanuelsson, T., Chen, J., Horberg, M. et al. (2018). *Spectrum efficient Dband communication link for real-time multi-gigabit wireless transmission*, in 2018 IEEE/MTT-S International Microwave Symposium-IMS, IEEE, pp. 1523‑1526.

Wan, Y., Chen, H., Chen, Q. and Li, Z. (2020). *A Miniaturized Frequencyreconfigurable Rat-race Coupler Based on Metasurface*, 2020 IEEE MTT-S International Microwave Workshop Series on Advanced Materials and Processes for RF and THz Applications (IMWS-AMP), IEEE, pp. 1‑3.

Wu,W., Yuan, B. andWu, A. (2018). *A quad-element UWB-MIMO antenna with bandnotch and reduced mutual coupling based on EBG structures*, International journal of Antennas and Propagation.

Xu, B. W., Wang, W. M. and Liu, Y. A. (2019). *A coupled line-based coupler with simultaneously tunable phase and frequency*, IEEE Transactions on Circuits and Systems I: Regular Papers, Vol. 66(12), pp. 4637‑4647.

Xu, B., Zheng, S. and Long, Y. (2019). *A phase tunable hybrid coupler with enhanced bandwidth*, International Journal of RF and Microwave Computer-Aided Engineering Vol. 29(8), p. e21779.

Zarifi, D., Farahbakhsh, A. and Zaman, A. U. (2022). *Design and development of broadband gap waveguide-based 0-dB couplers for Ka-band applications*, IET Microwaves, Antennas & Propagation Vol. 16(11), pp. 718‑724.

Zarifi, D. and Shater, A. (2017). *Design of a 3-DB directional coupler based on groove gap waveguide technology*, Microwave and Optical Technology Letters Vol. 59(7), pp. 1597‑1600.

Zhao, Z. and Denidni, T. A. (2020). *Millimeter-wave printed-RGW hybrid coupler with symmetrical square feed*, IEEE Microwave and Wireless Components Letters Vol. 30(2), pp. 156‑159.

Zheng, S. Y. (2017). *Simultaneous phase-and frequency-tunable hybrid coupler*, IEEE Transactions on Industrial Electronics Vol. 64(10), pp. 8088‑8097.

Zhu, H. and Abbosh, A. M. (2017). *A compact tunable directional coupler with continuously tuned differential phase,* IEEE Microwave and Wireless Components Letters Vol. 28(1), pp. 19‑21.